

THE MOTION OF A DISCONTINUOUS FIBER IN A  
TURBULENT VELOCITY FIELD

by

Keith D. Robinson

ProQuest Number: 10794476

All rights reserved

INFORMATION TO ALL USERS

The quality of this reproduction is dependent upon the quality of the copy submitted.

In the unlikely event that the author did not send a complete manuscript and there are missing pages, these will be noted. Also, if material had to be removed, a note will indicate the deletion.



ProQuest 10794476

Published by ProQuest LLC (2018). Copyright of the Dissertation is held by the Author.

All rights reserved.


This work is protected against unauthorized copying under Title 17, United States Code  
Microform Edition © ProQuest LLC.


ProQuest LLC.  
789 East Eisenhower Parkway  
P.O. Box 1346  
Ann Arbor, MI 48106 – 1346

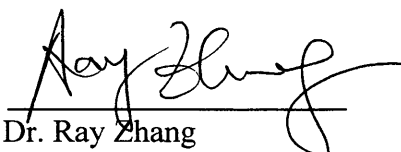
A thesis submitted to the Faculty and the Board of Trustees of the Colorado School of Mines in partial fulfillment of the requirements for the degree of Master of Science (Engineering Systems).

Golden, Colorado

Date 11/15/99

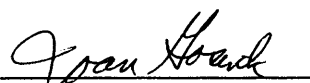
Signed:   
Keith D. Robinson

Approved:   
Dr. David Muñoz  
Thesis Advisor

Approved:   
Dr. Ray Zhang  
Thesis Advisor

Golden, Colorado

Date 11/15/99

  
Dr. Joan Gosink  
Department Head  
Engineering Division

## ABSTRACT

The purpose of this thesis was to model the motion of a single discontinuous fiber immersed in a turbulent velocity field. Three polypropylene fibers each with a length of 102 mm and diameters of 12  $\mu\text{m}$ , 30  $\mu\text{m}$ , and 47  $\mu\text{m}$  were studied. Fibers were attached to an airfoil placed in the test section of a wind tunnel. A square grid placed upstream of the airfoil generated isotropic, homogeneous turbulence at the fiber location. The characteristics of the turbulence were measured with a three-dimensional hot-wire anemometer. These measurements indicated that the mean axial velocity increased and the turbulent intensities decreased as the distance from the trailing edge of the airfoil increased and approached values between 6-8%. The motion of the fiber was modeled using a kinematic fiber model. This model assumed that the fiber was made up of rigid cylinders connected by frictionless, hinged connections. Aerodynamic forces acting on the fiber were assumed to follow the correlations presented by White and Ziabicki. Numerical results from single degree of freedom and two degrees of freedom models were compared to high-speed video recordings. The 12  $\mu\text{m}$  and 30  $\mu\text{m}$  kinematic models resulted in displacement and frequencies that agreed reasonably well with the video data. In order to model the 47  $\mu\text{m}$  fiber, it will be necessary to use models with more degrees of freedom or to refine the model by adding resistance to the hinge connections.

## TABLE OF CONTENTS

ABSTRACT .....	iii
LIST OF FIGURES .....	vii
LIST OF TABLES .....	xiii
ACKNOWLEDGEMENTS .....	xv
DEDICATION .....	xvi
Chapter 1. INTRODUCTION .....	1
1.1 Rationale .....	1
1.2 Description of Rotary-Spinning Process .....	2
1.3 Theoretical Background .....	10
1.3.1 The First Region of Fiber Growth .....	10
1.3.2 The Second Region of Fiber Growth. ....	18
1.3.3 The Third Region of Fiber Growth. ....	24
1.4 Objectives .....	26
Chapter 2. MODELING THE FIBER: LITERATURE SURVEY .....	28
2.1 Analytical Approach .....	28
2.2 Solving the String PDE .....	29
2.3 Solving the Cantilever Beam PDE .....	33
2.4 Summary of PDE Methods .....	36
Chapter 3. MODELING THE FIBER: KINEMATIC APPROACH.....	38
3.1 Analytical Approach .....	38
3.2 Single Degree of Freedom Kinematic Analysis.....	39
3.2.1 Gravitational Forces .....	40
3.2.2 Radial and Tangential Velocity Vectors .....	43
3.2.3 Relative Fiber Velocity .....	45

3.2.4 Equations of Motion .....	46
3.2.5 Numerical Simulation Technique .....	48
3.3 Two Degree of Freedom Kinematic Analysis .....	50
3.3.1 The Relative Velocity of the 2 <sup>nd</sup> (End) Element .....	51
3.3.2 The Position and Velocity of the 2 <sup>nd</sup> (End) Element .....	52
3.3.3 Relative Velocity of the 1st Element .....	53
3.3.4 Forces Acting on the 1st Element .....	53
3.3.5 Numerical Simulation Technique .....	56
3.3.6 Numerical Stability .....	56
3.4 Generalized Multi-Degree of Freedom Kinematic Analysis .....	57
3.5 Summary of Kinematic Numerical Simulation.....	59
<b>Chapter 4. EXPERIMENTAL METHOD .....</b>	<b>61</b>
4.1 Description of Test Fibers .....	61
4.2 Closed-Loop Wind Tunnel Description .....	61
4.3 Procedure for Measuring Velocity Data .....	64
4.4 Video Recording Procedure .....	65
<b>Chapter 5. CHARACTERIZATION OF THE VELOCITY FIELD</b> <b>ACTING UPON THE FIBER .....</b>	<b>67</b>
5.1 Velocity and Turbulence Measurements .....	67
5.2 Results of Measurements .....	72
5.2.1 Axial (U) Velocity Measurements .....	72
5.2.2 Vertical (W) Velocity Measurements .....	76
5.2.3 Horizontal (V) Velocity Measurements.....	78
5.2.4 Turbulent Intensities .....	79
5.2.5 Frequency Spectrum .....	82
5.3 Discussion of Results.....	88
<b>Chapter 6. HIGH-SPEED VIDEO RESULTS .....</b>	<b>89</b>
6.1 Frequency Results .....	89
6.2 Measured Displacements .....	92

Chapter 7. NUMERICAL RESULTS.....	94
7.1 Description of Numerical Simulation .....	94
7.2 The Effect of Axial Turbulence on Fiber Motion.....	94
7.3 Numerical Results: Displacement of Test Fibers.....	99
7.4 Numerical Results: Frequency Spectrums of Test Fibers.....	103
7.5 Numerical Results: Tensile Forces in Test Fibers .....	105
7.6 Summary of Numerical Results .....	107
Chapter 8. CONCLUSION AND FUTURE POSSIBILITIES .....	109
8.1 Conclusions .....	109
8.2 Future Possibilities for Research .....	110
REFERENCES CITED .....	113
APPENDIX A .....	115
APPENDIX B .....	122
APPENDIX C .....	129
APPENDIX D .....	136

## LIST OF FIGURES

Figure 1-1 Schematic of continuous high-speed spinning line (Ziabicki 1976) .....	3
Figure 1-2 Schematic diagram of the rotary-spinning process for discontinuous fibers .....	5
Figure 1-3 The near-wall region of fiber formation (centrifugal force only) .....	8
Figure 1-4 Fiber growth in the second region (both centrifugal and aerodynamic forces acting upon fiber).....	8
Figure 1-5 Stresses due to bending in growing fiber .....	9
Figure 1-6 Flow through a single hole in the basket wall.....	12
Figure 1-7 Forces acting on a fluid element in a single hole in the basket wall.....	15
Figure 1-8 Flow of molten material without any transverse forces .....	19
Figure 1-9 Velocity profile around a spinning disk in an infinite fluid .....	21
Figure 1-10 Relative velocity around a spinning disk in an infinite fluid .....	21
Figure 1-11 Dimensionless velocity profile around a spinning disk surrounded by a stationary wall.....	23
Figure 1-12 Dimensionless relative velocity around a spinning disk surrounded by a stationary wall.....	24
Figure 2-1 A vibrating string problem .....	30
Figure 2-2 A vibrating string with one fixed end .....	32
Figure 2-3 The cantilever beam model .....	33
Figure 3-1 Fiber model with a single degree-of-freedom .....	40
Figure 3-2 Equilibrium position in a steady, laminar velocity field.....	41

Figure 3-3 Angle theta as a function of the ratio of gravity force to drag force .....	42
Figure 3-4 Error using equation 3.3 rather than 3.1 to determine drag force .....	43
Figure 3-5 Velocity vector diagram .....	45
Figure 3-6 Two-element kinematic model.....	50
Figure 3-7 Free-body diagram for the 1 <sup>st</sup> element in a two-element model .....	54
Figure 4-1 Closed-loop wind tunnel for fiber testing .....	62
Figure 5-1 Instantaneous velocity for laminar and turbulent flow .....	68
Figure 5-2 Wind tunnel test section and velocity component detail.....	68
Figure 5-3 Mean axial ( <b>U</b> ) velocities measured downstream of the airfoil .....	73
Figure 5-4 Mean Vertical ( <b>W</b> ) velocities for different downstream positions .....	77
Figure 5-5 Mean Horizontal ( <b>V</b> ) velocities for different downstream positions .....	79
Figure 5-6 Axial turbulent intensity for four different fan speeds.....	80
Figure 5-7 Vertical turbulent intensity for four different fan speeds.....	81
Figure 5-8 Horizontal turbulent intensity for four different fan speeds.....	81
Figure 5-9 Amplification ratio plotted as a function of frequency ratio .....	83
Figure 5-10 Axial velocity frequency spectrum for 1000 RPM .....	84
Figure 5-11 Axial velocity frequency spectrum for 1500 RPM .....	85
Figure 5-12 Axial velocity frequency spectrum for 2000 RPM .....	85
Figure 5-13 Vertical velocity frequency spectrum for 1000 RPM .....	86
Figure 5-14 Vertical velocity frequency spectrum for 1500 RPM .....	86
Figure 5-15 Vertical velocity frequency spectrum for 2000 RPM .....	87
Figure 6-1 Low frequency fiber motion.....	91
Figure 6-2 High frequency fiber motion.....	91

Figure A-1 Tip displacement plot for 12 $\mu\text{m}$ fiber (Constant axial velocity, 1000 RPM).....	115
Figure A-2 Tip displacement plot for 30 $\mu\text{m}$ fiber (Constant axial velocity, 1000 RPM) .....	116
Figure A-3 Tip displacement plot for 12 $\mu\text{m}$ fiber (Constant axial velocity, 1500 RPM) .....	116
Figure A-4 Tip displacement plot for 30 $\mu\text{m}$ fiber (Constant axial velocity, 1500 RPM) .....	117
Figure A-5 Tip displacement plot for 12 $\mu\text{m}$ fiber (Constant axial velocity, 2000 RPM) .....	117
Figure A-6 Tip displacement plot for 30 $\mu\text{m}$ fiber (Constant axial velocity, 2000 RPM) .....	118
Figure A-7 Tip displacement plot for 12 $\mu\text{m}$ fiber (with axial turbulence, 1000 RPM) .....	118
Figure A-8 Tip displacement plot for 30 $\mu\text{m}$ fiber (with axial turbulence, 1000 RPM) .....	119
Figure A-9 Tip displacement plot for 12 $\mu\text{m}$ fiber (with axial turbulence, 1500 RPM ) .....	119
Figure A-10 Tip displacement plot for 30 $\mu\text{m}$ fiber (with axial turbulence, 1500 RPM) .....	120
Figure A-11 Tip displacement plot for 12 $\mu\text{m}$ fiber (with axial turbulence, 2000 RPM) .....	120
Figure A-12 Tip displacement plot for 30 $\mu\text{m}$ fiber (with axial turbulence, 2000 RPM) .....	121
Figure B-1 Tip displacement for 12 $\mu\text{m}$ , single degree of freedom model (1000 RPM).....	122
Figure B-2 Tip displacement for 12 $\mu\text{m}$ , two degrees of freedom model (1000 RPM).....	123

Figure B-3 Tip displacement for 12 $\mu\text{m}$ , single degree of freedom model (1500 RPM).....	123
Figure B-4 Tip displacement for 12 $\mu\text{m}$ , two degrees of freedom model (1500 RPM).....	124
Figure B-5 Tip displacement for 12 $\mu\text{m}$ , single degree of freedom model (2000 RPM).....	124
Figure B-6 Tip displacement for 12 $\mu\text{m}$ , two degrees of freedom model (2000 RPM).....	125
Figure B-7 Tip displacement for 30 $\mu\text{m}$ , single degree of freedom model (1000 RPM).....	125
Figure B-8 Tip displacement for 30 $\mu\text{m}$ , two degrees of freedom model (1000 RPM).....	126
Figure B-9 Tip displacement for 30 $\mu\text{m}$ , single degree of freedom model (1500 RPM).....	126
Figure B-10 Tip displacement for 30 $\mu\text{m}$ , two degrees of freedom model (1500 RPM).....	127
Figure B-11 Tip displacement for 30 $\mu\text{m}$ , single degree of freedom model (2000 RPM).....	127
Figure B-12 Tip displacement for 30 $\mu\text{m}$ , two degrees of freedom model (2000 RPM).....	128
Figure C-1 Frequency Spectrum for 12 $\mu\text{m}$ , single degree of freedom model (1000 RPM) .....	129
Figure C-2 Frequency Spectrum for 12 $\mu\text{m}$ , two degrees of freedom model (1000 RPM) .....	130
Figure C-3 Frequency Spectrum for 12 $\mu\text{m}$ , single degree of freedom model (1500 RPM) .....	130
Figure C-4 Frequency Spectrum for 12 $\mu\text{m}$ , two degrees of freedom model (1500 RPM) .....	131

Figure C-5 Frequency Spectrum for 12 $\mu\text{m}$ , single degree of freedom model (2000 RPM) .....	131
Figure C-6 Frequency Spectrum for 12 $\mu\text{m}$ , two degrees of freedom model (2000 RPM) .....	132
Figure C-7 Frequency Spectrum for 30 $\mu\text{m}$ , single degree of freedom model (1000 RPM) .....	132
Figure C-8 Frequency Spectrum for 30 $\mu\text{m}$ , two degrees of freedom model (1000 RPM) .....	133
Figure C-9 Frequency Spectrum for 30 $\mu\text{m}$ , single degree of freedom model (1500 RPM) .....	133
Figure C-10 Frequency Spectrum for 30 $\mu\text{m}$ , two degrees of freedom model (1500 RPM) .....	134
Figure C-11 Frequency Spectrum for 30 $\mu\text{m}$ , single degree of freedom model (2000 RPM) .....	134
Figure C-12 Frequency Spectrum for 30 $\mu\text{m}$ , two degrees of freedom model (2000 RPM) .....	135
Figure D-1 Fiber tension for 12 $\mu\text{m}$ , single degree of freedom model (1000 RPM).....	136
Figure D-2 Fiber tension for 12 $\mu\text{m}$ , two degrees of freedom model (1000 RPM).....	137
Figure D-3 Fiber tension for 12 $\mu\text{m}$ , single degree of freedom model (1500 RPM).....	137
Figure D-4 Fiber tension for 12 $\mu\text{m}$ , two degrees of freedom model (1500 RPM).....	138
Figure D-5 Fiber tension for 12 $\mu\text{m}$ , single degree of freedom model (2000 RPM).....	138
Figure D-6 Fiber tension for 12 $\mu\text{m}$ , two degrees of freedom model (2000 RPM).....	139

Figure D-7 Fiber tension for 30 $\mu\text{m}$ , single degree of freedom model (1000 RPM).....	139
Figure D-8 Fiber tension for 30 $\mu\text{m}$ , two degrees of freedom model (1000 RPM).....	140
Figure D-9 Fiber tension for 30 $\mu\text{m}$ , single degree of freedom model (1500 RPM).....	140
Figure D-10 Fiber tension for 30 $\mu\text{m}$ , two degrees of freedom model (1500 RPM).....	141
Figure D-11 Fiber tension for 30 $\mu\text{m}$ , single degree of freedom model (2000 RPM).....	141
Figure D-12 Fiber tension for 30 $\mu\text{m}$ , two degrees of freedom model (2000 RPM).....	142

## LIST OF TABLES

Table 5-1 Mean axial velocity ( $U$ ) and turbulent intensity ( $u'/U$ ) at different positions downstream of the airfoil with four different fan speeds (500, 1000, 1500, & 2000 RPM).....	74
Table 5-2 Reynolds numbers for each fan speed .....	75
Table 5-3 Mean vertical velocity ( $W$ ) and turbulent intensity ( $w'/U$ ) at different positions downstream of the airfoil with four different fan speeds (500, 1000, 1500, & 2000 RPM).....	76
Table 5-4 Mean horizontal velocity ( $V$ ) and turbulent intensity ( $v'/U$ ) at different positions downstream of the airfoil with four different fan speeds (500, 1000, 1500, & 2000 RPM).....	78
Table 6-1 Frequency results for 12 $\mu$ m fiber .....	89
Table 6-2 Frequency results for 30 $\mu$ m fiber .....	89
Table 6-3 Frequency results for 47 $\mu$ m fiber .....	90
Table 6-4 Maximum measured displacements for 12 $\mu$ m fiber (mm).....	92
Table 6-5 Maximum measured displacements for 30 $\mu$ m fiber (mm).....	93
Table 6-6 Maximum measured displacements for 47 $\mu$ m fiber (mm).....	93
Table 7-1 First five local peaks at tip of 12 $\mu$ m fiber and resulting damping factor (without axial turbulence, 1000 RPM) .....	96
Table 7-2 First five local peaks a tip of fiber 30 $\mu$ m and resulting damping factor (without axial turbulence, 1000 RPM) .....	96
Table 7-3 First five local peaks at tip of 12 $\mu$ m fiber and resulting damping factor (with axial turbulence, 1000 RPM).....	97
Table 7-4 First five local peaks at tip of 30 $\mu$ m fiber and resulting damping factor (with axial turbulence, 1000 RPM).....	97

Table 7-5 Average damping ratio for 12 $\mu\text{m}$ and 30 $\mu\text{m}$ fibers.....	98
Table 7-6a Maximum positive 12 $\mu\text{m}$ fiber displacement (mm).....	100
Table 7-6b Approximate mean 12 $\mu\text{m}$ fiber position (mm).....	100
Table 7-6c Maximum negative 12 $\mu\text{m}$ fiber displacement (mm).....	100
Table 7-7a Maximum positive 30 $\mu\text{m}$ fiber displacement (mm).....	100
Table 7-7b Approximate mean 30 $\mu\text{m}$ fiber position (mm).....	101
Table 7-7c Maximum negative 30 $\mu\text{m}$ fiber displacement (mm).....	101
Table 7-8 Frequency data (Hz) for 12 $\mu\text{m}$ fiber.....	104
Table 7-9 Frequency data (Hz) for 30 $\mu\text{m}$ fiber.....	104

## ACKNOWLEDGEMENTS

This research was funded by a grant from the National Science Foundation (NSF) contract DMI-9634828.

## DEDICATION

For Merrie.

“In the land of Uz there lived a man...And so he died, old and full of years.”

## Chapter 1

### INTRODUCTION

#### 1.1 Rationale

In any manufacturing process, the goal is to obtain a usable end product. One of the most important factors in the manufacturing process is to be able to control the process so that the product is consistent and that the amount of rejected product is minimized.

In many cases, it is possible to control a process by “feel”. This type of control relies upon a trial-and-error solution method consisting of many different test runs. In addition, this control method is very dependent upon the knowledge and experience of the system operator. If an operator leaves a company, the productivity of a system may suffer.

A more desirable approach to controlling a manufacturing process is one that is based upon knowledge of how various production factors affect the final product. With this approach, the knowledge required to operate the manufacturing process can be documented more easily and should be independent of the individual operator. In the rotary spinning method of producing small diameter discontinuous fibers, production factors include parameters such as spin rate, air velocity, melt temperature, and air

temperature. Examples of product parameters include such items as fiber diameter, fiber length, fiber strength and production rate.

In addition to more consistent results, a better understanding of how the production factors affect product parameters provides a foundation of knowledge which may be used to develop improvements in the product and manufacturing process itself. Improvement need not be completed through another time consuming trial and error method. Instead, analytical and/or numerical modeling could be used to reduce the amount of time and iterations required to improve or to optimize the process.

This thesis examines factors such as fiber diameter and turbulence in order to determine their affects upon fiber motion and the tensile forces within the fiber. This knowledge will lead to a better understanding of the interaction between the fiber and air stream that could be used to improve the manufacturing process. The effect of temperature upon the motion of the fiber is not considered in this thesis.

## 1.2 Description of Rotary-Spinning Process

The amount of literature available that discusses the manufacturing of fibers is large. However, most of the literature concerns the manufacturing of continuous fibers. A large bibliography is presented by Ziabicki (Ziabicki 1976, Ziabicki et al 1985). These references present a wealth of information concerning the fiber properties, rate of

solidification, the affect of drawing and extruding on fiber properties. Figure 1-1 presents a schematic of a typical high-speed continuous fiber spinning line (Ziabicki, 1976).

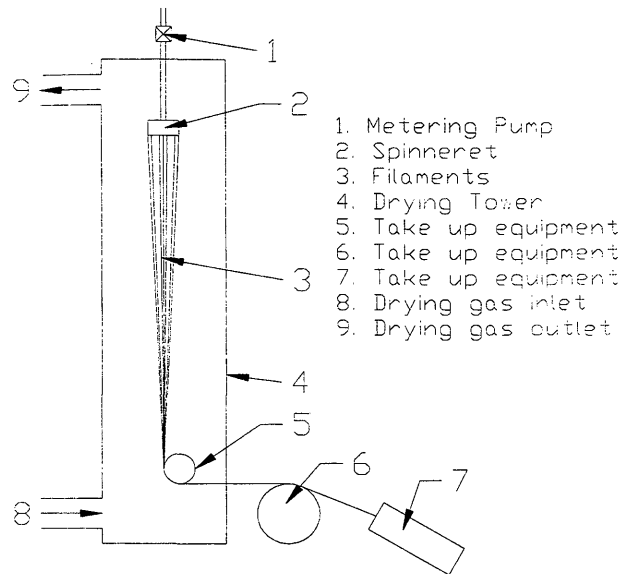


Figure 1-1

Schematic of continuous high-speed spinning line (Ziabicki 1976).

Ziabicki (1985) provides a summary of the basic equations that govern melt spinning on a continuous fiber line. The first equation describes the forces acting on the continuous fiber:

$$\frac{dF}{dx} = W \cdot \left( \frac{dV}{dx} - \frac{g}{v} \right) - \pi \cdot D \cdot \tau_f \quad (1.1)$$

where  $F$  is the tension in the fiber,  $x$  is the distance from the spinneret,  $W$  is the mass flow rate (extrusion rate) per fiber,  $V$  is the axial velocity,  $g$  is the acceleration due to

gravity,  $D$  is the diameter of the fiber,  $\nu$  is the kinematic viscosity of molten material, and  $\tau_f$  is the shear stress on the surface of the fiber.

The second equation describes the stresses in the fiber:

$$\eta \cdot \left( \frac{dV}{dx} \right) = \sigma = F \cdot \frac{\rho \cdot V}{W} \quad (1.2)$$

where  $\eta$  is the elongational viscosity,  $V$  is the axial velocity,  $x$  is the distance from the spinneret,  $\sigma$  is the tensile stress,  $F$  is the tension,  $\rho$  is the density of fiber material,  $W$  is the mass flow rate (extrusion rate) per fiber, and  $D$  is the diameter of the fiber.

The third equation given by Ziabicki describes the mass balance of the fiber drawing process:

$$\frac{\rho \cdot V \cdot \pi \cdot D^2}{4} = \text{const} = W \quad (1.3)$$

where  $\rho$  is the density of fiber material,  $V$  is the axial velocity,  $D$  is the diameter of the fiber, and  $W$  is the mass flow rate (extrusion rate) per fiber.

The final equation describes the energy balance during the fiber drawing process:

$$\frac{dT}{dx} = - \frac{\pi \cdot D \cdot h}{W \cdot C_p} \cdot (T - T_s) \quad (1.4)$$

where  $T$  is the average fiber temperature,  $x$  is the distance from the spinneret,  $D$  is the diameter of the fiber,  $h$  is the convective coefficient of heat transfer,  $W$  is the mass flow rate (extrusion rate) per fiber,  $C_p$  is the specific heat of polymer,  $T_s$  is the cooling air

temperature. It is reasonable to expect that a similar set of equations can be used to describe the production of discontinuous fibers using the rotary-spinning process.

The rotary spinning process utilizes a rapidly spinning basket with small holes in the outer wall (Figure 1-2). The molten material is poured into the basket and then is forced through the holes onto the outer surface of the basket. Once on the outer surface of the basket, the molten fiber material starts to grow away from the surface of the basket. As this new fiber grows longer, it leaves the boundary layer surrounding the basket and begins to be stretched by the combined centripetal and drag forces. This stretching continues until the fiber breaks.

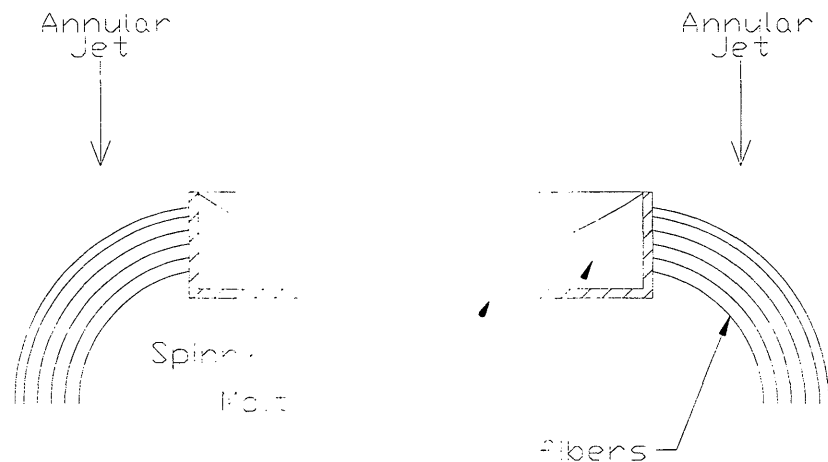


Figure 1-2

Schematic diagram of the rotary-spinning process for discontinuous fibers.

Temperature is another factor that has an important affect upon the fibers. Initially, the molten material and the air stream near the basket is above the glass transition temperature. As the fibers travel through the air, they cool and pass through the glass transition temperature. The behavior of the material changes as it passes through this temperature. The effects of temperature will not be included in this study.

The most detailed analysis of the centrifugal spinning process used to make discontinuous fibers was by Cai (1994) and Cai et al (1994). These papers discussed the factors that affect the initial growth of the fibers in a centrifugal spinning process. The study utilized glycerin to model the molten fiber material. One of the primary results of the study by Cai was that the fiber diameter, length, and production rate were proportional to the product of the Reynolds and Weber numbers.

The process air passing over the fiber creates drag forces that act upon the fiber. The velocity field in the manufacturing process is the result of two main factors: the rapidly spinning basket and the annular jet. As the basket spins, the air surrounding the basket begins to spin due to the viscous drag. At the surface of the basket, the air is traveling with the same velocity as the basket. As the distance from the basket decreases, the velocity of the air also decreases. Since the fiber is traveling at the same rate as the surface of the basket, a relative velocity between the fiber and the air is created.

The second cause of the velocity field is the annular jet that surrounds the basket. As the annular jet passes over the fiber, it stretches the fiber and causes it to align itself

with the flow. As a result of these two causes, the process of formation can be thought of consisting of three distinct regions.

The first region is near the wall of the basket where centrifugal force is the main force acting upon the fiber. In this region, the molten fiber material is within the boundary layer of the spinning basket. The relative air velocity in the boundary layer is almost zero, so there are no drag forces to act on the newly formed fiber. In this region, the fiber begins to grow away from the surface of the spinning basket due to the centrifugal acceleration. In this region, the fiber is essentially perpendicular to the surface of the basket (Figure 1-3). At this point the only force in the fiber is a tension force.

The second region begins as the fiber exits the slow moving boundary layer around the basket and is acted upon by both centrifugal and aerodynamic drag forces. As the fiber grows away from the surface of the basket, the relative velocity across the fiber begins to increase. As this velocity increases, the drag force acting upon the fiber increases and begins to bend the fiber (Figure 1-4). Similar behavior can be seen in liquid surrounding a rapidly spinning cup (Fraser et al, 1963).

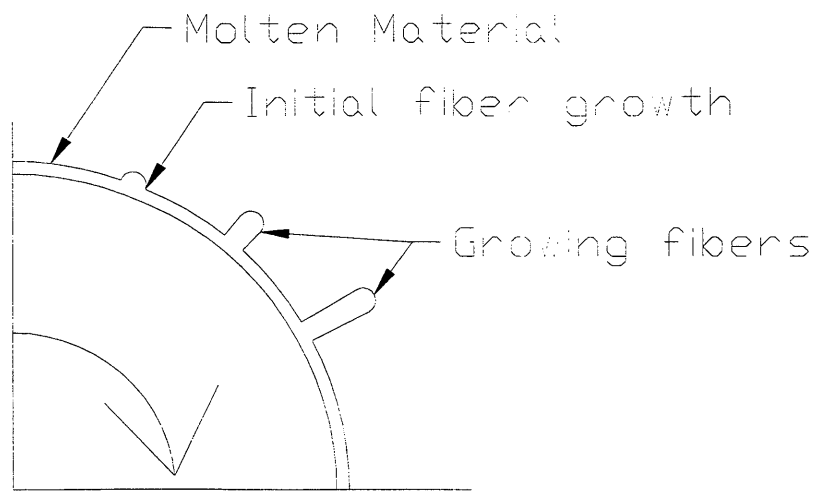


Figure 1-3

The near-wall region of fiber formation (centrifugal force only).

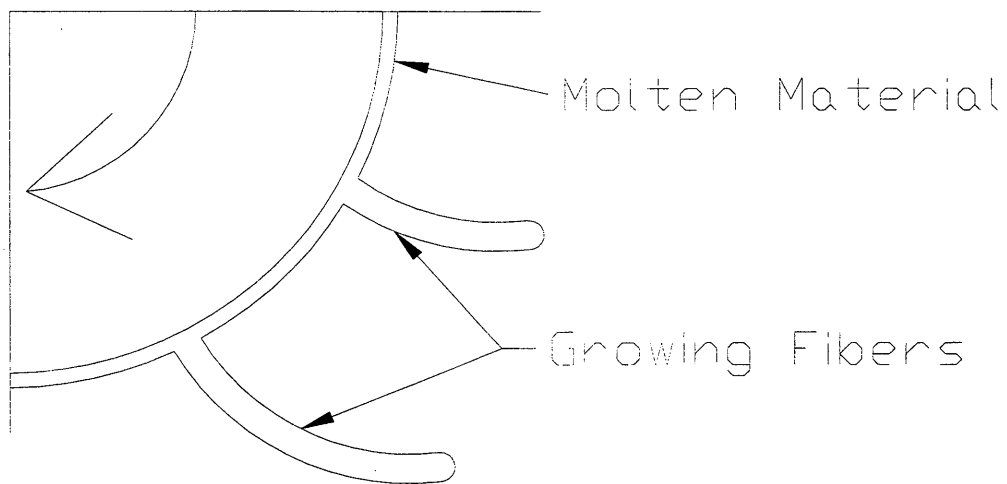


Figure 1-4

Fiber growth in the second region (both centrifugal and aerodynamic forces acting upon fiber).

In addition to the tensile force created by the centrifugal force, this bending creates an additional stress within the fiber. On the upstream side of the fiber, this additional stress is a tensile force while on the downstream side of the fiber it is a compressive force (Figure 1-5). This bending increases until the free end of the fiber is almost parallel to the velocity field and it enters the third region.

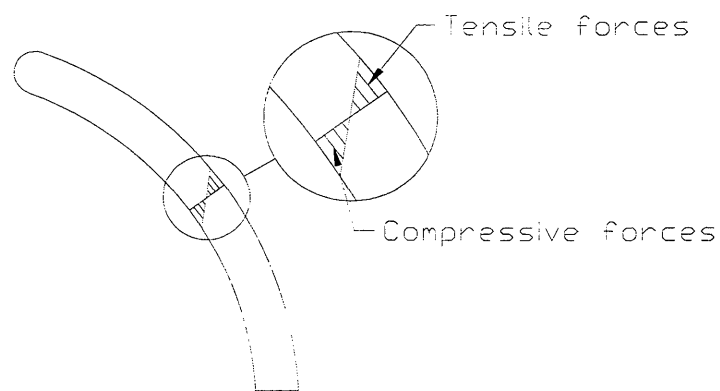


Figure 1-5

Stresses due to bending in growing fiber.

The third region begins when the fiber is relatively far away from the wheel and is parallel to the airflow. In this region, the aerodynamic drag forces are large compared to the centrifugal force, which is essentially zero. It is this third region which is modeled most closely in the wind tunnel. Since aerodynamic forces within this region mainly affect the fiber, the variation in these aerodynamic forces is of primary interest in this

region. Because of this, it is desirable to study how the turbulent fluctuations within the velocity field affect the fiber.

### 1.3 Theoretical Background

In order to understand the rotary-spinning process, it is necessary to develop a system of equations similar to those presented by Ziabicki for the continuous fiber spinning process. This section will discuss some of the basic forces that act upon the melt and the fiber and then develop some basic force relationships that can be used to analyze the process. The analysis will be broken into three separate sections that correspond to the three regions encountered by the fiber during the spinning process.

#### 1.3.1 The First Region of Fiber Growth

Equation 1.3 describes the flow rate of the fiber material. In a continuous fiber process, the speed of the take-up reel controls the speed of the fiber. Since the diameter of the fiber is essentially constant by the end of the process and the speed of the take-up reel is constant, the mass flow rate of the fiber is constant. This mass flow rate represents the amount of fiber made in a given time period.

In the rotary-spinning process, the mass flow rate of the fiber is determined by two factors that act at the root of the fiber. The first factor is the amount of molten material that is forced through the small orifice in the basket wall by the centripetal force created by the angular velocity of the basket. The second factor is the amount of material

that is connected to a fiber and is pulled through the orifice by the force acting on the fiber.

The first force that affects the mass flow rate of molten material is the centripetal force created by the rotation of the basket. The centripetal force acting upon a body is determined using the equation:

$$F_C = \frac{m \cdot v^2}{r} \quad (1.5)$$

where  $m$  is the mass of an object or fluid element,  $v$  is the velocity of an object or fluid element and  $r$  is the radius of curvature of the object's path.

This equation indicates that the force is proportional to the mass of the fluid, inversely proportional to the radius, and proportional to the velocity squared. The velocity at the surface of the basket is the angular velocity times the radius:

$$v = \omega \cdot r \quad (1.6)$$

Substituting this relationship in equation 1.5 yields the following relationship:

$$F_C = \frac{m \cdot (\omega \cdot r)^2}{r} = m \cdot \omega^2 \cdot r \quad (1.7)$$

Equation 1-7 indicates that the force acting upon the fiber melt is proportional to the angular velocity squared and proportional to the radius of curvature, or in this case, the radius of the basket.

Now that the force acting on the melt has been defined, the next question that needs to be answered is how the mass flow rate is related to this centripetal force. This is

important because the mass flow rate controls the quantity of fibers created. One method that can be used to model this flow is to assume that each hole in the basket wall is a pipe and solve the Navier-Stokes equations to determine the velocity profile, the flow rate, the mean velocity, and the shear stress within the hole (Figure 1-6). Once the mass flow rate has been solved for one hole, the total mass flow rate can be found by multiplying by the total number of holes.

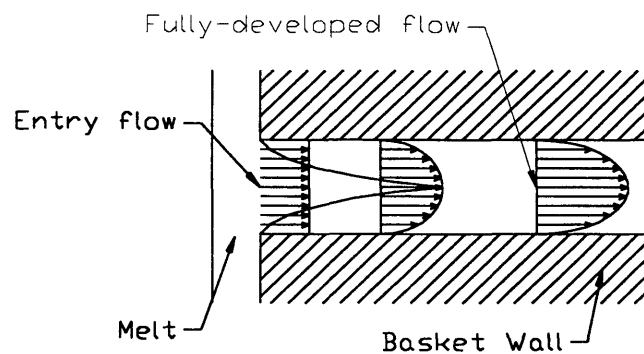


Figure 1-6

Flow through a single hole in the basket wall.

One shortcoming of this approach is that it assumes that the melt flows like a Newtonian fluid. If we assume that the fluid does not experience any phase changes while passing through the basket wall, this assumption will be closer to reality. Even with this inaccuracy, the pipe model will give an indication of how the basket radius and the angular velocity of the basket affect the production rate for the fibers.

One benefit is that the flow through the hole is laminar due to the high viscosity of the fluid. Solving the Navier-Stokes equations for laminar flow through a cylindrical results in the following set of equations (White 1974, Schlichting 1979). The velocity profile is given by:

$$u(r) = \frac{1}{4 \cdot \mu} \cdot \left( -\frac{dp}{dx} \right) \cdot (r_o^2 - r^2) \quad (1.8)$$

where  $u(r)$  is the velocity at different distances from axis of pipe,  $r$  is distance from the center of the pipe,  $r_o$  is the radius of pipe,  $\mu$  is the viscosity of fluid, and  $\frac{dp}{dx}$  is the pressure gradient across the pipe.

Once the velocity profile is known, the volumetric flow rate of fiber material through the hole can be determined by:

$$Q = \frac{\pi \cdot r_o^2}{8 \cdot \mu} \cdot \left( -\frac{dp}{dx} \right) \quad (1.9)$$

where  $Q$  is the volumetric flow rate,  $r_o$  is the radius of pipe,  $\mu$  is the viscosity of fluid, and  $\frac{dp}{dx}$  is the pressure gradient across the pipe.

The mean velocity of the material in the pipe is determined by:

$$\bar{u} = \frac{1}{2} \cdot u_{Max} \quad (1.10)$$

where  $\bar{u}$  is the mean velocity and  $u_{Max}$  is the maximum velocity. The shear stress acting on the fluid in the pipe is found to be:

$$\tau_w = \frac{4 \cdot \mu \cdot \bar{u}}{r_o} \quad (1.11)$$

where  $\tau_w$  is the wall stress,  $\mu$  is the viscosity of the fluid,  $\bar{u}$  is the mean velocity, and  $r_o$  is the radius of the pipe.

These four equations completely describe the motion of a fluid within a pipe and can easily be solved to determine the amount of fluid passing through a single hole in the basket wall. In order to solve these equations, it is necessary to determine the pressure gradient acting upon the length of the pipe.

The pressure gradient that drives the flow through the holes is created by the difference between the centrifugal force between the inner and outer surface of the basket. Figure 1-7 shows a fluid element and the forces acting upon it. Pressure is a force per unit area, so the pressure on each end of the pipe is found by dividing the force on each end of the pipe by the area of the pipe. The difference between these pressures divided by the length of the pipe will give the pressure gradient across the pipe length. The force on each end of the fluid element is:

$$F = m \cdot \omega^2 \cdot r \quad (1-12)$$

where  $m$  is the mass of the fluid element,  $\omega$  is the angular velocity of the basket, and  $r$  is the radius of the inner or outer surface of the basket.

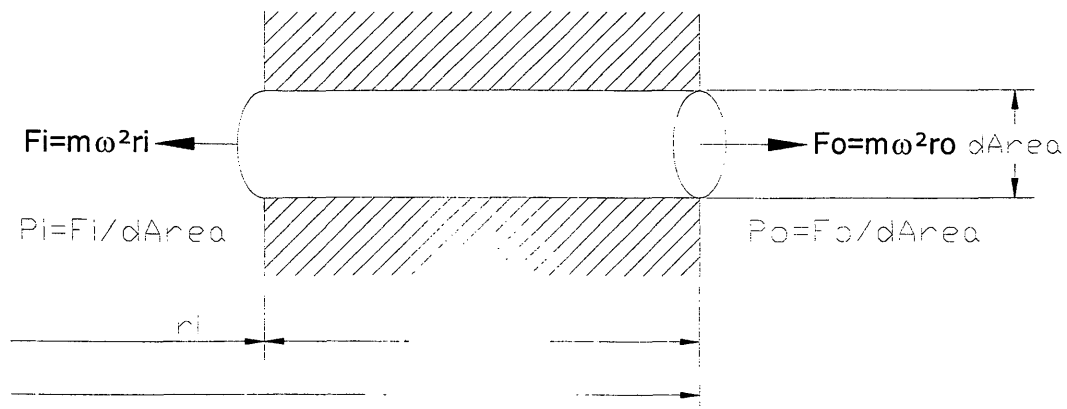


Figure 1-7

Forces acting on a fluid element in a single hole in the basket wall.

The pressure on each end is the force divided by the area of the pipe:

$$P = \frac{F}{Area} = \frac{m \cdot \omega^2 \cdot r}{\pi \cdot r_{Pipe}^2} \quad (1.13)$$

The pressure gradient is the pressure difference between the two ends of the fluid in the pipe divided by the length of the pipe:

$$\frac{dp}{dx} = \frac{P_{Outer} - P_{Inner}}{r_{Outer} - r_{Inner}} = \frac{m \cdot \omega^2}{\pi \cdot r_{Pipe}^2 \cdot (r_{Outer} - r_{Inner})} \cdot (r_{Outer} - r_{Inner}) \quad (1.14)$$

Simplifying this expression further yields:

$$\frac{dp}{dx} = \frac{P_{Outer} - P_{Inner}}{r_{Outer} - r_{Inner}} = \frac{m \cdot \omega^2}{\pi \cdot r_{Pipe}^2} \quad (1.15)$$

At this point, the only unknown quantity in equation 1.15 is the mass of the fluid element.

This is easily calculated using the equation:

$$m = \rho_{Melt} \cdot \pi \cdot r_{Pipe}^2 \cdot (r_{Outer} - r_{Inner}) \quad (1.16)$$

Substituting this result into equation 1.15 yields the pressure gradient across a single hole in the basket wall:

$$\frac{dp}{dx} = \frac{\omega^2}{\pi \cdot r_{Pipe}^2} \cdot \rho_{Melt} \cdot \pi \cdot r_{Pipe}^2 \cdot (r_{Outer} - r_{Inner}) \quad (1.17)$$

or, after simplifying further:

$$\frac{dp}{dx} = \omega^2 \cdot \rho_{Melt} \cdot (r_{Outer} - r_{Inner}) \quad (1.18)$$

Substituting these results into equation 1.9 yields an expression that gives the flow rate through a single hole in the basket wall:

$$Q = \frac{\pi \cdot r_{Pipe}^2}{8 \cdot \mu} \cdot \omega^2 \cdot \rho_{Melt} \cdot (r_{Outer} - r_{Inner}) \quad (1.19)$$

Unfortunately, this equation is accurate only for an infinitely long pipe. This is due to the fact that the fluid flow is not fully developed immediately after entering the pipe. Instead, a boundary layer begins to develop and the flow continues to change for some distance after the pipe entrance. Before equation 1.19 can be used, it is necessary to determine how long it will take the fluid melt to reach a fully developed flow condition.

White (1974) derives two equations for the flow in the inlet of a duct. The first relates the average velocity in the duct to the pressure drop and the second gives the

entrance length for the fluid, both of which are a function of the Reynolds number in the pipe. The entrance length is defined as the distance required for the flow to achieve a fully developed flow profile. These equations are based on the assumption that the entrance to the pipe is smooth and that the velocity profile is uniform at the entrance of the pipe as shown in Figure 1-6. The average velocity is found to be:

$$\frac{2 \cdot (p_0 - p_x)}{\rho \cdot \bar{u}^2} = \frac{64 \cdot x}{\text{Re}_D \cdot D} + 1.31 \quad (1.20)$$

where  $p_0$  is the pressure at inlet of pipe,  $p_x$  is the pressure at an arbitrary distance from the entrance of the pipe,  $x$  is an arbitrary distance from entrance of pipe and  $\rho$  is the density of fluid flowing through pipe. The Reynolds number ( $\text{Re}_D$ ) is defined to be:

$$\text{Re}_D = \frac{\rho_{\text{Melt}} \cdot D_{\text{Pipe}} \cdot \bar{u}}{\mu_{\text{Melt}}} \quad (1.20)$$

where  $\rho$  is the density of fluid flowing through pipe,  $D_{\text{Pipe}}$  is the diameter of the pipe,  $\mu$  is the viscosity of fluid flowing through the pipe, and  $\bar{u}$  is the average velocity in the pipe.

The entrance length for a single pipe is found to be:

$$\frac{x_L}{D_{\text{Pipe}}} \approx 0.08 \cdot \text{Re}_D + 0.7 \quad (1.21)$$

where  $x_L$  is the length required for fully developed flow. Equation 1.21 indicates that the entrance length approaches a value of 0.7 times the pipe diameter as the Reynolds number approaches zero.

This suggests that equation 1.21 can be used to determine the melt flow rate through a single hole if the thickness of the basket wall is greater than ten times the diameter of the hole if the Reynolds number is approximately 1. If the Reynolds number is 10, then the entrance length is 1.5 diameters and the wall thickness needs to be about 15 times the hole diameter for Equation 1.21 to be valid. With a Reynolds number of 100, the entrance length is 8.7 diameters and the thickness of the basket wall would need to be approximately 90 times the diameter of the hole before equation 1.21 would give reasonable results.

### 1.3.2 The Second Region of Fiber Growth

When the fiber enters the second region, two forces act upon the fiber: centripetal force and aerodynamic drag forces. The previous section derived the resulting flow rate through a single hole in the basket wall. As the melt passes through the hole and then exits the hole, an assumption must be made of the behavior of the fiber.

As a first approximation, assume that the surface tension in the molten material is enough to hold the fiber in a stream the same diameter of the hole in the basket. In the absence of any transverse forces, the flow of the molten material will be as shown in Figure 1-8. This assumption requires that the flow rate throughout the length of the fiber is constant. As a result, the continuity equation is true at any point along the fiber:

$$\rho \cdot A \cdot v = \text{Const} = W \quad (1.22)$$

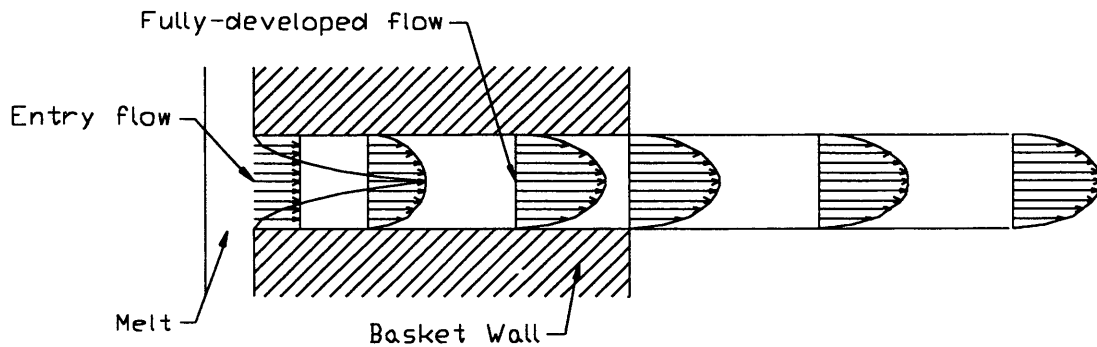


Figure 1-8

Flow of molten material without any transverse forces.

As the basket rotates, the viscosity of the air causes the air immediately adjacent to the surface of the basket to begin to move with the basket. This is the “no-slip” boundary condition requirement. At an infinite distance from the disk, the fluid is stationary. As the fiber grows away from the surface of the basket, the air begins to have a velocity relative to the fiber. This relative motion creates drag forces upon the fiber and, as a result, the fiber begins to bend. The angle of the bend is a function of the ratio between the centripetal forces and the drag forces.

In order to determine the aerodynamic forces acting on the fiber, it is necessary to examine the boundary layer around the spinning basket. The velocity profile around the

basket can be determined by solving the Navier-Stokes equations of motion for a rapidly spinning disk. Schlichting (1979) gives detailed derivations of this solution process, so it won't be repeated here. The result for a disk spinning in an infinite fluid is:

$$u = \frac{r_{Basket}^2 \cdot \omega}{r} \quad (1.23)$$

where  $u$  is the velocity of the air,  $r_{Basket}$  is the radius of the outer surface of the basket,  $\omega$  is the angular velocity of the basket, and  $r$  is the distance from the surface of the basket.

Figure 1-9 is a plot of the dimensionless results for this equation using the dimensionless variables  $u/u_1$  and  $r/r_1$ . This plot shows that the velocity drops off rapidly as the distance from the surface of the disk increases. Since the fiber is attached to the basket, it has the same velocity as the surface of the disk. The relative air velocities that the fiber feels is zero at the surface of the disk and equal to the velocity of the disk at an infinite distance. Figure 1-10 shows the dimensionless velocity relative to a fiber mounted to the surface of a disk spinning in an infinite fluid.

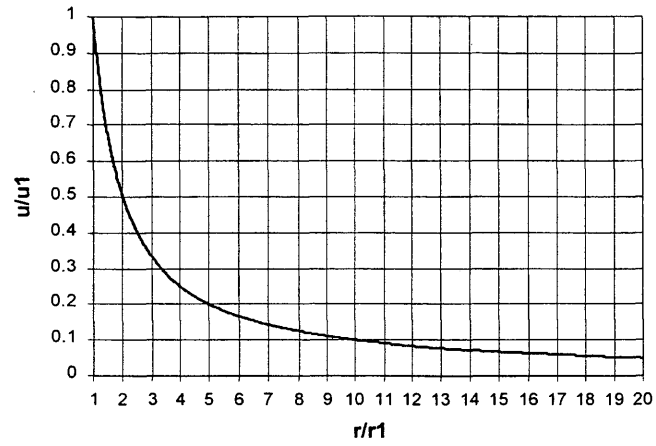


Figure 1-9

Velocity profile around a spinning disk in an infinite fluid.

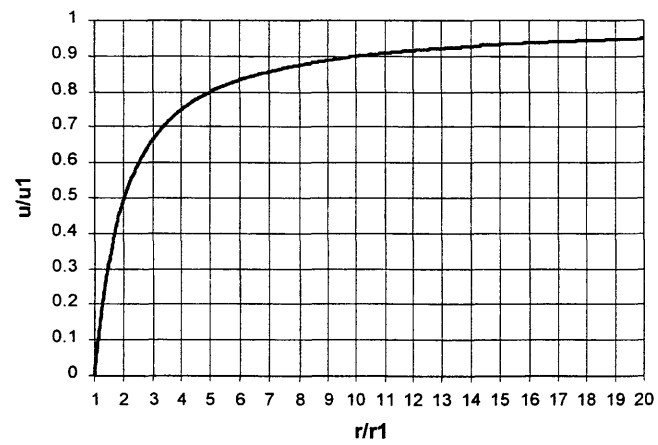


Figure 1-10

Relative velocity around a spinning disk in an infinite fluid.

If the spinning disk is enclosed within a stationary outer wall, as it is in the manufacturing process, the velocity profile around the spinning disk changes. Solving the Navier-Stokes equations for this situation yields the following velocity profile:

$$\frac{u}{u_1} = \frac{\chi}{1 - \chi^2} \cdot \frac{1 - x^2}{x} \quad (1.24)$$

where  $u$  is the velocity at some point in space, and  $u_1$  is the velocity at surface of disc.

There are two dimensionless variables in equation 1.24. These are defined to be:

$$\chi = \frac{r_1}{r_2} \quad (1.25)$$

and

$$x = \frac{r}{r_2} \quad (1.26)$$

where  $r$  is the distance from surface of disk,  $r_1$  is the radius of disc, and  $r_2$  is the radius of outer wall.

If the results for this velocity profile are plotted using a dimensionless distance, the results can be applied to any case of a rotating disk within a stationary outer wall.

This dimensionless distance variable is:

$$\frac{x'}{s} = \frac{r - r_1}{s} \quad (1.27)$$

where  $s$  is the difference between the two radii ( $r_2 - r_1$ ).

Plotting the results from equation 1.24 versus equation 1.27 yields Figure 1-11.

This plot shows that the velocity profile depends upon the gap between the rotating disc

and the outer wall as well as the distance from the rotating disk. When the gap is small, the velocity profile approaches linear. When the gap is large, the velocity profile approaches the velocity profile for the disc spinning in an infinite fluid. The shape of the velocity profile is important because it determines the aerodynamic forces acting on the fiber and as a result, the path of the fiber and the stresses within the fiber. Figure 1-12 presents the velocity relative to a fiber attached to the spinning disk. It is this relative velocity which creates the drag forces acting on the fiber.

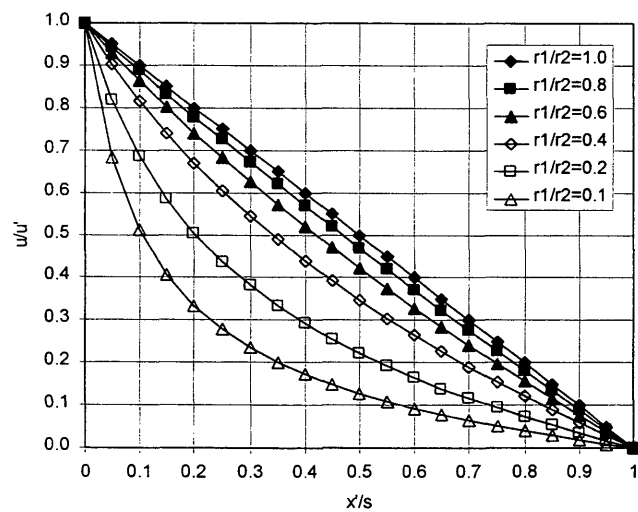


Figure 1-11

Dimensionless velocity profile around a spinning  
disk surrounded by a stationary wall.

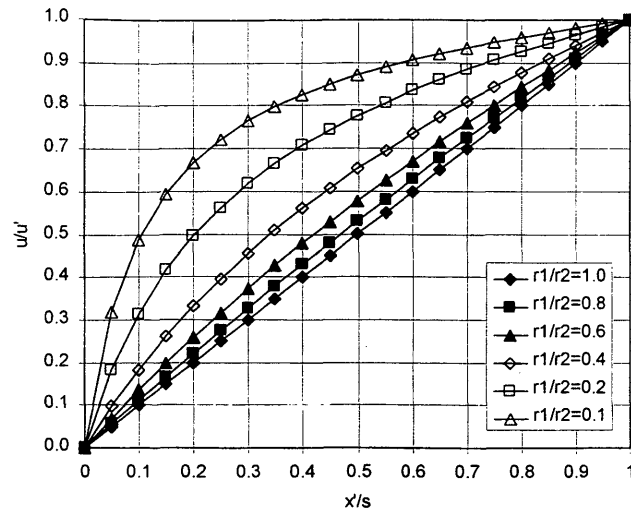


Figure 1-12

Dimensionless relative velocity around a spinning disk surrounded by a stationary wall.

### 1.3.3 The Third Region of Fiber Growth

In the third region of fiber growth the fiber is essentially parallel with the mean velocity of the air stream. The forces acting on the fiber are created by the friction forces created by the viscosity of the air stream passing along the length of the fiber. In addition, the turbulence in the air stream creates forces that act perpendicular to the axis of the fiber.

When the fiber is in its equilibrium position, the axial velocity creates a force that acts along the axis of the fiber and tends to straighten the fiber. In a laminar velocity

field, the fiber will align itself with the flow and, once it reaches its equilibrium position, it will remain there. Ziabicki (1985) presents a relationship to determine the viscous forces acting on a continuous fiber moving through an air stream. This relationship is:

$$F_{Axial} = \frac{C_D \cdot \pi \cdot d_f \cdot l \cdot \rho_{Air} \cdot U^2}{2} \quad (1.28)$$

where the drag coefficient is:

$$C_D = 0.41 \cdot Re^{-0.61} \quad (1.29)$$

and the Reynolds number is:

$$Re = \frac{\rho_{Air} \cdot d_f \cdot U}{\mu} \quad (1.30)$$

In equation 1.28, 1.29, and 1.30  $F_{Axial}$  is the axial force on fiber,  $d_f$  is the diameter of the fiber (m),  $l$  is the length of fiber (m),  $\rho_{Air}$  is the density of air,  $U$  is the axial velocity, and  $\mu$  is the viscosity of air.

If the fiber is disturbed from its equilibrium position, the axial velocity is no longer aligned with the fiber. This creates a velocity across the cylinder. In addition, the turbulent fluctuations in velocity perpendicular to the axis of the fiber also create forces which cause the fiber to move from its equilibrium position.

White (1974) presents a relationship for the force on a cylinder created by a velocity perpendicular to the axis of the cylinder. This relationship is:

$$F_{Transverse} = \frac{C_D \cdot d_f \cdot l \cdot \rho_{Air} \cdot W^2}{2} \quad (1.31)$$

where  $F_{\text{Transverse}}$  is the transverse force on fiber,  $d_f$  is the diameter of the fiber,  $l$  is the length of fiber,  $\rho_{\text{Air}}$  is the density of air, and  $W$  is the velocity perpendicular to the axis of the cylinder.

The drag coefficient in equation 1.31 depends upon the Reynolds number and is determined using the following relationships:

$$\text{Re} = \frac{\rho_{\text{Air}} \cdot d_f \cdot W}{\mu} \quad (1.32)$$

$$\text{if } \text{Re} \leq 1: \quad C_D = \frac{8 \cdot \pi}{\text{Re} \cdot \left[ 0.5 - 0.577216 + \text{Ln} \left( \frac{8}{\text{Re}} \right) \right]} \quad (1.33a)$$

$$\text{if } 1 < \text{Re} \leq 2 \cdot 10^5 \quad C_D = 1 + 10 \cdot \text{Re}^{-0.6} \quad (1.33b)$$

The forces resulting from the use of Equations 1.28 through 1.33 are the major forces acting on a fiber in the manufacturing process and in the laboratory wind tunnel used in this study and discussed in Section 4.2. Now that these correlations have been developed, it is possible to begin to examine how to model the motion of a single fiber.

#### **1.4 Objectives**

The overall goal of the current research project is to improve the understanding of how a fiber is formed by the forces present in the rotary fiber spinning process. In an attempt to obtain the overall research goal, the objectives of this thesis are:

1. To develop a simple method to model the motions of a single fiber in a turbulent velocity field.
2. To use the simple model to develop information that can be used to develop more complete models in the future.

Achieving these objectives will provide tools that will help future research to gain a better understanding of the process of discontinuous fiber formation.

## Chapter 2

### MODELING THE FIBER: LITERATURE SURVEY

#### 2.1 Analytical Approach

In order to analyze the motion of a fiber, it is necessary to determine how the fiber will be modeled. It is reasonable to assume that the properties of the fiber have a large affect upon the motion of the fiber within the turbulent flow of the manufacturing process. The most important properties appear to be the modulus of elasticity (Young's Modulus) of the fiber, the moment of inertia of the fiber, the tension within the fiber, and the length of the fiber. Any attempt to model the motion of a fiber should include these parameters.

The turbulence fluctuations in the wind tunnel occur in all three directions. For a complete model, it is necessary to model the forces in all three directions. Since the velocities and the temperatures in the wind tunnel are relatively low, any stretching of the fiber will be ignored.

The second simplifying assumption is that the fiber material is isotropic. As a result, the response of the fiber is independent of the direction of an applied force. For example, the motion of the fiber in the horizontal and vertical directions will be the same under the same applied force. This assumption makes it possible to limit the analysis to

only fluctuations in the vertical direction. The results from this analysis can then be applied to the turbulent fluctuations in the horizontal plane.

There are many methods that can be used to model the motion of the fiber. Perhaps the most obvious is to treat the fiber as a string and then to solve the partial differential equations (PDE) that describe the vibration of a string. A second possible method is to treat the fiber as a cantilever beam and solve PDEs for the vibration of a beam.

While each of these methods is useful to some extent, each has some important shortcomings that make them difficult to apply to the problem of modeling the motion of a single fiber. These two models and the shortcoming inherent in each method are described in the next sections.

### 2.2.1 Solving the String PDE

One common problem found in engineering literature is the vibration of a string (Figure 2-1). One assumption that governs the use of the string model is the fact that a string cannot support a bending moment. The only stress present in the string is a tensile force. The vibration of a string can be described by a single PDE of the following form (Bland, 1960; Wylie, 1982; Rao, 1995):

$$\frac{\partial}{\partial x} \left[ P \cdot \frac{\partial w(x,t)}{\partial x} \right] + f(x,t) = \rho(x) \cdot \frac{\partial^2 w(x,t)}{\partial t^2} \quad (2.1)$$

where  $P$  is the tension in the string,  $x$  is the position from the origin,  $f(x, t)$  is an external force applied to the fiber,  $\rho(x)$  is the mass per unit length of the string, and  $w(x, t)$  is the vertical position of the string. In this form, both the tension and the diameter of the string can vary along the length of the string. For a fiber with a uniform diameter, equation 2.1 reduces to:

$$\frac{\partial}{\partial x} \left[ P \cdot \frac{\partial w(x, t)}{\partial x} \right] + f(x, t) = \rho \cdot \frac{\partial^2 w(x, t)}{\partial t^2} \quad (2.2)$$

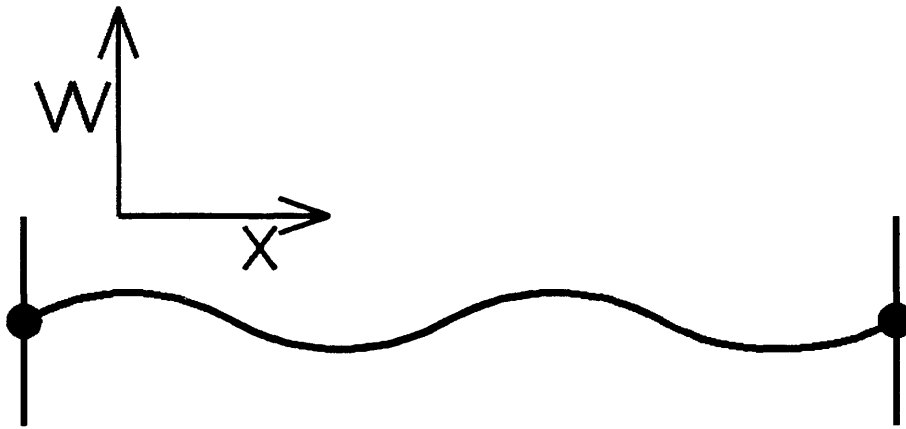


Figure 2-1

A vibrating string problem.

The fact that a fiber in the manufacturing process is subjected to shear stresses acting along the length of the fiber and that the diameter of the fiber gets smaller

indicates that this is an appropriate method to use to model the motion of the fiber.

However, there are two difficulties with this method.

The first difficulty encountered when solving the string PDE is determining the appropriate boundary conditions to use. The typical boundary conditions used to solve string equations are two fixed endpoints. This means that both ends of the string are fixed in space. It is not possible to model the motion of a fiber in the rotary spinning process in this way since only one end is fixed. The free end is free to move in space and its position is a function of the forces acting upon it.

There are several other boundary conditions that can be used instead of two fixed ends. For example, one end may be fixed and the other end connected to a spring (Figure 2-2). This combination of boundary conditions may be an acceptable model of the fiber in the manufacturing process or of a fiber in a wind tunnel. Before this arrangement can be solved, it is necessary to determine the spring constant. This information must come from an analysis of the aerodynamic forces acting on the fiber.

The second shortcoming lies in the external force acting upon the fiber. The turbulence present in the velocity field is random. It does not consist of a few frequencies that can be modeled using a simple Fourier series. As a result, the process is stochastic process and yields a stochastic PDE. Solving stochastic PDE's requires different procedures than solving regular PDE's. If possible, it would be desirable to be able to model the fiber using more simple methods. In addition, it is necessary to determine how the force on the fiber is related to the turbulent velocities present in the air stream.

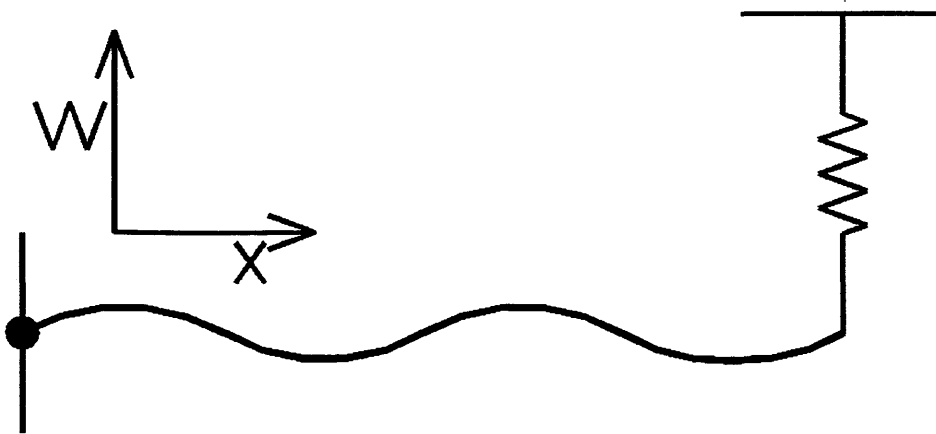


Figure 2-2

A vibrating string with one fixed end.

While the string model appears like a good way to model a single fiber, there are three major questions about its use. The first is the fact that the string model does not include any properties such as the modulus of elasticity. If section properties are important, the string model cannot account for them. The second question is how to model the boundary condition of the free end of the fiber. It is necessary to determine the spring constant before the equation can be solved. The third question is how to model the random external forces created by the turbulence in the air stream. Again, it is necessary to determine how the forces are related to the turbulent velocities present in the velocity field before this model can be solved.

### 2.3 Solving the Cantilever Beam PDE

A second method that may be used to model a single fiber is to treat the fiber as a cantilever beam (Figure 2-3). The vibration of beams is commonly studied and there are many papers that discuss the vibration of cantilever beams. There are also many studies that are concerned with the nonlinear vibration of beams (Nayfeh, 1995). One important factor in these studies is the fact that the beams are self-supporting. When examining fibers with diameters of less than  $100\mu\text{m}$ , the fibers cannot support their own weight unless the length of the fiber is very short.

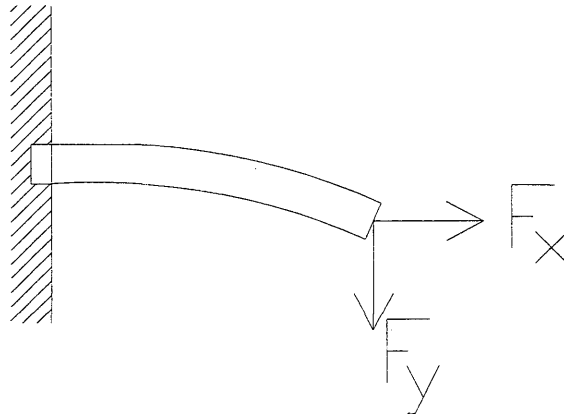


Figure 2-3

The cantilever beam model.

The general PDE for a cantilever beam is (Wylie, 1982; Rao, 1995):

$$\frac{\partial^2}{\partial x^2} \left[ E \cdot I(x) \cdot \frac{\partial^2 w(x,t)}{\partial x^2} \right] + \rho \cdot A(x) \cdot \frac{\partial^2 w(x,t)}{\partial t^2} = f(x,t) \quad (2.3)$$

where  $E$  is the modulus of elasticity,  $I$  is the cross-sectional moment of inertia,  $\rho$  is the density of the material,  $A(x)$  is the cross-sectional area,  $w(x,t)$  is the vertical displacement, and  $f(x, t)$  is the external force acting on the beam. If the beam is uniform, then equation 2.3 reduces to:

$$E \cdot I(x) \cdot \frac{\partial^4}{\partial x^4} w(x,t) + \rho \cdot A \cdot \frac{\partial^2}{\partial t^2} w(x,t) = f(x,t) \quad (2.4)$$

Two initial and four boundary conditions are required to solve this equation. The two boundary conditions for the fixed end of the beam are:

$$w(0,t) = \dot{w}(0,t) = 0 \quad (2.5)$$

The boundary conditions for the free end of the beam are typically a bending moment of zero at the free end,

$$E \cdot I \cdot \frac{\partial^2 w}{\partial x^2} = 0 \quad (2.6)$$

and a shear force of zero at the free end:

$$\frac{\partial}{\partial x} \left( E \cdot I \cdot \frac{\partial^2 w}{\partial x^2} \right) = 0 \quad (2.7)$$

The external force in equation 2.4 is due to the turbulence in the velocity field. As with the string model, this results in a stochastic differential equation. It is desirable to avoid the stochastic conditions if possible.

The fibers that are to be modeled have diameters less than  $100\mu\text{m}$ . A fiber diameter of this magnitude results in a moment of inertia of around  $10^{-23}$ - $10^{-19}\text{m}^4$ . With

these dimensions, a beam cannot support its own weight. When the equation is solved with a moment of inertia this small, the resulting deflections are much too large and violate the assumptions made for its development. This suggests that this equation cannot be used.

If a cantilever beam is subjected to an axial load, then the beam has a different deformation than a regular cantilever beam. Modeling a cantilever beam with an axial force is useful when modeling cables since the cantilever beam model includes section properties. The general equation for a uniform beam with an axial load is:

$$\frac{\partial^2}{\partial x^2} \left[ E \cdot I(x) \cdot \frac{\partial^2}{\partial x^2} w(x,t) \right] + \rho \cdot A \cdot \frac{\partial^2}{\partial t^2} w(x,t) - P \cdot \frac{\partial^2}{\partial x^2} w(x,t) = f(x,t) \quad (2.8)$$

The use of Equation 2.8 is preferable to the use of Equation 2.2 since it includes the section properties of the fiber. However, since the magnitude of I is so small with the fibers that are being examined, the displacements may be too great and the use of equation 2.8 may be invalid.

One important factor in equation 2.8 is the product of the modulus of elasticity and the moment of inertia. The modulus of elasticity is a function of the material of which a beam or fiber is made. The moment of inertia is function of the diameter of the fiber or beam. For a circular beam or fiber, the moment of inertia is:

$$I = \frac{\pi \cdot d_{fiber}^4}{64} \quad (2.9)$$

If the diameter of a beam is decreased by a factor of two, then the moment of inertia decreases by a factor of eight. In order for a fiber or beam to have the same motion, it is necessary for the modulus of elasticity to increase by a factor of eight. This fact suggests that there is a point where the size of a fiber is so small that the modulus of elasticity is not significant. When this is the case, then equation 2.8 reduces to:

$$\rho \cdot A \cdot \frac{\partial^2}{\partial t^2} w(x, t) - P \cdot \frac{\partial^2}{\partial x^2} w(x, t) = f(x, t) \quad (2.10)$$

Equation 2.10 is the same as equation 2.2 if the axial force on the fiber/beam (P) is assumed to be constant.

#### 2.4 Summary of PDE Methods

There are several questions that surround the use of the string PDE and the cantilever beam PDE to model the motion of a fiber. These are:

1. The forces acting on the fiber under study are the result of air passing along the length of the fiber and across the axis of the fiber. It is desirable to determine if the published correlation between aerodynamic forces and velocities produce realistic forces. This is especially important since the dimensions of the fibers are less than 100 $\mu$ m.
2. The effect of a material's modulus of elasticity and moment of inertia are unknown. If the effect of these two factors is insignificant, then the fiber can be modeled as a string. If the effect is significant, the fiber needs to be

modeled as a beam. In addition, the forces and displacements may be such that this equation can not be used to accurately model this system.

3. The turbulence present in the velocity field results in a stochastic differential equation. Solving stochastic problems is a field unto itself and is considered beyond the scope of this study. It is desirable to model the fiber without the use of stochastic models if possible.

Because of the questions involved with the use of both the string model and the beam model, a simpler approach will be used to model the motion of the fiber. This approach will be a kinematic approach that models the fiber as rigid cylindrical elements connected by hinges. If this kinematic method reasonably models the motion of a single fiber, it may help to determine when the string model and when the beam models are appropriate to use.

## Chapter 3

### MODELING THE FIBER: KINEMATIC APPROACH

#### 3.1 Analytical Approach

The previous chapter discussed modeling the fiber as a string and as a beam. The conclusion of the discussion was that the effects of material properties such as the modulus of elasticity have an unknown effect upon the motion of small fibers. In addition, the aerodynamic forces that result from the random turbulent fluctuations play an important part in the motion of the fibers. The randomness of these forces result in stochastic differential equations. In an attempt to avoid having to solve these stochastic equations, a kinematic approach will be used to model the motion of a single fiber in the wind tunnel.

In this kinematic approach, the fiber is assumed to begin at some equilibrium position at time zero and the forces acting upon the fiber are determined. Once these forces are known, the acceleration, velocity, and position resulting from these applied forces are then calculated. These results then become the initial conditions for the subsequent time step.

The first and simplest model will assume that a fiber can be modeled as a rigid cylinder with one hinged end and one free end (Shigley, 1967). Aerodynamic forces will

be applied to the cylinder and the motion of the fiber determined. The results for this numerical study will then be compared to high-speed videotaped data to determine if the frequency and the magnitude of the fluctuations agree. In addition to the single degree of freedom model, a numerical study of a model with two degrees-of-freedom will also be performed.

If the results from the first two models are not acceptable, a model with four degrees-of-freedom will be studied. As the degrees of freedom increase, the motion of the model should approach the motion of the fiber.

### 3.2 Single Degree of Freedom Kinematic Analysis

The first modeling approach assumes that the fiber can be modeled as a single rigid, cylindrical element attached to the airfoil by a hinge (Figure 3-1). The hinged connection provides no resistance to movement in this model. Any force that acts parallel to the axis of the fiber creates a tension within the fiber. Any force that acts perpendicular to the axis of the fiber causes rotation about the hinge connection. As a result, it is necessary to separate the force vectors into their radial (acting along the fiber axis) and their tangential (acting in the angular direction) components to determine the motion of the fiber.

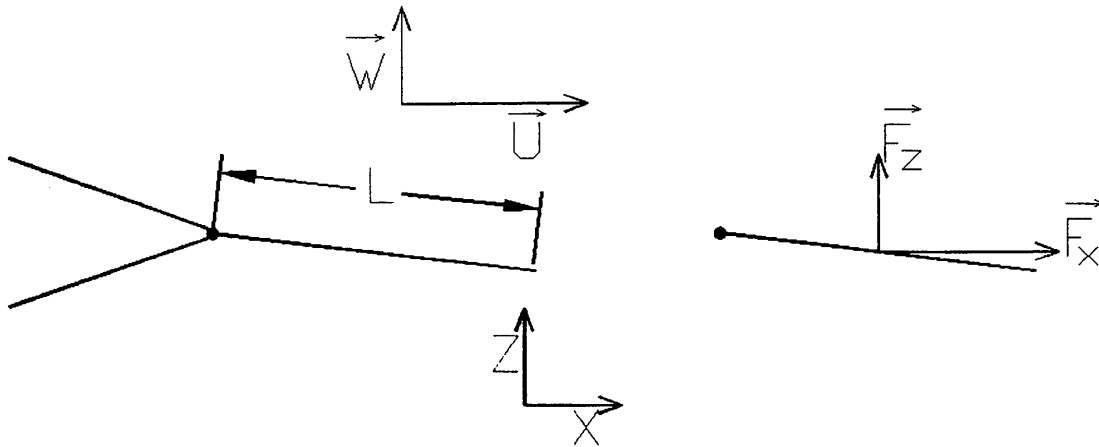


Figure 3-1

Fiber model with a single degree-of-freedom.

### 3.2.1 Gravitational Forces

If the fiber were immersed in a one-dimensional laminar velocity field, the fiber would move to an equilibrium position. This equilibrium position would be the position at which the torque resulting from the gravitational force would be opposed by the torque created by the horizontal force component (Figure 3-2). In a two-dimensional laminar velocity field, the fiber would reach an equilibrium position in which at which the torque resulting from the gravitational force would be opposed by the torque created by the both the horizontal and vertical force components.

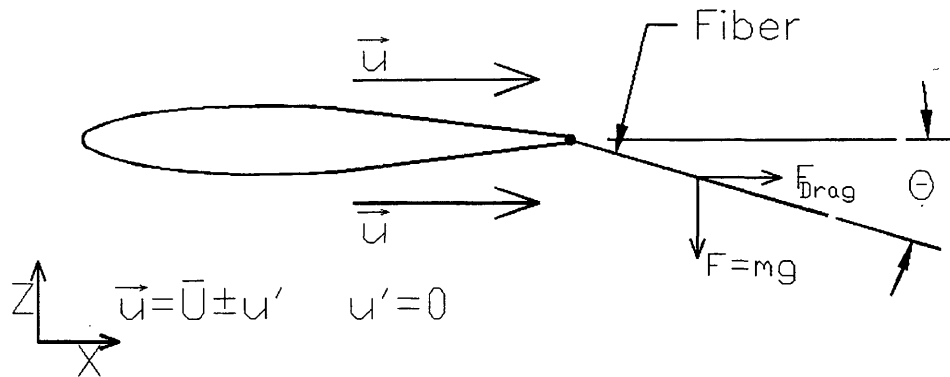


Figure 3-2

Equilibrium position in a steady, laminar velocity field.

Figure 3-2 indicates that the drag force created by the  $U$ -velocity vector has two components acting on the fiber. The first component, which acts along the axis of the fiber, creates a tensile force in the fiber and is found using the equation:

$$F_{\text{Radial}} = F_{\bar{U}} \cdot \cos(\theta) \quad (3.1)$$

The second force acts perpendicular to the axis of the fiber and creates a moment that opposes the moment created by gravitational forces. This force is found using the equation:

$$F_{\theta} = F_{\bar{U}} \cdot \sin(\theta) \quad (3.2)$$

The angle theta ( $\theta$ ) is the angle created by the weight of the fiber and is given by the arctangent of the ratio of the gravitational force to the drag force (Figure 3-3).

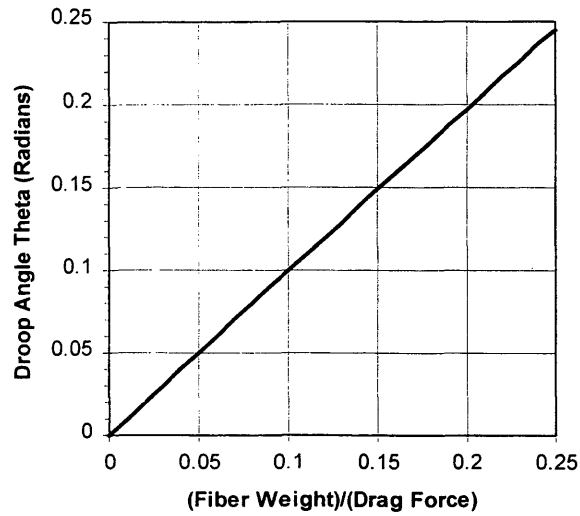


Figure 3-3

Angle theta as a function of the ratio of gravity force to drag force.

Figure 3-3 indicates that if the force ratio is less than 0.25, the angle theta will be less than 0.25 radians. If the angle theta is small enough, equations 3.1 and 3.2 will simplify to:

$$F_{Radial} = F_{\bar{U}} \cdot \cos(\theta) \approx F_{\bar{U}} \quad (3.3)$$

$$F_{\theta} = F_{\bar{U}} \cdot \sin(\theta) \approx 0 \quad (3.4)$$

Figure 3-4 illustrates the error incurred by using equation 3.3 instead of equation 3.1.

This figure shows that the error is less than 5% for angles less than  $17^{\circ}$  (0.30 radians) and less than 2.5% for angles less than  $13^{\circ}$  (0.23 radians). This suggests that the weight of the fiber can be neglected if the force ratio is less than 0.20.

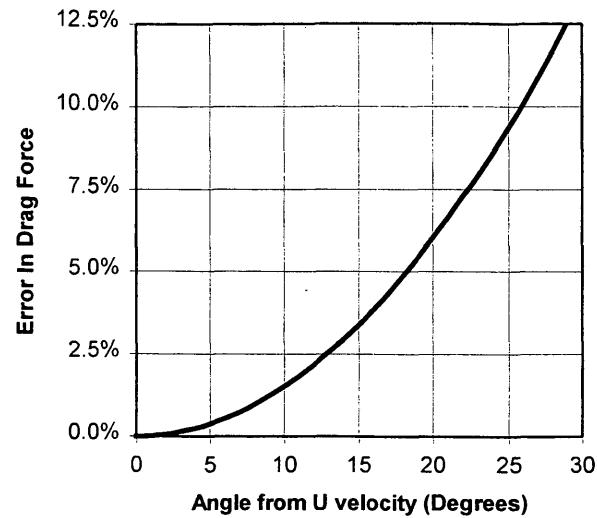


Figure 3-4

Error using equation 3.3 rather than 3.1 to determine drag force.

The largest test fiber in this study has a diameter of  $47\mu\text{m}$  and a length of 0.102 meters with a weight of  $1.604 \cdot 10^{-7}$  N. The lowest velocity in this test is on the order of 10 m/s. Using equation 1.28 with this combination of velocity and fiber diameter yields an axial force ( $F_U$ ) of  $4.361 \cdot 10^{-5}$  N and a gravitational force to drag force ratio of 0.004. Since this ratio is so small, it can be concluded that the gravitational force on the fiber can be ignored.

### 3.2.2 Radial and Tangential Velocity Vectors

The velocity in the air stream can be expressed as a vector with two or three components. For this study only a two-dimensional flow field will be considered. In order

to determine the motion of the fiber it is necessary to determine two forces acting on the fiber: the radial force and the tangential force. To do this, it is necessary to determine the velocity component acting parallel to the axis and the velocity component acting perpendicular to the axis. Once these two components are determined, equations 1.28, and 1.31 can be used to determine the forces acting on the fiber.

The data that will be used in the numerical simulation consists of a mean axial velocity ( $\vec{U}$ ) and a mean vertical velocity ( $\vec{W}$ ). Unless the position angle of the fiber is exactly zero, then each of these velocities contribute to the radial and tangential forces acting on the fiber. The total radial velocity vector can be found using equation 3.5:

$$V_{Radial} = |\vec{U}| \cdot \cos(\theta) + |\vec{W}| \cdot \cos\left(\frac{\pi}{2} - \theta\right) \quad (3.5)$$

The total tangential velocity vector can be found using equation 3.6:

$$V_{\theta} = |\vec{U}| \cdot \sin(\theta) + |\vec{W}| \cdot \sin\left(\frac{\pi}{2} - \theta\right) \quad (3.6)$$

The results from equation 3.5 and 3.6 are used with equations 1.28 and 1.31 to determine the forces acting on the fiber.

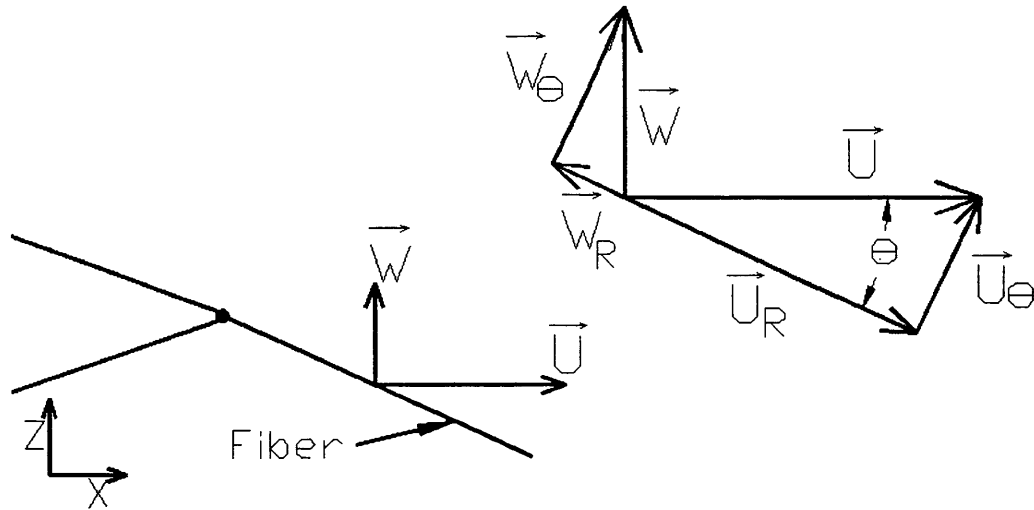


Figure 3-5

Velocity vector diagram.

### 3.2.3 Relative Fiber Velocity

One important factor that must be taken into account is the velocity of the fiber. The air velocities measured in the wind tunnel are with respect to a fixed point in the air stream. However, the fiber is not stationary. As a result, the velocity of the air with respect to the fiber is not the same as the velocity being measured in the air stream.

If both the fiber velocity vector and the tangential velocity vector are in the same direction, the relative velocity is less than calculated, and as a result, the force acting on the fiber is less. If the fiber velocity vector and the tangential velocity vector are in opposite directions, the relative velocity will be greater than calculated, and as a result, the forces acting upon the fiber will be greater.

The velocity of the center of the fiber element can be calculated as:

$$V_{Fiber} = \dot{\theta} \cdot \frac{l}{2} \quad (3.7)$$

The air velocity relative to the fiber is determined by the difference between the calculated tangential velocity and the fiber velocity:

$$V_{\theta Relative} = V_{\theta} - V_{Fiber} \quad (3.8)$$

This relative velocity is substituted into equations 1.31 to determine the tangential force ( $F_{\theta}$ ) acting upon the fiber.

Once the net radial (tension) forces and tangential forces are determined, the torque on the fiber is found. This is simply the tangential force times the lever-arm length, which is half of the element length:

$$T = F_{\theta} \cdot \frac{l}{2} \quad (3.9)$$

At this point, all of the forces acting on the fiber are defined. It is only necessary to substitute the torque into the equations of motion to be able to determine the motion of the fiber.

### 3.2.4 Equations of Motion

Like any other mass, the motion of the fiber can be defined with three parameters: acceleration, velocity, and position. In the case of the fiber rotating about a fixed point

the quantities of interest are angular acceleration ( $\ddot{\theta}$ ), angular velocity ( $\dot{\theta}$ ), and position ( $\theta$ ). These quantities are related as follows:

$$\ddot{\theta} = \frac{d\dot{\theta}}{dt} = \frac{d^2\theta}{dt^2} \quad (3.10)$$

$$\dot{\theta} = \frac{d\theta}{dt} = \int \ddot{\theta} \cdot dt \quad (3.11)$$

If the angular acceleration is integrated to get angular velocity, the following equation is obtained:

$$\dot{\theta} = \int \ddot{\theta} \cdot dt = \ddot{\theta} \cdot t + C \quad (3.12)$$

The constant in equation 3.12 is the initial angular velocity of the mass. As a result, equation 3.12 can be written as:

$$\dot{\theta}(t) = \ddot{\theta} \cdot t + \dot{\theta}_0 \quad (3.13)$$

Integrating equation 3.13 yields the equation for the position of the mass:

$$\theta(t) = \theta_0 + \dot{\theta}_0 \cdot t + \frac{1}{2} \cdot \ddot{\theta} \cdot t^2 \quad (3.14)$$

where  $\theta(t)$  is the position of the mass as a function of time,  $\theta_0$  is the initial position of the mass,  $\dot{\theta}_0$  is the initial velocity of the mass, and  $\ddot{\theta}$  is the acceleration of the mass at any given instant.

There is one more equation required to complete the equations of motion. Newton's law gives the relationship between acceleration and force. In rotational form this law is written as:

$$T = I \cdot \ddot{\theta} \quad (3.15)$$

where T is the torque on the mass and I is the mass moment of inertia about the center of rotation. For a cylindrical element rotating about one end, I can be found using equation 3.16:

$$I = \frac{1}{3} \cdot m \cdot l^2 \quad (3.16)$$

where m is the mass of the element and l is the length of the element. Rearranging equation 3.15 yields the equation to determine the angular acceleration of the fiber element around the hinge connection:

$$\ddot{\theta} = \frac{T}{I} \quad (3.17)$$

### 3.2.5 Numerical Simulation Technique

The motion of the fiber will be studied using a numerical simulation. In this approach, the equations outlined in the previous sections will be used to determine the motion of the fiber element at discrete time steps. The net force acting on the fiber at each instant will be determined and then the equations of motion used to determine the motion of the fiber during that time interval. At time zero, the initial position for the fiber

will be assumed to be a position of zero, a velocity of zero, and an initial acceleration of zero. At the end of each time step, the acceleration, the velocity, and the position of the fiber will be known. These values are then used as the initial values for the next time step.

The forces acting on the fiber are generated using velocity data sets taken in the wind tunnel. These data sets were acquired using a three-dimensional hot-wire anemometer and consist of 4096 velocity readings with a time interval of 0.0002 seconds between each reading. Velocity readings were made at 16 different positions downstream of the airfoil to which the fiber is mounted. This series of measurements allowed the characterization of the turbulence immediately downstream of the airfoil. This is the turbulence that would be acting on any fiber mounted to the airfoil.

The test fiber for all of the studies in this thesis is .102 m. This length of fiber was chosen because it fit the frame size of the high-speed video very well. For the single element model, the velocities recorded at the position corresponding to the center of the fiber, or 0.0508 m from the trailing edge of the airfoil will be used to generate the forces acting on the fiber.

The results for the simulation will be plotted as a function of time. The maximum and minimum displacements from the simulation will be compared to the videotaped movement of the fiber to determine if the model gives reasonable results. A Fast Fourier Transform (FFT) will be performed on the numerical results to determine the fundamental frequency of the motion. The resulting frequencies will also be compared to

the videotaped data to determine how well the numerical simulation agrees with the actual data.

### 3.3 Two Degree of Freedom Kinematic Analysis

Many assumptions and simplifications are made when modeling real systems. One of the biggest simplifications in modeling systems is the use of discrete elements to model a continuous system. Usually the number of elements is increased until the results approach the actual system. In order to increase the accuracy of the numerical simulation in this, a model made up of two elements will be examined in addition to the single element model (Figure 3-6).

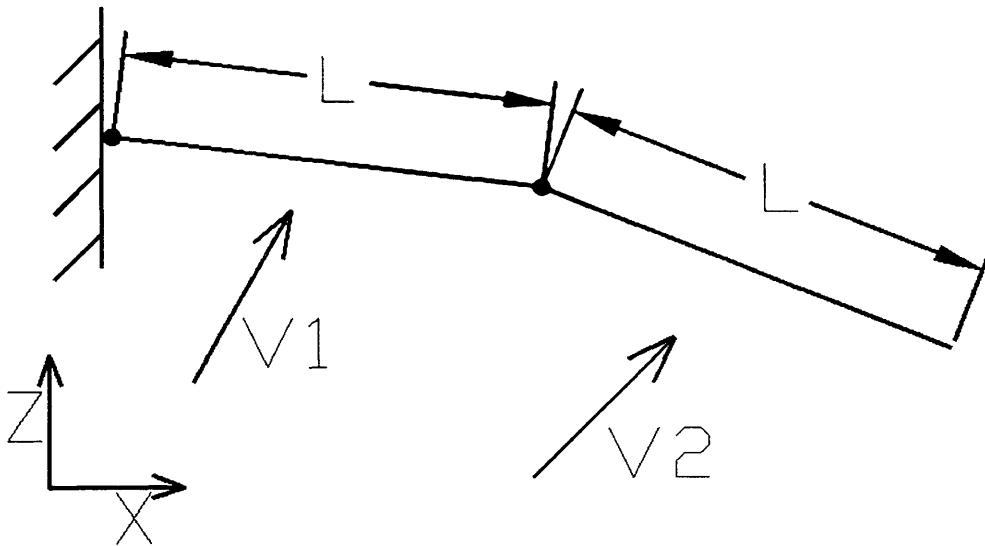


Figure 3-6

Two-element kinematic model.

The basic approach to the two-element model is the same as that taken for the single element model. However, there are some additional factors that must be taken into account in the more complex model. These factors are discussed below.

### 3.3.1 The Relative Velocity of the 2nd (End) Element

The forces acting on the last element are the same as the forces outlined for the single element model. There are several major differences that must be taken into account to obtain realistic results.

The procedure outlined for the single element provides the motion around the hinged connection. In the single element model, the hinged connection was fixed. In the two-element model, the hinged connection is moving. The primary effect of this movement is that it changes the relative tangential velocity of the air. In the single element model, the velocity of the fiber was determined to be:

$$V_{Fiber} = \dot{\theta} \cdot \frac{l}{2} \quad (3.7)$$

Again in writing this equation it is assumed that the end of the fiber is fixed in space.

Since the free end of the fiber can now move in the two-element model, equation 3.7 does not give the true velocity of the fiber. Instead, it gives the velocity relative to the hinged connection. In order to get the velocity about the inertial reference frame, it is necessary to add the velocity of the hinged connection to the relative velocity given by equation 3.7.

The hinged connection is at the end of the first element of the model. This element is assumed to be rigid, so the velocity of the hinged joint is:

$$V_{Hinge} = \dot{\theta}_1 \cdot l_1 \quad (3.18)$$

where  $\dot{\theta}_1$  is the angular velocity of the first element, and  $l_1$  is the length of the first element. Adding this velocity to the relative velocity given by equation 3.7 yields the true velocity for the second element:

$$V_2 = \dot{\theta}_1 \cdot l_1 + \dot{\theta}_2 \cdot \frac{l_2}{2} \quad (3.19)$$

The relative tangential velocity is now given by equation 3.20:

$$V_{n\theta Relative} = V_{n\theta} - V_n \quad (3.20)$$

where  $V_{2\theta Relative}$  is the relative tangential velocity for element n,  $V_{2\theta}$  is the tangential velocity for element n, and  $V_2$  is the velocity of fiber element n. As with the previous model, this relative velocity is used with equation 1.31 to determine the tangential force acting on the fiber element. Equation 3.9 can then be used to determine the torque on the element.

### 3.3.2 The Position and Velocity of the 2<sup>nd</sup> (End) Element

Equations 3.13 and 3.14 give the position and velocity of the second (end) element relative to the hinged connection. To get the actual position for the second fiber element it is necessary to add the position of the previous elements to that given by equation 3.14. The same is true to determine the actual velocity for the second element.

In the numerical study, it is not necessary to keep track of the actual position and velocity for each fiber element as long as the relative velocity for the last fiber is determined using equations 3.19 and 3.20. If these equations are used, it is possible to add the positions for each element together after the force calculations are made.

### 3.3.3 Relative Velocity of the 1<sup>st</sup> Element

The relative velocity of the first element is determined using equation 3.19:

$$V_1 = \dot{\theta}_1 \cdot \frac{l}{2} \quad (3.21)$$

As before, the value for  $V_1$  is substituted into equation 3.20 to determine the relative tangential velocity.

### 3.3.4 Forces Acting on the 1<sup>st</sup> Element

The tangential and radial forces acting on the first element are determined in the same manner as used for the other elements in the model. Once the velocity components and the position angle for the first element are known, equations 3.5 and 3.6 can be used to determine the tangential and radial forces acting on the fiber. Then the resulting torque can be determined.

Unlike the element with one free end, the inner elements have additional forces acting on them from the subsequent elements. Figure 3-7 gives a free body diagram for the first element of a two-element model. This figure shows that the radial and tangential

forces on the end element act upon the end of the first element and create an additional torque acting on the fiber.

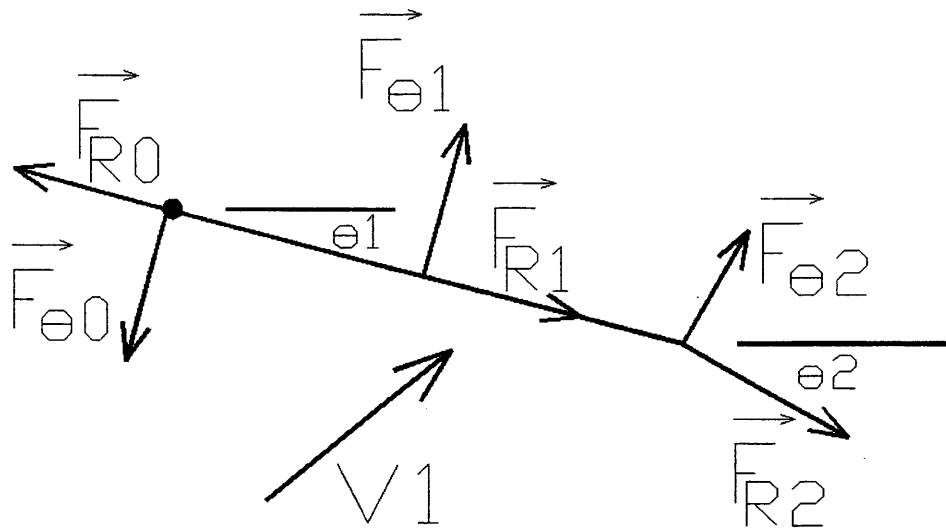


Figure 3-7

Free-body diagram for the 1<sup>st</sup> element in a two-element model.

The two forces acting on the end of the fiber create additional torque acting on the first element. The additional tangential and radial forces can be determined using the following equations:

$$F_{R21} = F_{R2} \cdot \cos(\theta_2 - \theta_1) + F_{\theta 2} \cdot \cos\left(\frac{\pi}{2} + (\theta_2 - \theta_1)\right) \quad (3.22)$$

$$F_{\theta 21} = F_{R2} \cdot \sin(\theta_2 - \theta_1) + F_{\theta 2} \cdot \sin\left(\frac{\pi}{2} + (\theta_2 - \theta_1)\right) \quad (3.23)$$

where  $F_{R21}$  is the radial force acting on element 1 from element 2,  $F_{\theta 21}$  is the tangential force acting on element 1 from element 2,  $F_{R2}$  is the radial force on element 2, and  $F_{\theta 2}$  is the tangential force acting on element 2. The torque due to the tangential force acting at the hinged end of the fiber is given by:

$$T_{21} = F_{\theta 21} \cdot l \quad (3.24)$$

where  $T_{21}$  is the torque due to forces acting on element 2,  $F_{\theta 21}$  is the tangential force due to forces on element 2, and  $l$  is the length of element. The net torque acting on the element is the sum of the two torque components:

$$T_{Net} = T_1 + T_{21} \quad (3.25)$$

where  $T_{Net}$  is the net torque acting on element 1.  $T_1$  is the torque due to forces acting on element 1, and  $T_{21}$  is the torque due to forces acting on element 2. The acceleration of element 1 is then determined using the following equation:

$$\ddot{\theta}_1 = \frac{T_{Net}}{I_1 + I_2} \quad (3.26)$$

The radial force (tension) in element 1 is the sum of the radial force due to the two different radial force components:

$$F_{R1Net} = F_{R1} + F_{R21} \quad (3.27)$$

### 3.3.5 Numerical Simulation Technique

The technique used to carry out the numerical simulation is basically the same as the process used to for the single element model. The initial position of each element is assumed to be a position angle of 0, a velocity of 0, and an acceleration of 0. Velocity data is used to determine net forces acting upon each fiber element and the resulting acceleration, velocity, and position are determined for each element using the equations outlined in the previous sections.

Other than the additional forces on the first element and the additional velocity in the last element, the only significant change is the velocity data that is used in the simulation. For this simulation, the velocity data taken at the point that corresponds with the center point of each element is used.

For example, if a fiber that is 0.102m long is modeled using two elements, the center of element 1 is 0.025m from the trailing edge of the airfoil and the center of element 2 is 0.076m from the trailing edge of the airfoil. The air velocity data taken 0.025m from the trailing edge of the airfoil is used as the air velocity acting on element 1 while the air velocity data taken 0.076m from the airfoil is used as the air velocity acting on element 2.

### 3.3.6 Numerical Stability

When the number of elements was increased to two elements, the mass moment of inertia of each element decreased by a factor of eight. The force decreased by a factor

of two since the length of each segment was halved. This resulted in the angular acceleration of each cylinder increasing by a factor of four. This increase in acceleration made the model unstable. This instability was removed by decreasing the time step used in the simulation.

Since the velocity data was obtained with a frequency of 5kHz, the individual velocity data points were separated by  $2.0 \times 10^{-4}$  seconds. However, the time step required for the two-element model to be stable was approximately  $0.5 \times 10^{-4}$  seconds. The shorter time step was obtained by linearly interpolating between adjacent data points. This method did not create information that was not included in the original data set. Ideally, new velocity data would be recorded using a probe with a higher frequency response.

### 3.4 Generalized Multi-Degree of Freedom Kinematic Analysis

The equations presented for the two-degree of freedom model can be generalized to apply to any multi-degree of freedom model. The generalized form of equation 3.19 is used to find the velocity of any element in the model:

$$V_n = l \cdot \sum_{i=1}^{n-1} \dot{\theta}_i + \dot{\theta}_n \cdot \frac{l}{2} \quad (3.28)$$

where  $V_n$  is the velocity of element n,  $l$  is the element length,  $n$  is the number of elements in model, and  $\theta_i$  is the angular velocity of element n. The relative tangential velocity any element is:

$$V_{i\theta Relative} = V_{i\theta} - V_i \quad (3.29)$$

where  $V_{i\theta\text{Relative}}$  is the relative tangential velocity for element  $i$ ,  $V_{i\theta}$  is the tangential velocity for element  $i$ , and  $V_i$  is the velocity of fiber element  $i$ . The radial and tangential forces acting on element  $i$  resulting from the force acting on element  $(i+1)$  is:

$$F_{R(i+1)i} = F_{R(i+1)} \cdot \cos(\theta_{(i+1)} - \theta_i) + F_{\theta(i+1)} \cdot \cos\left(\frac{\pi}{2} + (\theta_{(i+1)} - \theta_i)\right) \quad (3.30)$$

$$F_{\theta(i+1)i} = F_{R(i+1)} \cdot \sin(\theta_{(i+1)} - \theta_i) + F_{\theta(i+1)} \cdot \sin\left(\frac{\pi}{2} + (\theta_{(i+1)} - \theta_i)\right) \quad (3.31)$$

where  $F_{R(i+1)i}$  is the radial force acting on element  $i$  from element  $(i+1)$ ,  $F_{\theta(i+1)i}$  is the tangential force acting on element  $i$  from element  $(i+1)$ ,  $F_{R(i+1)}$  is the radial force on element  $(i+1)$ , and  $F_{\theta(i+1)}$  is the tangential force acting on element  $(i+1)$ .

The torque acting on element  $i$  due to the tangential force created by element  $(i+1)$  is:

$$T_{(i+1)i} = F_{\theta(i+1)i} \cdot l \quad (3.32)$$

where  $T_{(i+1)i}$  is the torque due to forces acting on element  $(i+1)$ ,  $F_{\theta(i+1)i}$  is the tangential force due to forces on element  $(i+1)$ , and  $L$  is the length of element  $i$ . The net torque acting on the element is the sum of the two torque components:

$$T_{Net} = T_i + T_{(i+1)i} \quad (3.33)$$

where  $T_{Net}$  is the net torque acting on element  $i$ ,  $T_i$  is the torque due to forces acting on element  $i$ , and  $T_{(i+1)}$  is the torque due to forces acting on element  $(i+1)$ . The acceleration of element  $i$  is then determined using the following equation:

$$\ddot{\theta}_i = \frac{T_{Net}}{I_i + I_{i+1} + \dots + I_n} \quad (3.34)$$

The radial force (tension) in element  $i$  is the sum of the radial force due to the two different radial force components:

$$F_{R1Net} = F_{R1} + F_{R21} \quad (3.35)$$

where  $F_{R1Net}$  is the net radial force (tension) in element  $i$ ,  $F_{R1}$  is the radial force in element  $i$  due to drag, and  $F_{R21}$  is the radial force on element  $i$  from element  $(i+1)$

The numerical simulation is performed in the same manner as used for the two-element model. The initial forces on the end element (the  $n$ th element) of the fiber are determined and used to determine the acceleration of the last element in the model.

The next step is to move to the  $(n-1)$  element and determine the forces acting on this element. These forces include the forces acting on the last element. The resulting acceleration, velocity, and position of this element is then determined.

The next element is to move to the  $(n-2)$  element and to repeat the same process to determine the forces acting on the element and the resulting acceleration. This procedure is repeated for every element and each time step in the model.

### 3.5 Summary of Kinematic Numerical Simulation

The kinematic fiber model uses the fundamental laws of motion to determine the angular acceleration, velocity, and position for each element within the fiber model. The accuracy of the model should increase as the number of elements used increases. One

drawback of increasing the number of elements is that the time step used in the simulation needs to decrease in order for the numerical model to remain stable.

Before it is possible to give the results for the numerical simulations, it is necessary to present some information about the velocity field in which the fiber is located. The next chapter presents the results of the turbulence data taken and determines several features of the flow field. The results of the numerical simulations will be presented in Chapter 7.

## Chapter 4

### EXPERIMENTAL METHOD

#### 4.1 Description of Test Fibers

The three different fibers that are used in this study have diameters of 12 $\mu\text{m}$ , 30 $\mu\text{m}$ , and 47 $\mu\text{m}$ . The length of the test fibers will be 102mm. This length was selected because it fit well within the aspect ratio of the picture recorded by the high-speed video system. The fibers are made of polypropylene, which has density of 910 kg/m<sup>3</sup> and an elastic modulus of 1.5x10<sup>9</sup> Pa.

#### 4.2 Closed-Loop Wind Tunnel Description

In order to model the motion of a single fiber, it was necessary to determine the characteristics of the turbulence present in the air stream in which the fiber was mounted. The tests were conducted in the test section of a closed-loop wind tunnel (Figure 4-1). The test section measures 0.203m x 0.203m. The duct between the nozzle and the test section was of sufficient length to result in a fully developed velocity profile in the test section.

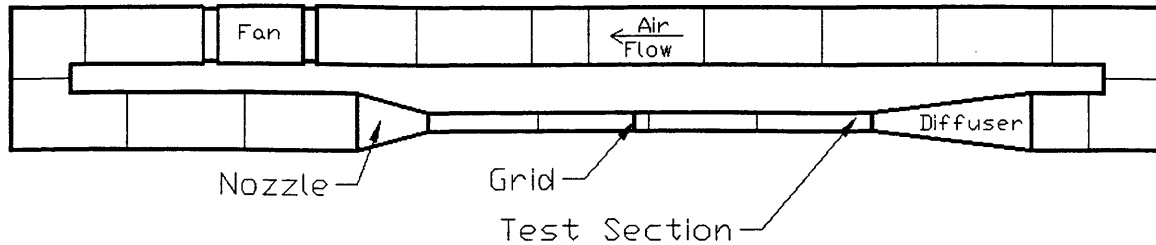


Figure 4-1

Closed-loop wind tunnel for fiber testing.

The primary factor that can be controlled in the wind tunnel is the speed of the fan. This control is obtained through the use of a variable frequency drive attached to the motor. This controller allows the fan speed to be varied from a low value of around 400 revolutions per minute (RPM) to its maximum value of approximately 2200 RPM. If nothing changes in the wind tunnel, then a fan will deliver the same amount of air if the fan speed is held constant. As a result, by controlling the fan speed, the axial velocity in the test section of the wind tunnel can be controlled.

The speed of the fan wheel is measured using an optical tachometer mounted in the inlet of the fan. This device shines a light onto the rotating fan shaft that has a piece of reflective tape mounted upon it. As the shaft rotates, the light reflects off the reflective tape and creates a pulse for each revolution of the shaft. The resulting pulses are counted and displayed on a digital display. The accuracy of the tachometer is  $\pm 1$  RPM. Since the flow volumetric rate is linearly related to the fan speed, the uncertainty in

the flow rate is relatively small. Perhaps even more important, it is very easy to develop the same conditions from one test to another.

Some means was needed to mount the test fibers in the test section of the wind tunnel. Ideally, the mounting method would not disturb the flow in the test section. Since flat bars, cylinders, and other simple geometric shapes shed regular vortex sheets (Wolochuk et al, 1996), a symmetric airfoil was chosen to minimize the wake from the fiber attachment point.

One additional benefit of the airfoil shape was that it allowed a force sensor to be mounted out of the air stream. The airfoil was mounted in the center of the test section with the axis of symmetry of the airfoil aligned with the center of the test section. The test fibers were then attached to the trailing edge of the airfoil.

In addition to the airfoil, a 1" (25.4 mm) grid was mounted in the wind tunnel. This placement of this grid creates a region of isotropic turbulence at the airfoil (Tresso, 1998). Isotropic turbulence is characterized by similar fluctuations in all three principal directions. This will help reduce the complexity associated with turbulence measurements. The distance between the grid and the airfoil was 1.88m.

In order to be able to understand the aerodynamic forces acting on the fiber it was necessary to characterize the turbulence created by this. This characterization was accomplished by using a three-dimensional hot-wire anemometer connected to a data-acquisition system to record the turbulent fluctuations present in the air stream.

### 4.3 Procedure for Measuring Velocity Data

To properly model the motion of the fiber, it was necessary to characterize the velocity and turbulence immediately downstream of the airfoil. This area is of primary interest since the fiber will be attached to the trailing edge of the airfoil. The fiber was not attached to the airfoil during the velocity measurements due to the fact that the fiber might hit and damage the fragile hot-wire anemometer.

Performing the measurements using this method requires the assumption that the velocity field will be largely unaffected by the fiber. Since the diameters of the fibers that will be tested are on the order of 10-50 $\mu\text{m}$ , the disturbances created by the fiber in the velocity field will be on that same order. This means that only the very small eddies and the very high frequencies of turbulence will be affected by the fiber. The integral scale or energy containing eddies correspond to the grid mesh dimension of 25.4mm. Since the majority of the turbulence energy is contained within eddies larger than the scale of the fiber, this assumption appears to be sound.

The three-dimensional hot-wire anemometer consists of three separate 3 $\mu\text{m}$  diameter hot-wire velocity sensors. These wires are oriented so that each one is subjected to only one of the three velocity components. Each of these three channels is recorded separately so that a complete record of the velocity is obtained.

The acquisition frequency used for this study was 15kHz. This resulted in a rate of 5kHz for each channel. There is no need for the acquisition frequency to be higher

than this rate since the probe is limited to 2500Hz. This is because the turbulent eddies associated with frequencies greater than 2500Hz are smaller than the size of the probe itself. Each data set consisted of 12,288 data points with 4096 data points for each velocity component.

For the high-speed video recording, single fibers will be attached to the trailing edge of an airfoil. For this analysis, the length of the fiber exposed to the air stream will be 102mm. Since the airfoil creates a disturbance in the flow, it is reasonable to assume that the velocity field varies downstream of the airfoil. Velocity measurements were made at 16 different positions downstream of the airfoil. These positions were spaced 6.4mm apart and corresponded to the length of the test fiber. The velocity data recorded at these different positions was then used as the velocities acting on the test fibers in the numerical simulations.

The velocity measurements and the resulting turbulent parameters will be presented in Chapter 5.

#### 4.4 Video Recording Procedure

The motion of three different test fibers mounted in the wind tunnel was recorded using a high-speed video recorder. The video recording was then analyzed to determine the frequency of and magnitude of the fluctuations. Each test fiber was subjected to three different fan speeds. Approximately 10 seconds of video were taken at each fan speed

with a recording rate of 500 frames per second. Since the frequencies that were expected were less than 30Hz, the speed was adequate to resolve the desired frequencies.

Each set of data was analyzed by counting the first and second modes of fluctuations. This was accomplished by dividing the recording into segments of about 1 second of length (500 frames) and then stepping through the video at a rate of about 1 frame per second while counting the fluctuations. This resulted in about eight sets of data that were then averaged.

In addition, the maximum positive and negative deflection of each fiber was recorded. This was done by projecting the videotaped picture onto a large piece of paper and then slowly stepping through the first second of each ten-second data set and marking the maximum displacement. After the maximum displacement was marked, the remaining data was played at a slightly faster rate (about 2 frames per second). If a displacement was larger than the previous maximum displacement, then the new maximum displacement was marked on the paper. Once the entire video recording for that fiber and fan speed combination was examined, the process was repeated for the mean position and the maximum negative displacement. The resulting frequencies and magnitudes are compared to the numerical simulations in the Chapter 7.

## Chapter 5

### CHARACTERIZATION OF THE VELOCITY FIELD ACTING UPON THE FIBER

#### 5.1 Velocity and Turbulence Measurements

Since the velocity field in which fibers are formed is turbulent, there is an added level of complexity in the analysis of the fiber motion. When the velocity in a turbulent flow is measured with a sensor having a fast response time, a constant value for velocity is not seen (Hinze 1974, White, 1974). Instead, rapid velocity fluctuations are observed. Figure 5-1 shows a typical result of the instantaneous velocity plotted against time for a laminar flow and a turbulent flow.

In general, a velocity field can be described in terms of three components  $u$ ,  $v$ , and  $w$ . Figure 5-2 shows the orientation of these three velocity components in the test section of the wind tunnel. Even though the turbulent flow varies constantly, it can be described in terms of an average part plus a fluctuating part. This fact can be stated in the form of:

$$u = \bar{U} + u' \quad (5.1a)$$

$$v = \bar{V} + v' \quad (5.1b)$$

$$w = \bar{W} + w' \quad (5.1c)$$

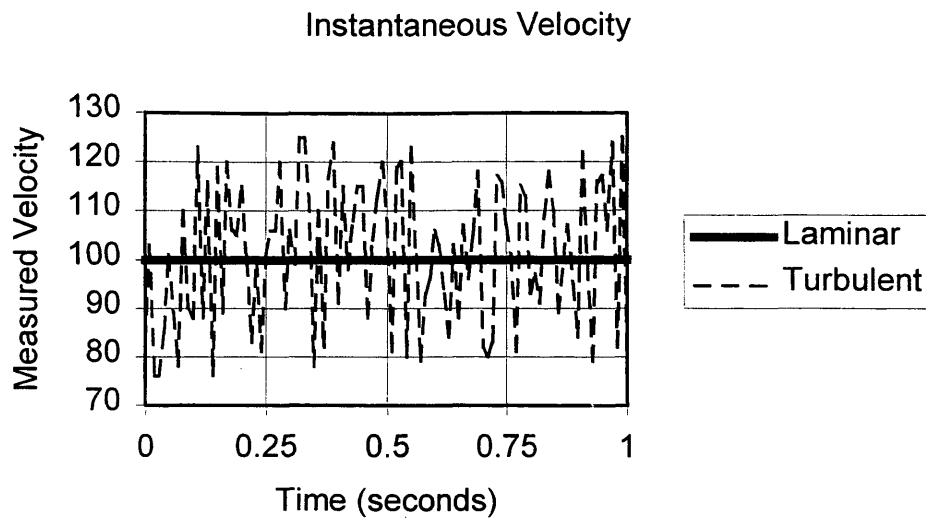


Figure 5-1

Instantaneous velocity for laminar and turbulent flow.

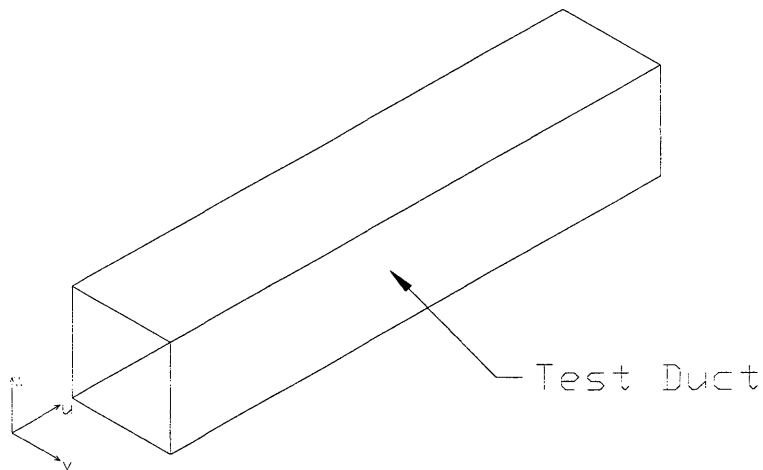


Figure 5-2

Wind tunnel test section and velocity component detail.

In the previous equations, the average velocity in each direction is represented by the  $\bar{U}$ ,  $\bar{V}$ , and  $\bar{W}$ . These values can be calculated from velocity measurements using the following equations:

$$\bar{U} = \frac{\sum_{i=1}^n u_i}{n} \quad (5.2a)$$

$$\bar{V} = \frac{\sum_{i=1}^n v_i}{n} \quad (5.2b)$$

$$\bar{W} = \frac{\sum_{i=1}^n w_i}{n} \quad (5.2c)$$

where  $u_i$ ,  $v_i$ , and  $w_i$  are individual velocity measurements and  $n$  is the number of measurements.

The fluctuating components are represented by the  $u'$ ,  $v'$  and  $w'$  values. According to Hinze (1974), the fluctuating components in these equations are the root-mean-square (RMS) value of the turbulent fluctuations in the velocity rather than the actual fluctuations. The RMS values can be determined from flow measurements and are calculated using the following equations:

$$u' = \sqrt{\frac{\sum_{i=1}^n (u_i - \bar{U})^2}{n}} \quad (5.3a)$$

$$v' = \sqrt{\frac{\sum_{i=1}^n (v_i - \bar{v})^2}{n}} \quad (5.3b)$$

$$w' = \sqrt{\frac{\sum_{i=1}^n (w_i - \bar{w})^2}{n}} \quad (5.3c)$$

These three equations are equal to the biased standard deviation. If the number of readings is large, they approach the value for the unbiased standard deviation of the velocities. As a result, they can be replaced by the unbiased standard deviation of each of the velocity components:

$$u' = \sqrt{\frac{\sum_{i=1}^n (u_i - \bar{u})^2}{n-1}} \quad (5.4a)$$

$$v' = \sqrt{\frac{\sum_{i=1}^n (v_i - \bar{v})^2}{n-1}} \quad (5.4b)$$

$$w' = \sqrt{\frac{\sum_{i=1}^n (w_i - \bar{w})^2}{n-1}} \quad (5.4c)$$

If this substitution is accepted, it provides a means to describe the turbulence in a statistical manner.

The turbulence intensity is defined as the fluctuating component divided by the mean component. In the case of flow in the wind tunnel, the intensity will be defined as the fluctuating component divided by the mean axial flow:

$$Intensity_U = \frac{u'}{\overline{U}} \quad (5.5a)$$

$$Intensity_V = \frac{v'}{\overline{U}} \quad (5.5b)$$

$$Intensity_W = \frac{w'}{\overline{U}} \quad (5.5c)$$

The frequency spectrum for the turbulence is obtained by performing a Fast Fourier Transform (FFT) on the velocity data sets. The FFT is a fast operation that can be used on sets of data that contain  $2^m$  values, where  $m$  is any integer. The FFT operation returns a complex value. When the magnitude of the complex value is plotted versus the frequency, a frequency spectrum is obtained. Any spikes indicate frequencies present in the data set. The equation used to perform the FFT is (Math Soft, 1998):

$$c_j = \frac{1}{\sqrt{n}} \cdot \sum_{k=0}^{n-1} v_k \cdot e^{2 \cdot \pi \cdot i \cdot \left(\frac{j}{n}\right) \cdot k} \quad (5.6)$$

where  $c_j$  is the value of element  $k$  and  $n$  is the number of elements in data set. The frequency that corresponds with element  $c_j$  is determined by:

$$f_k = \frac{k}{n} \cdot f_s \quad (5.7)$$

where  $f_s$  is the sampling frequency and  $n$  is the number of data points

## 5.2 Results of Measurements

The results of velocity measurements are presented in the following sections. Measurements were taken with four different fan speeds. The results are divided into two main parts: velocity and frequency. The velocity results are divided according to velocity direction and include the mean ( $U$ ,  $V$ , and  $W$ ) and fluctuating velocities ( $u'$ ,  $v'$ , and  $w'$ ) for the three principal directions, and the turbulent intensity ( $u'/U$ ,  $v'/U$ , and  $w'/U$ ). The frequency results are presented as a series of histograms that show the primary frequencies present in the velocity fluctuations in the three principle directions. Readings were taken at a rate of 15000Hz, or 5000Hz for each of the three velocity components. Each data set holds 4096 readings for a time interval of 0.819 seconds. Frequencies above 2500 Hz are filtered out from the readings for all fan speeds because higher frequencies correspond to turbulent eddy length scales smaller than the probes spatial resolution.

### 5.2.1 Axial (U) Velocity Measurements

The first step in determining the forces acting upon a fiber is to determine the velocities that are acting upon the fiber. Once these velocities are known, the aerodynamic forces acting upon the fiber can be determined using the relationships that were presented in the previous chapter. The four fan speeds will be 500, 1000, 1500, and 2000 RPM.

Table 5.1 presents the measured axial velocities for all fan speeds. This table presents the mean velocities for each of the positions downstream of the airfoil. The final row also presents the grand average for all of the downstream positions for each fan speed. Table 5.2 presents the calculated velocity fluctuations ( $u'$ ) for each position downstream of the airfoil. Again, the results are given for each of the four fan speeds.

Figure 5-3 presents the data shown in Tables 5.1 in graphical format. In this figure, the mean value is plotted along with lines indicating the mean plus or the mean minus one standard deviation. This figure indicates that the mean axial velocity increases as the distance from the airfoil increases for three of the four fan speeds at which measurements were taken.

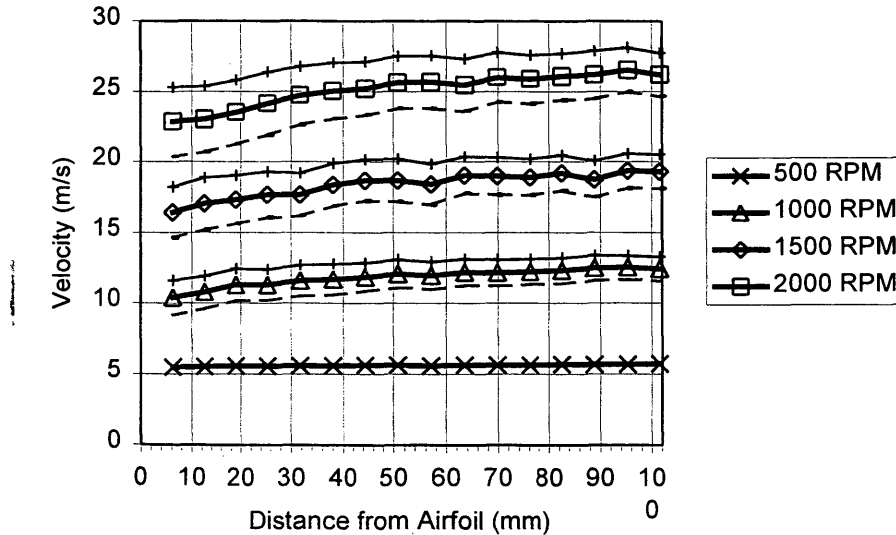


Figure 5-3

Mean axial ( $U$ ) velocities measured downstream of the airfoil.

Table 5.1

Mean axial velocity ( $U$ ) and turbulent intensity ( $u'/U$ ) at different positions downstream of the airfoil with four different fan speeds (500, 1000, 1500, & 2000 RPM).

Position (mm)	500 RPM		1000 RPM		1500 RPM		2000 RPM	
	U (m/s)	$u'/U$	U (m/s)	$u'/U$	U (m/s)	$u'/U$	U (m/s)	$u'/U$
6	5.499	2.5%	10.373	11.9%	16.415	11.0%	22.827	10.8%
13	5.538	2.6%	10.768	10.8%	17.037	10.9%	23.029	10.1%
19	5.569	2.7%	11.285	10.1%	17.325	9.8%	23.508	9.7%
25	5.572	2.6%	11.279	9.7%	17.667	9.1%	24.141	9.2%
32	5.596	2.5%	11.594	9.3%	17.668	8.5%	24.703	8.3%
38	5.593	2.5%	11.669	9.2%	18.352	8.3%	25.035	8.0%
44	5.631	2.8%	11.840	8.4%	18.696	7.9%	25.21	7.6%
51	5.624	2.5%	12.068	8.2%	18.688	8.2%	25.643	7.3%
57	5.594	2.2%	11.944	8.0%	18.402	7.8%	25.666	7.4%
64	5.641	2.4%	12.177	7.6%	19.039	6.8%	25.459	7.4%
70	5.659	2.5%	12.135	7.7%	18.996	7.0%	26.003	6.8%
76	5.660	2.5%	12.225	7.3%	18.902	6.8%	25.869	6.7%
83	5.672	2.6%	12.286	7.5%	19.190	6.6%	26.068	6.3%
89	5.664	2.6%	12.495	7.3%	18.772	7.0%	26.179	6.5%
95	5.677	2.6%	12.525	6.7%	19.374	6.3%	26.549	6.0%
102	5.712	2.8%	12.412	7.0%	19.305	6.2%	26.183	5.9%

The increase in axial velocity from the position closest to the airfoil to the farthest position was 3.9% with a fan speed of 500 RPM, 19.7% for 1000 RPM, 17.6% for 1500 RPM, and 14.7% for a fan speed of 2000 RPM. This difference in behavior suggests that the flow regime is different for the lowest fan speed.

The onset of turbulence begins when the Reynolds number ( $Re$ ) reaches a value of  $2 \cdot 10^3$ . At this value for  $Re$ , the flow enters the transition region where the flow is not

yet fully turbulent. A flow may not reach fully turbulent until it reaches much higher Reynolds numbers. For flows in square ducts, Re is calculated using the following equation:

$$\text{Re} = \frac{\rho_{Air} \cdot D \cdot U}{\mu_{Air}} \quad (5.8)$$

where  $\rho_{Air}$  is the density of air (1.08 kg/m<sup>3</sup> in Golden, Colorado), D is the diameter of duct (0.2032m), U is the axial velocity (m/s), and  $\mu_{Air}$  is the viscosity of air (1.82·10<sup>-5</sup> kg/m-s @ 20°C)

When the mean axial velocities recorded 102mm from the airfoil are used in equation 5.8, the value of Re for each of the fan speeds are as shown in Table 5.2. The fact that the fan speed of 500 RPM exhibits different behavior than the other fan speeds suggests that the flow is still in the transition region between fully laminar and fully turbulent flow.

Table 5.2

Reynolds numbers for each fan speed.

Fan Speed	Re
500 RPM	6.9·10 <sup>4</sup>
1000 RPM	1.50·10 <sup>5</sup>
1500 RPM	2.33·10 <sup>5</sup>
2000 RPM	3.16·10 <sup>5</sup>

### 5.2.2 Vertical (W) Velocity Measurements

The second component of the velocity field within the wind tunnel is the vertical (W) component of velocity. Along with the axial velocity, this is the most important velocity in this analysis. Table 5.3 presents the mean vertical (W) velocity and the velocity fluctuation ( $w'$ ) for the different positions downstream of the airfoil. Figure 5-4 presents the same data in a graphical form.

Table 5.3

Mean vertical velocity ( $W$ ) and turbulent intensity ( $w'/U$ ) at different positions downstream of the airfoil with four different fan speeds (500, 1000, 1500, & 2000 RPM).

Position (mm)	500 RPM		1000 RPM		1500 RPM		2000 RPM	
	W (m/s)	$w'/U$	W (m/s)	$w'/U$	W (m/s)	$w'/U$	W (m/s)	$w'/U$
6	0.161	2.8%	0.321	11.4%	0.612	10.1%	0.701	9.7%
13	0.161	2.9%	0.301	10.8%	0.454	9.6%	0.701	9.2%
19	0.175	2.6%	0.261	9.8%	0.363	8.8%	0.542	8.5%
25	0.162	2.8%	0.258	9.5%	0.321	8.3%	0.447	8.1%
32	0.169	2.8%	0.274	8.7%	0.279	8.3%	0.522	7.5%
38	0.174	2.5%	0.271	8.2%	0.332	7.4%	0.499	7.2%
44	0.161	2.7%	0.212	8.0%	0.347	7.2%	0.493	6.9%
51	0.169	2.7%	0.229	7.4%	0.316	6.8%	0.462	6.5%
57	0.135	2.3%	0.234	7.5%	0.165	7.0%	0.423	6.5%
64	0.158	2.7%	0.148	7.1%	0.272	6.4%	0.551	6.4%
70	0.155	2.8%	0.189	6.9%	0.264	6.4%	0.456	5.9%
76	0.160	2.8%	0.142	6.5%	0.273	6.2%	0.487	5.9%
83	0.145	3.1%	0.178	6.4%	0.295	5.8%	0.393	5.6%
89	0.150	2.7%	0.220	6.5%	0.260	6.2%	0.462	5.5%
95	0.142	3.1%	0.168	6.1%	0.297	5.5%	0.546	5.3%
102	0.170	3.0%	0.178	5.9%	0.304	5.6%	0.475	5.3%

The data indicates that the mean vertical velocity decreases as the distance from the airfoil increases. This decrease is not a large decrease and the pattern is not very regular. Overall, there was a slight positive vertical velocity at all positions. This velocity increased as the fan speed increased. The fluctuations were one and a half times the mean velocity for the fan speed of 500 RPM. For the remaining fan speeds, the fluctuations were about four times the mean vertical velocity. Again, this suggests that the flow with the lowest fan speed was not yet fully turbulent.

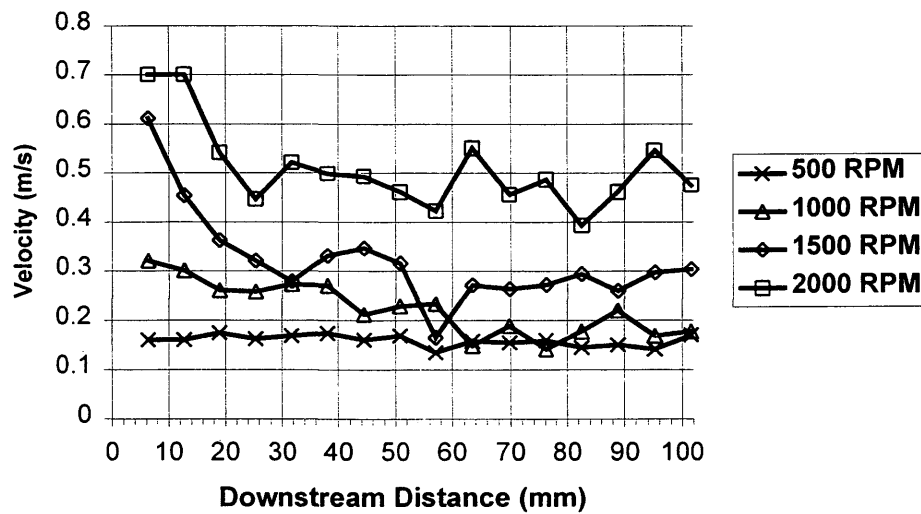


Figure 5-4

Mean Vertical ( $\bar{W}$ ) velocities for different downstream positions.

### 5.2.3 Horizontal (V) Velocity Measurements

The third component of velocity in the wind tunnel is the horizontal velocity. This velocity will not be dealt with in the modeling of the fiber. Table 5.4 presents the mean horizontal velocity (V) and velocity fluctuations ( $v'$ ) for different distances from the airfoil. Figure 5-5 presents the same data in a graphical format.

Table 5.4

Mean horizontal velocity (V) and turbulent intensity ( $v'/U$ ) at different positions downstream of the airfoil with four different fan speeds (500, 1000, 1500, & 2000 RPM).

Position (mm)	500 RPM		1000 RPM		1500 RPM		2000 RPM	
	V (m/s)	$v'/U$	V (m/s)	$v'/U$	V (m/s)	$v'/U$	V (m/s)	$v'/U$
6	-0.199	3.9%	-1.429	14.5%	-2.301	13.6%	-3.369	13.8%
13	-0.205	4.3%	-1.410	13.0%	-2.29	12.6%	-3.366	12.7%
19	-0.207	4.2%	-1.520	12.3%	-2.35	11.7%	-2.990	12.3%
25	-0.224	4.0%	-1.409	11.7%	-2.108	10.6%	-3.394	11.0%
32	-0.220	4.0%	-1.153	10.7%	-2.355	10.0%	-2.999	10.2%
38	-0.205	4.1%	-1.344	10.1%	-2.158	9.7%	-3.137	9.9%
44	-0.197	4.1%	-1.393	9.7%	-2.088	9.0%	-3.128	9.4%
51	-0.215	4.0%	-1.301	9.0%	-2.156	8.5%	-2.917	9.1%
57	-0.190	3.4%	-1.368	8.9%	-2.114	8.6%	-2.910	8.9%
64	-0.213	4.4%	-1.433	8.5%	-2.035	8.1%	-3.015	8.2%
70	-0.225	4.3%	-1.234	8.1%	-2.004	7.7%	-3.093	8.1%
76	-0.218	4.0%	-1.292	8.0%	-1.827	7.7%	-2.770	8.0%
83	-0.251	4.4%	-1.240	7.5%	-1.842	7.2%	-2.670	7.8%
89	-0.225	3.9%	-1.327	7.5%	-1.759	7.4%	-2.809	7.6%
95	-0.251	4.1%	-1.255	7.3%	-1.945	7.1%	-2.849	7.3%
102	-0.255	4.4%	-1.029	7.0%	-2.157	6.8%	-2.771	7.2%

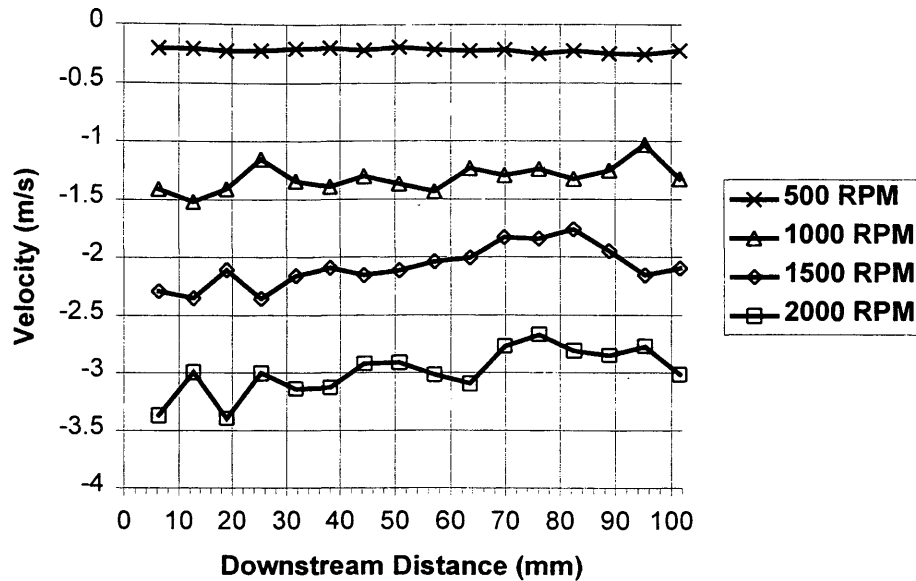


Figure 5-5

Mean Horizontal (V) velocities for different downstream positions.

The most interesting thing about this data is that there is a significant negative mean velocity for all fan speeds. This mean velocity appears to be independent upon distance from the airfoil. In addition, the fluctuations do not appear to vary with the fan speed. All four fan speeds show a horizontal fluctuation of about 70% of the mean horizontal velocity.

#### 5.2.4 Turbulent Intensities

The turbulent intensity gives an indication of the magnitude of the fluctuations present within a velocity field. For this analysis, the intensities will be referenced to the

axial velocity recorded 102mm from the trailing edge of the airfoil to which the fiber will be mounted. Figures 5-6, 5-7, and 5-8 present the calculated values for the turbulence intensities.

The most striking feature of all three figures is the fact that the behavior of the lowest fan speed exhibits completely different behavior than the other three fan speeds. In previous sections different behavior was noted for this lowest fan speed as well. These figures support the conclusion that the flow with the lowest fan speed is not fully turbulent. As a result of this difference in behavior, a fan speed of 500 RPM will not be used in the following analysis.

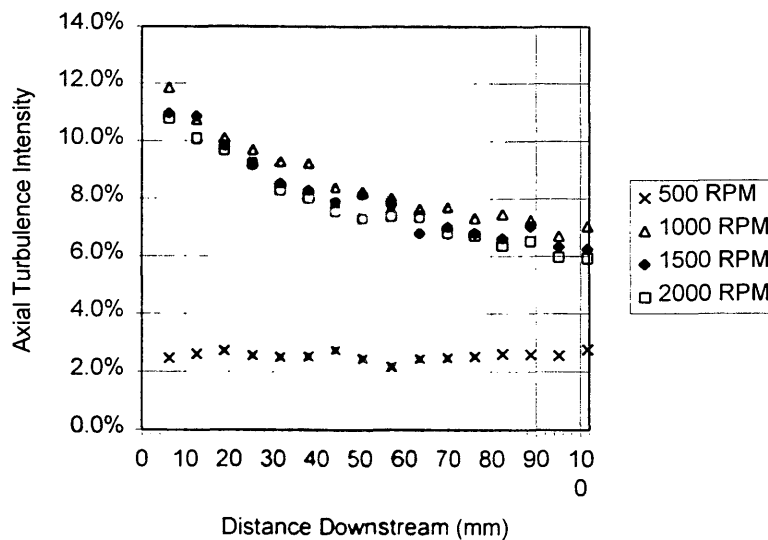


Figure 5-6

Axial turbulent intensity for four different fan speeds.

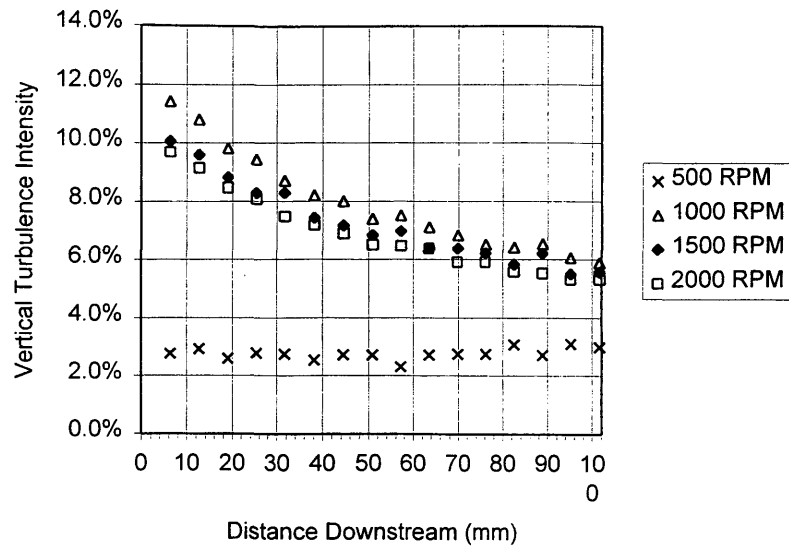


Figure 5-7

Vertical turbulent intensity for four different fan speeds.

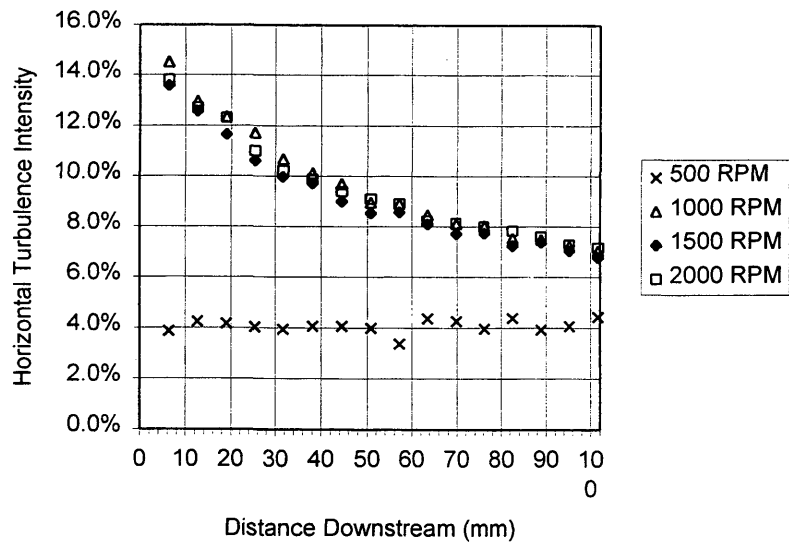


Figure 5-8

Horizontal turbulent intensity for four different fan speeds.

The behaviors of the three higher fan speeds are very similar. In all cases, the intensity is about 0.10-0.14 at a distance of 6mm from the airfoil and decreases to a value of about 0.06-0.07 at a distance of 102mm from the airfoil. The shape of the curve suggests that the intensity values asymptotically approach a value of around 0.06. The fact that the intensity in all directions is about the same confirms that the turbulence is isotropic.

It is interesting to note that the horizontal intensities are slightly higher than the intensities in the vertical direction. This difference may be the result of the airfoil being present in the wind tunnel. The air is squeezed in the vertical direction as it passes over the airfoil. Even with the presence of the airfoil, the difference in the component turbulence intensities is not significant enough to invalidate the assumption of isotropic turbulence.

#### 5.2.5 Frequency Spectrum

It is necessary to know the frequency spectrum of a turbulent velocity field in addition to knowing the mean velocity and turbulent intensities. It is necessary to know the frequency of the turbulence since it is possible for the motion of an object to be magnified if it is forced with a frequency near its natural frequency. The ratio of dynamic amplitude to static amplitude ( $X/\delta_k$ ), known as the amplitude ratio ( $M$ ), is plotted as a

function of frequency ratio ( $r$ ) in Figure 5-9 (Steidel, 1971). The frequency ratio is defined as:

$$r = \frac{\omega}{\omega_n} \quad (5.10)$$

where  $\omega$  is the frequency of applied force and  $\omega_n$  is the natural frequency for the system.

Figure 5-9 shows how the amplitude of vibrations increases dramatically when the frequency ratio approaches a value of one. On the other hand, once the frequency ratio reaches values greater than five, the amplification is almost zero. If the frequency spectrum of the turbulence is near the natural frequency of the fiber, resonance will occur and the amplitude of fiber motion will increase.

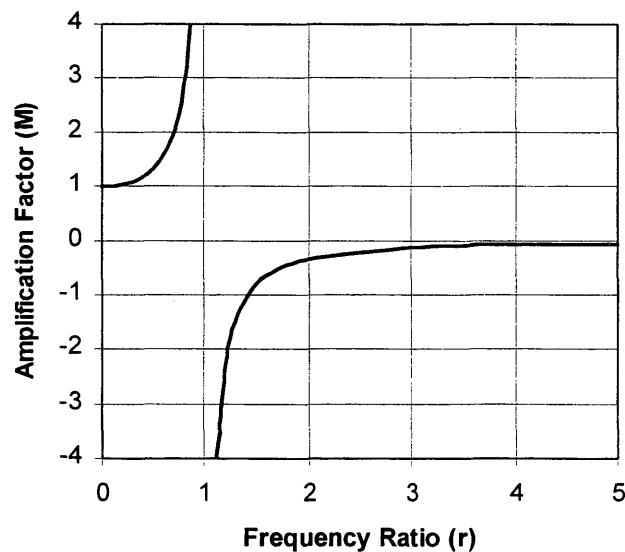


Figure 5-9

Amplification ratio plotted as a function of frequency ratio.

The frequency spectrum is determined by performing a Fast Fourier Transform (FFT) of the velocity data. For this study, a FFT was performed on each of the individual data sets taken at the different downstream positions. The resulting frequency spectrums for the axial and the vertical velocity components are shown in the following graphs. Since the horizontal velocity component is not going to be part of this fiber motion study, the frequency spectrum for the V-velocity component will not be presented here.

Figures 5-10, 5-11 and 5-12 present the frequency spectrum for the axial (U) velocity measurements for fan speeds of 1000 RPM, 1500 RPM, and 2000 RPM. Figures 5-13, 5-14 and 5-15 present the frequency spectrums for the vertical (W) velocity measurements.

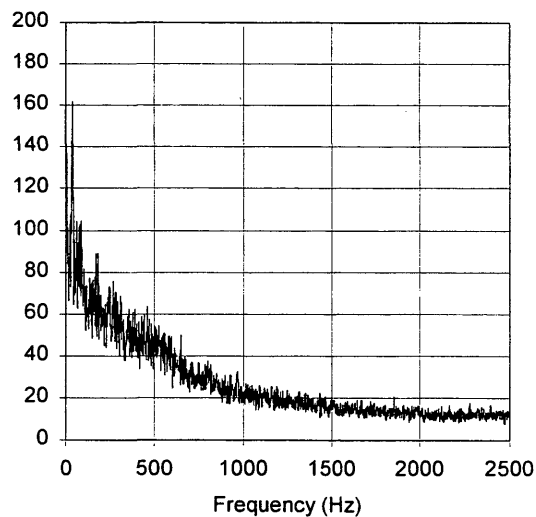


Figure 5-10

Axial velocity frequency spectrum for 1000 RPM.

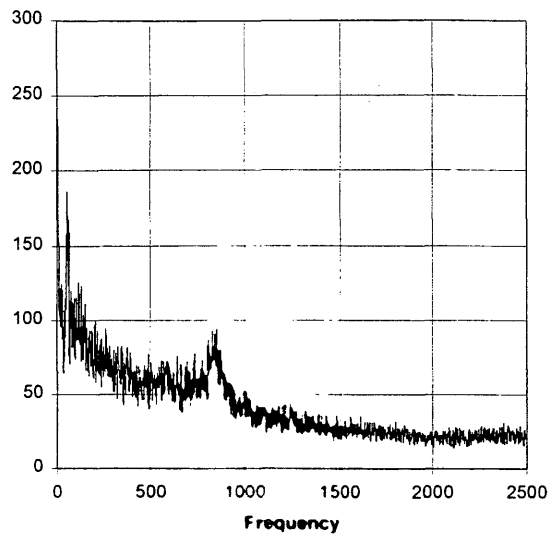


Figure 5-11

Axial velocity frequency spectrum for 1500 RPM.

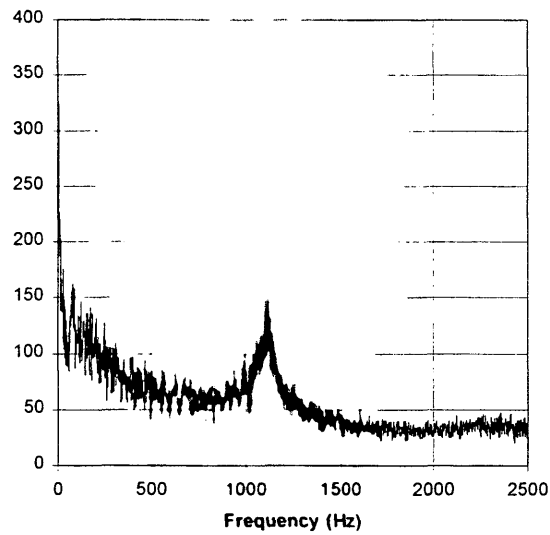


Figure 5-12

Axial velocity frequency spectrum for 2000 RPM.

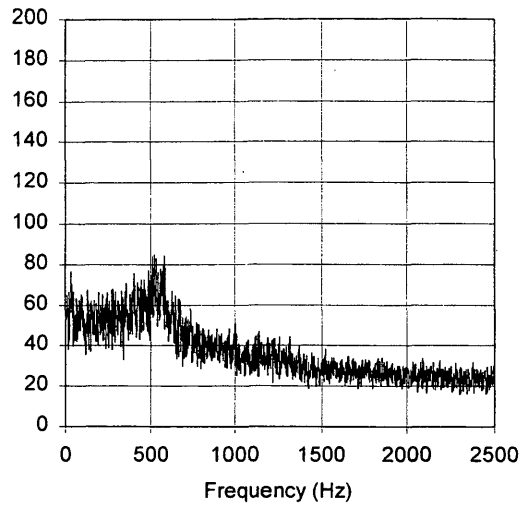


Figure 5-13

Vertical velocity frequency spectrum for 1000 RPM.

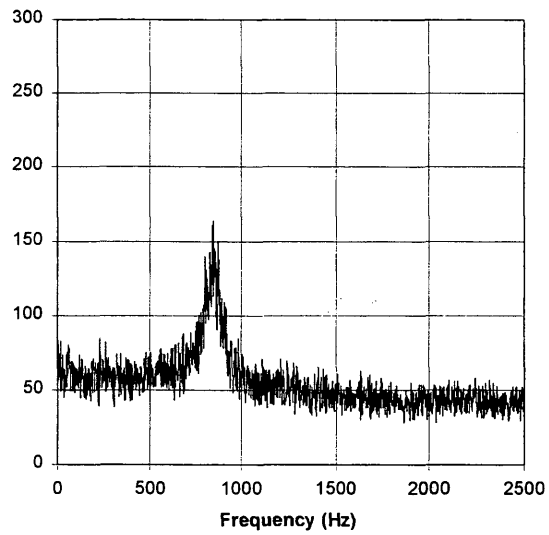


Figure 5-14

Vertical velocity frequency spectrum for 1500 RPM.

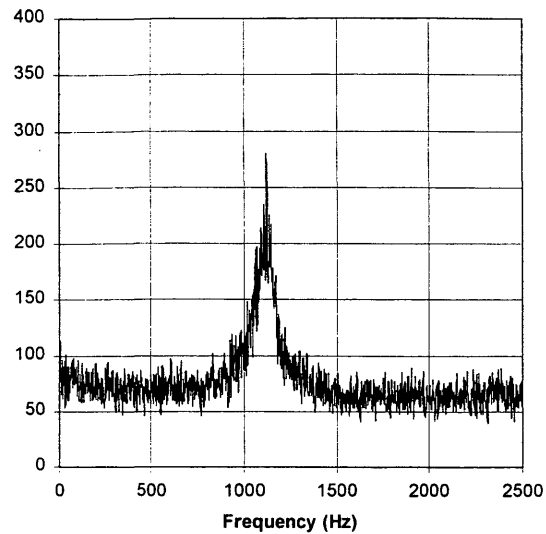


Figure 5-15

Vertical velocity frequency spectrum for 2000 RPM.

Figures 5-10 through 5-12 indicate that there is a significant amount of vibrational energies in frequencies below 500 Hz in the axial direction. In addition, a peak frequency of 800 Hz appears in the frequency spectrum for the fan speed of 1500 RPM and a peak frequency of 1100 Hz appears in the frequency spectrum for the fan speed of 2000 RPM. There may be the beginning of a 500 Hz frequency in the 1000 RPM spectrum, but the peak, if there, is lost in the plot of the individual frequencies.

Figures 5-13 through 5-15 indicate that there is a predominant frequency that increases as the fan speed (axial velocity) increases. This frequency peak starts to appear with a fan speed of 1000 RPM at a frequency of 500 Hz. This main frequency increases

to about 800 HZ with a fan speed of 1500 RPM and approximately 1100 Hz with a fan speed of 2000 RPM. This progression indicates that the peak frequency increases linearly with the axial velocity. These figures indicate that the amplification factor will be approximately zero if the frequency ratio greater than 4 or less than  $\frac{1}{4}$ .

### 5.3 Discussion of Results

The most striking aspect of these results is the difference between the 500 RPM results and the rest of the fan speeds. With a fan speed of 500 RPM, the turbulence intensities are independent of the distance from the airfoil. However, the intensity is clearly dependent on the distance from the airfoil for the higher fan speeds. This suggests that the flow with at the lowest fan speed it not yet fully turbulent. Because of this, the 500 RPM fan setting will not be used in the analysis of the fiber.

Figure 5-14 indicates that there is a peak frequency of around 500 Hz present in the turbulence with a fan speed of 1000 RPM. In addition, this main frequency increases linearly (approximately) with the axial velocity and reaches a value of approximately 800 HZ with a fan speed of 1500 Hz and approximately 1100 HZ with a fan speed of 2000 RPM. If the natural frequencies of any fibers tested in the wind tunnel are one-fourth or less than these major frequencies, then amplification factor will be approximately zero and any effects of resonance can be ignored.

## Chapter 6

## HIGH-SPEED VIDEO RESULTS

6.1 Frequency Results

The frequency results of the videotape analysis are presented in Tables 6.1, 6.2, and 6.3. These tables present the average and the standard deviation for each of the three test fibers and the three fan speeds.

Table 6.1

Frequency results for 12 $\mu$ m fiber.

<b>Fan Speed</b>	<b>Frequency (Hz)</b>	$\sigma$
1000	17	0.5
1500	15	0.5
2000	18	0.7

Table 6.2

Frequency results for 30 $\mu$ m fiber.

<b>Fan Speed</b>	<b>Frequency (Hz)</b>	$\sigma$
1000	14	1.0
1500	19	0.8
2000	27	1.0

Table 6.3

Frequency results for 47 $\mu$ m fiber.

<b>Fan Speed</b>	<b>Frequency (Hz)</b>	<b><math>\sigma</math></b>
1000	13	1.0
1500	14	0.8
2000	17	1.2

When watching the motion of the fiber on the videotape, it becomes apparent that the fibers have two types of motion. The first corresponds with the lowest frequency while the second corresponds to the higher frequencies that were ignored for this analysis. The higher frequencies were ignored for this analysis due to the need to manually analyze the videotape data. If a method to digitally analyze the videotape were available, it would then be possible to determine higher frequencies.

The first type of motion typically corresponded with the maximum displacement and the lowest frequency. When this behavior occurred the fiber was nearly straight or the first half of the fiber had a recognizable slope and then the second half became almost parallel to the axial flow. This first type of motion is shown in Figure 6-1.

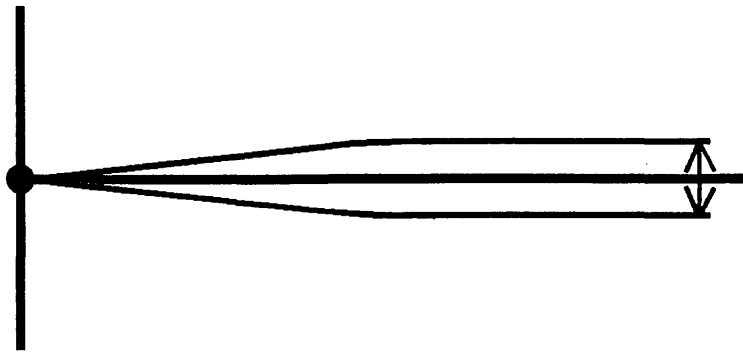


Figure 6-1

Low frequency fiber motion.

The second type of fiber motion, shown in Figure 6-2, generally fell between the displacements of the first mode and consisted of small amplitude rapid fluctuations. During some periods of the recordings, the fibers appeared to be stationary, except for a noticeable “shaking.” This shaking, when viewed at a slow tape speed, proved to be many, small amplitude waves traveling along the length of the fiber.

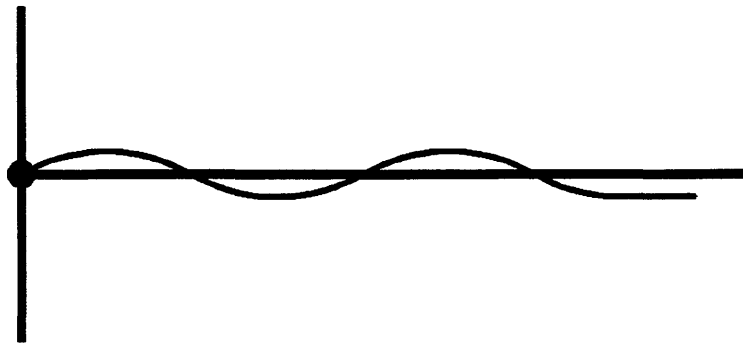


Figure 6-2

High frequency fiber motion.

## 6.2 Measured Displacements

In order to facilitate the measurement of displacements, a reticle was positioned on the video screen for the two larger fibers. The reticle was not used with smallest fiber because it obscured the fiber. The horizontal and vertical lines of the reticle were aligned with the root of the fiber. The displacements of the tip were measured relative to the horizontal line of the reticle. A measurement of 0 indicates that the fiber was aligned with the reticle. A positive number means that the tip of the fiber was above the reticle and a negative number means that the tip of the fiber was below the reticle.

The displacements measured during the videotape analysis are presented in Tables 6.4, 6.5, and 6.6. These tables present the maximum displacements (both positive and negative) and the mean position measured for each fiber.

Table 6.4

Maximum measured displacements for 12 $\mu$ m fiber (mm).

<b>Fan Speed</b>	<b>Positive (mm)</b>	<b>Mean (mm)</b>	<b>Negative (mm)</b>
1000	+4	$\approx 0$	-3
1500	+5	$\approx 0$	-4
2000	+5	$\approx 0$	-4

Table 6.5

Maximum measured displacements for 30 $\mu$ m fiber (mm).

<b>Fan Speed</b>	<b>Positive (mm)</b>	<b>Mean (mm)</b>	<b>Negative (mm)</b>
1000	+6	+1	-4
1500	+7	+2	-5
2000	+8	+2	-5

Table 6.6

Maximum measured displacements for 47 $\mu$ m fiber (mm).

<b>Fan Speed</b>	<b>Positive (mm)</b>	<b>Mean (mm)</b>	<b>Negative (mm)</b>
1000	0	-4	-8
1500	+2	-2	-5
2000	+2	-1	-5

When watching the videotape, it was readily apparent that the largest fiber (47 $\mu$ m) had a slightly bent shape. The drag created by the axial velocity was not large enough to straighten the fiber out, so the equilibrium position for this fiber was below the horizontal line of the reticle. It is also possible that the weight of the fiber was significant. The angle of the fiber was still less than about 0.2 radians, so the small angle approximation for the axial force should still apply. As a result, it should be possible to compare the fluctuations of the largest fiber around its equilibrium position to the results obtained by the numerical simulations.

## Chapter 7

### NUMERICAL RESULTS

#### 7.1 Descriptions of Numerical Simulations

The results for three different types of numerical simulations are presented in this chapter. The first simulation will investigate the response of the fiber model to an initial displacement with no vertical forces to determine the damping created by the axial velocity. In addition, this model will examine the effects of axial turbulence upon the movement of the fiber. The second situation is a single degree of freedom model with turbulence in the axial and vertical directions. The third simulation is the two-degree of freedom model with turbulence in the axial and vertical directions.

#### 7.2 The Effect of Axial Turbulence on Fiber Motion

The first question investigated is how turbulence in the axial direction affects the motion of the fiber. This investigation will be accomplished by subjecting a fiber model to an initial displacement and then recording the motion as the fiber is released. The only force that will be acting upon the fiber will be created by the axial velocity. The first simulation will assume a constant axial velocity. The second simulation will use turbulence data recorded in the wind tunnel as the velocity field.

If a fiber were to be immersed in a fully developed laminar flow, the only force acting on the fiber would be created by the axial velocity. This situation will also provide the damping effects of the axial velocity upon the fiber. This would be difficult to accomplish in an actual air stream. Because of this, numerical simulation is an attractive approach. A two degree of freedom model will be used for this simulation.

For this simulation, the motion of three fibers with a diameters of 12  $\mu\text{m}$ , 30  $\mu\text{m}$ , and 47  $\mu\text{m}$  will be studied. The fiber will be given an initial displacement and then be released. The resulting motion of the fiber will be analyzed to determine the damping provided by the axial velocity. The damping provided at each different fan speed will be calculated for each fiber.

The damping factor can be determined by measuring the value of successive peaks and then using the following two equations:

$$\delta = \frac{1}{m} \cdot \ln\left(\frac{x_1}{x_{m+1}}\right) \quad (7.1)$$

$$\zeta = \frac{\delta}{2 \cdot \pi} \quad (7.2)$$

where  $m$  is the local peak number,  $\delta$  is the logarithmic decrement,  $x_1$  is the amplitude of the first peak, and  $\zeta$  is the damping factor. Tables 7.1 and 7.2 give the peak values and the damping factor calculated using equations 7.1 and 7.2 for the first five peaks at the tip of the fiber with a constant axial velocity. Tables 7.3 and 7.4 give the peak amplitudes and the calculated damping factors with axial turbulence present in the air stream.

Table 7.1

First five local peaks at tip of 12  $\mu\text{m}$  fiber and resulting damping factor (without axial turbulence, 1000 RPM).

<b>Peak</b>	<b>Displacement at Tip of Fiber (mm)</b>	$\delta$	$\zeta$
1	.0014	-NA-	-NA-
2	.0006	.847	.135
3	.0005	.567	.090
4	.0003	.513	.082
5	.0002	.486	.077

Table 7.2

First five local peaks a tip of fiber 30  $\mu\text{m}$  and resulting damping factor (without axial turbulence, 1000 RPM).

<b>Peak</b>	<b>Displacement at Tip of Fiber (mm)</b>	$\delta$	$\zeta$
1	.0023	-NA-	-NA-
2	.0018	.245	.039
3	.0015	.214	.034
4	.0012	.217	.035
5	.0010	.277	.044

Table 7.3

First five local peaks at tip of 12  $\mu\text{m}$  fiber and resulting damping factor (with axial turbulence, 1000 RPM).

Peak	Displacement at Tip of Fiber (mm)	$\delta$	$\zeta$
1	$5.0 \cdot 10^{-4}$	-NA-	-NA-
2	$2.5 \cdot 10^{-4}$	.693	.110
3	$1.7 \cdot 10^{-4}$	.539	.086
4	$1.3 \cdot 10^{-4}$	.449	.071
5	$0.8 \cdot 10^{-4}$	.458	.073

Table 7.4

First five local peaks at tip of 30  $\mu\text{m}$  fiber and resulting damping factor (with axial turbulence, 1000 RPM).

Peak	Displacement at Tip of Fiber (mm)	$\delta$	$\zeta$
1	$2.3 \cdot 10^{-3}$	-NA-	-NA-
2	$1.8 \cdot 10^{-3}$	.245	.039
3	$1.5 \cdot 10^{-4}$	.214	.034
4	$1.3 \cdot 10^{-4}$	.190	.030
5	$1.0 \cdot 10^{-4}$	.208	.033

The results shown in Tables 7.1 through 7.4 indicate that the inclusion of axial turbulence has a small effect on the damping ratio. The damping factor calculated using

five peaks provides the best estimate for the actual damping factor. With a constant axial velocity, the damping ratio is 0.077 for the 12  $\mu\text{m}$  fiber and .044 for the 30  $\mu\text{m}$  fiber.

With axial turbulence, the average damping ratio is .073 for the 12  $\mu\text{m}$  fiber and .033 for the 30  $\mu\text{m}$  fiber. The differences between the two cases are very small and can be ignored.

The results shown in Chapter 5 indicate that turbulent intensities present in the axial velocity are on the order of 6-8%. These results would indicate that if the turbulent intensities present in a velocity field are on the order of 10%, then the axial intensity can be ignored when attempting to model the motion of a fiber. This fact reduces the need for detailed turbulence measurements in the axial direction and as a result, simplifies the model required to satisfactorily model the motion of a fiber.

The average calculated damping ratios for the three test are shown in Table 7.5. These damping ratios are the average damping ratio for the first five local peaks and were determined using a constant axial velocity. The damping ratio of the 47  $\mu\text{m}$  fiber is not shown because it was approximately zero.

Table 7.5

Average damping ratio for 12  $\mu\text{m}$  and 30  $\mu\text{m}$  fibers.

<b>Fan Speed</b>	<b>12 <math>\mu\text{m}</math></b>	<b>30 <math>\mu\text{m}</math></b>
1000	.096	.038
1500	.111	.023
2000	.101	.014

The results in Table 7.5 indicate that the damping ratio decreases as the diameter of the fiber increases. This also means that the damping ratio decreases as the mass of the fiber increases. As the mass of the fiber increases, the momentum of the fiber increases as well. These results indicate that the damping effect produced by the axial velocity becomes insignificant as the mass of the fiber increases above a certain level. All real systems exhibit some damping, so this result is not realistic and must be rejected. Since the damping of the 47  $\mu\text{m}$  fiber is negligible, it can be concluded that the kinematic model does not satisfactorily model the motion of this fiber. In the current model, the hinge connections are assumed to provide no resistance to bending. Changing the hinges in the model so that they provide a resistance to bending would reduce this shortcoming in the kinematic model.

### 7.3 Numerical Results: Displacement of Test Fibers

There are two major factors that should be compared between the video data and the numerical simulations. The first of these factors is the maximum displacement of the fiber. Tables 7.6a, 7.6b, and 7.6c presents both the numerical results and the video results for the 12  $\mu\text{m}$  fiber. Table 7.7a, 7.7b, and 7.7c present the results for the 30  $\mu\text{m}$  fiber.

Table 7.6a

Maximum positive 12  $\mu\text{m}$  fiber displacement (mm).

<b>Fan Speed</b>	<b>Video</b>	<b>1 DOF</b>	<b>2 DOF</b>
1000	+4	+5.6	+6.1
1500	+5	+8.7	+5.5
2000	+5	+6.2	+6.7

Table 7.6b

Approximate mean 12  $\mu\text{m}$  fiber position (mm).

<b>Fan Speed</b>	<b>Video</b>	<b>1 DOF</b>	<b>2 DOF</b>
1000	$\approx 0$	+1.8	+1.6
1500	$\approx 0$	+1.6	+1.5
2000	$\approx 0$	+1.7	+1.8

Table 7.6c

Maximum negative 12  $\mu\text{m}$  fiber displacement (mm).

<b>Fan Speed</b>	<b>Video</b>	<b>1 DOF</b>	<b>2 DOF</b>
1000	-3	-4.9	-2.9
1500	-4	-2.8	-2.6
2000	-4	-3.1	-2.1

Table 7.7a

Maximum positive 30  $\mu\text{m}$  fiber displacement (mm).

<b>Fan Speed</b>	<b>Video</b>	<b>1 DOF</b>	<b>2 DOF</b>
1000	+6	+5.2	+6.7
1500	+7	+7.2	+6.2
2000	+8	+6.3	+9.0

Table 7.7b

Approximate mean 30  $\mu\text{m}$  fiber position (mm).

<b>Fan Speed</b>	<b>Video</b>	<b>1 DOF</b>	<b>2 DOF</b>
1000	$\approx +1$	+1.7	+1.6
1500	$\approx +2$	+1.4	+1.5
2000	$\approx +2$	+1.4	+1.8

Table 7.7c

Maximum negative 30  $\mu\text{m}$  fiber displacement (mm).

<b>Fan Speed</b>	<b>Video</b>	<b>1 DOF</b>	<b>2 DOF</b>
1000	-4	-1.0	-4.1
1500	-5	-4.0	-2.8
2000	-5	-2.3	-2.3

While the uncertainty of the video data is relatively large due to the small fiber size, it appears that the kinematic models agree reasonably well with the actual fiber. The maximum positive displacement for the 12  $\mu\text{m}$  fiber is about +5 mm in the video data while the numerical simulations results in tip displacements that average +6-7 mm. The maximum positive displacement for the 30  $\mu\text{m}$  fiber is +6-8 mm in the video data and averages about about +7 mm for the numerical simulations.

The mean position of the fiber has the largest uncertainty from the video data. When the reticle was on, it obscured the 12  $\mu\text{m}$  fiber. As a result, it was turned off during

the videotaping. This makes it difficult to determine a mean position for the fiber.

Because of this, the mean position was stated to be approximately zero. The numerical simulations indicate that the mean position is approximately +1.6 mm. This position is similar to the results for the other fiber. Since the mean vertical velocity is not zero, it is reasonable that the mean position for the fiber would be a positive displacement.

The mean position for the 30  $\mu\text{m}$  fiber in the video data agrees quite well with the results from the numerical simulations. The video data indicates a mean position of +1-+2 mm and the numerical simulations result in a mean position of +1.5 mm.

The videotape data presented in Table 7.6c indicates that the maximum negative displacement for the fiber was approximately -4 mm while the numerical models indicate a displacement of between -2.1 and -2.9 mm. The maximum negative position for the 30  $\mu\text{m}$  fiber was -4 to -5 mm in the video data and was -1 to -4 mm in the numerical studies.

Perhaps the best indication of agreement is to compare the range of the displacements. The videotaped data indicates that the 12  $\mu\text{m}$  fiber has a peak-to-peak amplitude of 7 mm for the 1000 RPM fan speed, and 9 mm for the 1500 and 2000 RPM fan speeds. The single degree of freedom model predicts an amplitude of 10.5 mm for 1000 RPM, 11.5 mm for 1500 RPM, and 9.3 mm for 2000 RPM. The two degrees of freedom model predicts an amplitude of 9 mm for 1000 RPM, 8.1 mm for 1500 RPM, and 8.8 mm for 2000 RPM.

The videotaped data indicates that the 30  $\mu\text{m}$  fiber has a peak-to-peak amplitude of 10 mm for the 1000 RPM fan speed, and 12 mm for the 1500 RPM fan speed and 13 mm for the 2000 RPM fan speed. The single degree of freedom model predicts an amplitude of 6.2 mm for 1000 RPM, 11.2 mm for 1500 RPM, and 8.6mm for 2000 RPM. The two degrees of freedom model predicts an amplitude of 10.8mm for 1000 RPM, 9 mm for 1500 RPM, and 11.3 mm for 2000 RPM.

The kinematic models predicts the motion of the fiber reasonably well. The two degrees of freedom model is closer to the video results than the single degree of freedom model. This suggests that the use of models with more elements would provide a more realistic model for the fiber motion. Analyzing the frequency of the fiber motion will provide a better idea if the kinematic models may be used. If the frequency spectrum for the kinematic models agrees with the frequency data from the videotape, then the models can be considered to be an acceptable way to model the fiber.

#### 7.4 Numerical Results: Frequency Spectrums of Test Fibers

The frequency of the fiber's motion is the second criteria that should be used to judge the kinematic models. The frequency spectrum for each fan speed was determined by performing an FFT on the position versus time data. The results from these transformations for the single degree of freedom model are shown in Appendix C. Table 7.8 summarizes the frequency data for the 12  $\mu\text{m}$  fiber and Table 7.9 summarizes the

frequency data for the 30  $\mu\text{m}$  fiber. Table entries that include two numbers indicate two small local peaks that were the same magnitude.

Table 7.8

Frequency data (Hz) for 12  $\mu\text{m}$  fiber.

Fan Speed	Video Data	1DOF	2 DOF
1000	17	10/20	20
1500	15	10/20	5/30
2000	18	23	20

Table 7.9

Frequency data (Hz) for 30  $\mu\text{m}$  fiber.

Fan Speed	Video Data	1DOF	2 DOF
1000	14	5/10	23
1500	19	18	25
2000	27	24	25

The frequencies obtained from the FFT agree reasonably well with the frequencies obtained from the videotaped data. The frequencies from the two-degrees of freedom model were more varied than those obtained from the single degree of freedom model. For example, the two-degree of freedom models of the 30  $\mu\text{m}$  fiber had a large peak frequency at about 90 Hz for the 1500 RPM fan speed.

The fact that the frequencies are seen on the videotaped data and in the frequency spectrums of the numerical models suggest that the kinematic modeling approach is a

realistic method to take when modeling small fibers. It also suggests that the aerodynamic force relationships provide reasonably accurate force estimates for the 12  $\mu\text{m}$  and 30  $\mu\text{m}$  diameter fibers. Since the numerical simulations of the 47  $\mu\text{m}$  fiber results in no damping, it can be concluded that the kinematic model misses some factor that becomes more important as the diameter of the fiber grows past 30  $\mu\text{m}$ . Perhaps the section properties of the fiber become significant and then provide damping which is not included in the kinematic model.

The kinematic model can be altered to include some material damping by changing the hinges in the model to provide a resistance to bending. This modification could be enacted quite easily and would result in additional damping.

#### 7.5 Numerical Results: Tensile Forces in Test Fibers

One of the unknown factors in the rotary spinning manufacturing process is the fracture mechanism. The fibers continue to grow until they reach some critical length and then break away. Is the fracture a result of the tension in the fiber growing until the fiber fails? Or is the fracture the result of fatigue? Hristov (1995) indicates that the rate at which loads are applied to a polymer affect the deformation of a polymer. Caddell (1980) indicates that polymers undergo viscoelastic behavior which is dependent upon time.

While it is not possible to determine the exact fracture mechanism from tests in the wind tunnel, it is possible to determine some relative levels of stress in the fiber due

to the axial force and axial fluctuations and the bending stresses caused by the transverse fluctuations.

The numerical simulations provide the tension in the fiber due to the axial force and the axial turbulent fluctuations. The tensile stress resulting from this fiber tension can easily be found:

$$\sigma_{Tensile} = \frac{F_{Tensile}}{\pi \cdot r_{Fiber}^2} \quad (7.3)$$

where  $\sigma_{Tensile}$  is the stress due to fiber tension,  $F_{Tensile}$  is the fiber tension, and  $r_{Fiber}$  is the radius of fiber. This stress fluctuates due to the turbulence in the air stream. The tension calculated in each test fiber for each different fan speed are plotted in Appendix D. These figures show that the fluctuations in axial force are approximately the same magnitude as the turbulent intensity in the axial direction.

However, this is not the only stress acting on the fiber. When the fiber bends, it experiences a bending stress. This bending stress is a function of the modulus of elasticity, the size of the fiber, and the radius of curvature for the bend:

$$\sigma_{Bending} = \frac{E \cdot r_{fiber}}{R} \quad (7.4)$$

where  $\sigma_{Bending}$  is the stress due to bending,  $E$  is the Modulus of Elasticity,  $r_{Fiber}$  is the radius of fiber, and  $R$  is the radius of curvature for the fiber. The maximum displacement for the two test fibers was approximately 9 mm for a fiber with a length of 102 mm. The radius of curvature for these two fibers with a displacement of 10 mm is approximately 1

m. The resulting bending stress in the 12 mm fiber is approximately  $1.8 \times 10^3$  Pa. Meanwhile, the tensile stress in the fiber ranges from  $2.65 \times 10^4$  to  $8.4 \times 10^5$  Pa. This indicates that the bending stress is approximately 1% of the tensile stress. This suggests that the tensile force and the fluctuations in the tensile force due to the turbulence play a more important role in the fracture of the fibers than the stresses caused by the bending of the fibers.

The relative strengths of the tensile force and bending forces on individual fibers in the manufacturing process can be approximated by determining the mean velocity field in the manufacturing process and then determining the mean axial force on an individual fiber. Determining the turbulent intensity along the axis of the fiber can approximate the fluctuating portion of the tensile force. At the same time, the radius of the basket can be used to approximate the radius of curvature for an individual fiber.

### 7.6 Summary of Numerical Results

The kinematic approach to modeling a single fiber does a reasonable job of modeling the motion of the 12  $\mu\text{m}$  and 30  $\mu\text{m}$  fiber. The model does not do a good job of modeling the 47  $\mu\text{m}$  fiber. This appears to be the result of the increased moment of inertia of the larger fiber. As the diameter gets larger, the section properties become more important. The kinematic model could be modified to include some addition resistance to bending by assuming that the hinged connection between elements provides a resisting moment to bending.

The results also indicate that the axial turbulence has a small effect upon the motion of the fiber. If it can be shown that the turbulent intensity in the actual manufacturing process is on the order of 10%, the mean velocity field could be used to model the motion of the fiber. This velocity field could readily be generated by a CFD analysis.

The frequencies of motion that result from the use of the kinematic model agree reasonably well with the frequencies seen on the high-speed videotape. The two degrees of freedom models have several high frequencies that are difficult to count using the manual method employed in this study. It would be interesting to develop some method to digitally process the video images so that many frequencies could be determined directly from the videotape.

The tensile stress in the fibers due to the aerodynamic force acting along the axis of the fiber appears to be about two orders of magnitude greater than the stresses due to the bending of the fiber when the fibers are mounted in the wind tunnel. This suggests that the bending stresses are negligible when the fiber is parallel to the air stream.

## Chapter 8

### CONCLUSIONS AND FUTURE POSSIBILITIES

#### 8.1 Conclusions

The first objective of this thesis was to develop a simple method to model the motion of a single fiber in a turbulent velocity field. The kinematic model provided a realistic model of the motion of polypropylene fibers with diameters of 12  $\mu\text{m}$  and 30  $\mu\text{m}$ . The model provided realistic displacements and frequencies for these fibers.

The numerical simulations indicated that turbulence parallel to the axis of the fiber had a very small effect upon the motion of the fiber. As a result, it is possible to use mean axial velocity in future fiber models. This simplification will eliminate the need for turbulence measurements in the axial direction. Another benefit of the kinematic model is that both the mean air velocities and turbulence acting upon the fiber can vary along the length of the fiber. This ability to incorporate varying external forces will allow a fiber to be modeled in a general velocity field.

The kinematic model provides several different physical parameters of interest. These parameters include the displacement at the tip of the fiber, the fluctuation frequency for the fiber, and the stress at the root of the fiber. Of these three parameters, the displacement and frequency are the most important. The importance of the stress

distribution within the fiber depends upon whether the fiber is above or below the glass transition temperature and is beyond the scope of this study.

The final benefit of the kinematic model is the ease of programming. The numerical simulation can be easily implemented using common spreadsheet software. Unfortunately, models are effectively limited to two degree of freedom models using commonly available computers. Writing a program designed solely to perform the numerical simulation would enable higher order models to be studied.

The biggest drawback of the kinematic model is the sensitivity of the model to the size of the time step. A time step on the order of  $10^{-5}$  seconds is required for a two degree of freedom  $12\ \mu\text{m}$  fiber model. This small time step is the result of the small mass of the fibers and the short lengths being modeled. This fact indicates that if longer fibers were to be modeled, the required time step would increase and simplify the modeling procedure.

Overall, the kinematic fiber model provides a simple yet useful tool to model the motion of a single fiber in a turbulent air stream. The study in this thesis was limited to the using models with two degrees of freedom or less. The use of models with four or eight degrees of freedom should result in more accurate results.

## 8.2 Future Possibilities for Research

While the kinematic model provides a simple way to model a single fiber, there are many refinements that can be made to improve the accuracy of the results. Perhaps the largest improvement could be achieved by changing the assumption that the hinge

connections provide no resistance to bending. Adding a bending resistance to hinge connections provides an easy way to add the effect of section and material properties to the fiber model.

The second improvement would be to write computer code specifically to perform the numerical simulation. The simulations in this thesis were performed using commercially available spreadsheet software, and as a result, were limited to small models. The use of higher order models (four degree of freedoms and more) would result in more accurate simulations.

One of the limiting factors in this study was the lack of a drag correlation for discontinuous fibers. The drag correlation used in this study was developed using continuous fibers. The development of a correlation applicable to discontinuous fibers would eliminate some of the uncertainties present in the data.

There are many possibilities open for future research on modeling single fibers in a wind tunnel. There are several different methods that can be used to model a fiber. If the effect of the modulus of elasticity and section properties is negligible, then the fiber can be modeled as a stochastic string PDE. If the effect of these properties is not negligible, then the fiber can be modeled as a stochastic beam PDE.

Another approach that could be taken to model the fiber is to treat it as a spring-mass-damper system. If this approach is chosen, then the kinematic model can be used to determine an effective damping force to use in the model. Another approach that can be

taken is to model the fiber as a compound pendulum. In each of these methods, the Dunhamel equation could be used to solve the position of the fiber.

The present research utilized fibers of a single material. It would be interesting to see how fibers with different material properties behave under the same flow conditions. Comparing the frequency and displacement of a fiber made of a very stiff material with the motion of a polypropylene fiber would help indicate the effect of the material and section properties upon the motion.

Another possible area of research would be to repeat the high-speed videotape with some means of digitally analyzing the videotape to obtain frequencies and displacements. This would allow more accurate displacement and frequency information for the fibers to be obtained. The use of the high-speed video system is limited without the use of digital processing.

Future research on the motion of single fibers is endless.

## REFERENCES CITED

- Bland, D.R. 1960. Vibrating Strings: An Introduction to the wave equation. London: Routledge and Kegan Paul.
- Caddell, R.M. 1980. Deformation and Fracture of Solids. New Jersey: Prentice-Hall.
- Cai, Y. 1994. Modeling fiber formation by the spinning process. Ph.D. Dissertation. Golden, CO: Colorado School of Mines.
- Cai Y., Munoz, D.R., DePoorter, G., Martin, P.. 1994. Modeling fiber formation by the spinning process. FED-Vol. 206/AMD-Vol. 191, Developments in Non-Newtonian Flows. ASME.
- Fraser, R.P., Dombrowski, N., Routley, J.H. 1963. The filming of liquids by spinning cups. Chemical Engineering Science (18): 323-337.
- Hinze, J.O. 1974. Turbulence, 2<sup>nd</sup> Edition. New York:McGraw-Hill.
- Hristov, H.A., Hearle, J.W. S., Schultz, J.M., Kennedy, A.D. 1995. Rapid mechanical deformations of poly(ethylene terephthalate) fibers at temperatures above the glass transition. Journal of Polymer Science: Part B: Polymer Physics (33):125-133.
- MathSoft, 1998. Mathcad 8: User's Guide. Cambridge, MA: MathSoft.
- Nayfeh, A.H., Chin, C., Nayfeh, S.A. 1995. Nonlinear normal modes of a cantilever beam. Journal of Vibration and Acoustics (117): 477-481.
- Rao, S. S. 1995. Mechanical Vibrations. Reading, MA: Addison-Wesley.
- Schlichting. 1979. Boundary Layer Theory, New York: McGraw-Hill.
- Shigley, J.E., 1967. Simulation of Mechanical Systems. New York: McGraw-Hill.
- Steidel, R. F. 1971. An Introduction to Mechanical Vibrations. New York: John Wiley and Sons.
- Tabaddor, M., Nayfeh, A.H., 1997. An experimental investigation of multimode response in a cantilever beam, Journal of Vibration and Acoustics (119): 532-538.

Tresso, R.J. 1998. Three-dimensional statistical and cross moment methods for identifying and characterizing isotropic, homogeneous turbulent flow regions downstream of a square mesh. Thesis (M. Sc.) Golden, CO: Colorado School of Mines.

White, F.M. 1974. Viscous Fluid Flow. New York: McGraw-Hill.

Wolochuk, M.C., Plesniak, M.W., Braun, J.E. The Effects of Turbulence and Unsteadiness on Vortex Shedding from Sharp-Edged Bluff Bodies, Transactions of the ASME Journal of Fluids Engineering (118), pp.18-25.

Wylie, C.R., Barret, L.C. 1982. Advanced Engineering Mathematics. 5<sup>th</sup> Edition. New York: McGraw-Hill.

Ziabicki, A. 1976. Fundamentals of Fibre Formation: The Science of Fibre Spinning and Drawing. New York: John Wiley and Sons.

Ziabicki, A., Kawai, H. 1985. High Speed Fibre spinning: Science and Engineering Aspects. Malabar, FL: Krieger Publishing Company.

APPENDIX A  
DISPLACEMENT PLOTS FOR DAMPING  
CALCULATIONS

This Appendix contains the complete set of fiber positions versus time plots for the numerical simulations discussed in section 7.2. These plots provide the basis for calculating the damping provided by the axial velocity.

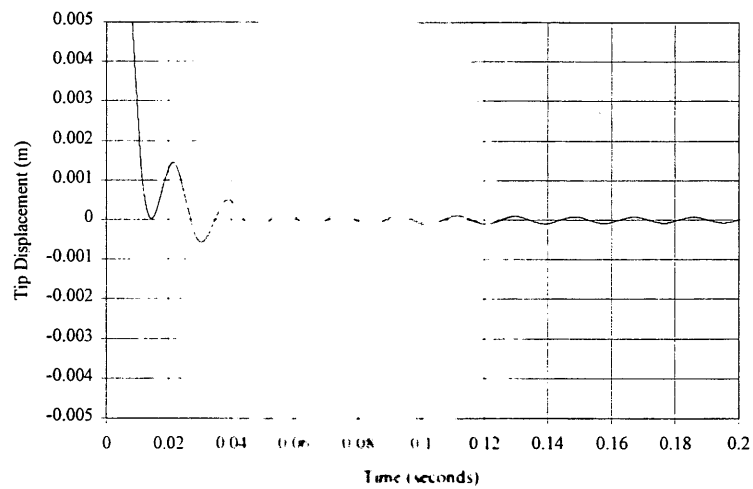


Figure A-1

Tip displacement plot for 12μm fiber (Constant axial velocity, 1000 RPM).

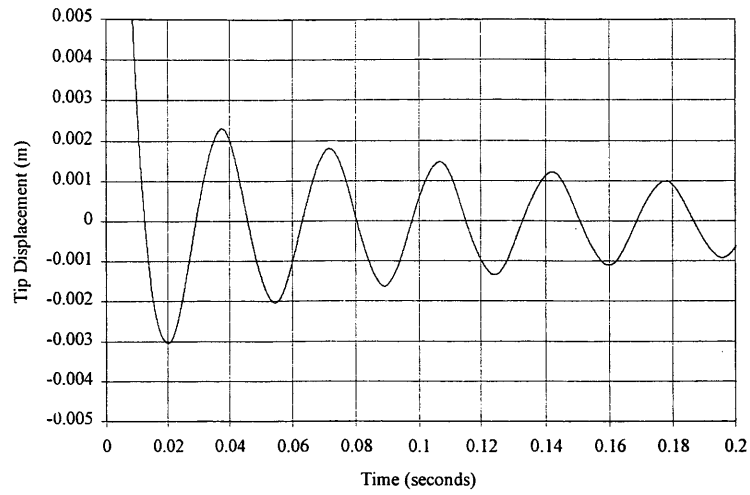


Figure A-2

Tip displacement plot for 30 $\mu$ m fiber (Constant axial velocity, 1000 RPM).

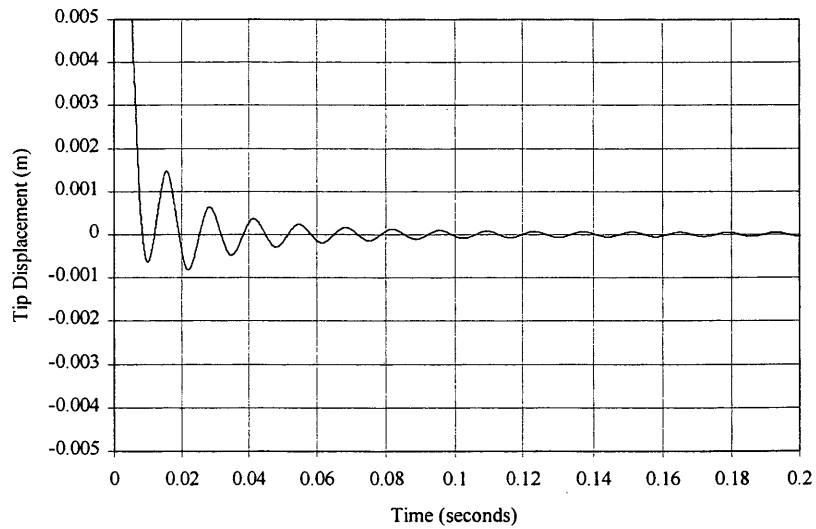


Figure A-3

Tip displacement plot for 12 $\mu$ m fiber (Constant axial velocity, 1500 RPM).

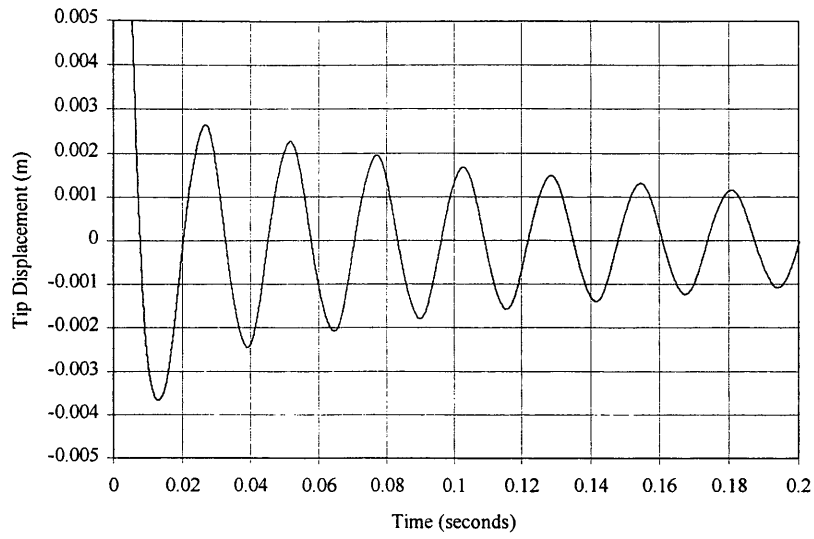


Figure A-4

Tip displacement plot for 30 μm fiber (Constant axial velocity, 1500 RPM).

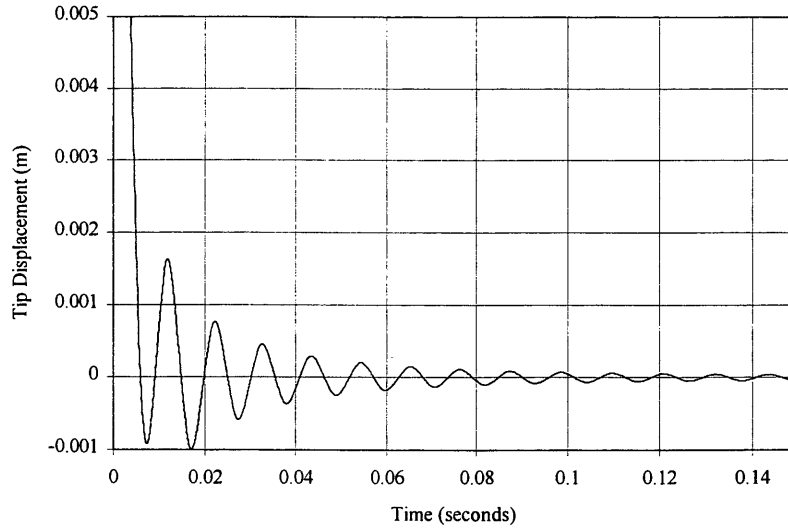


Figure A-5

Tip displacement plot for 12 μm fiber (Constant axial velocity, 2000 RPM).

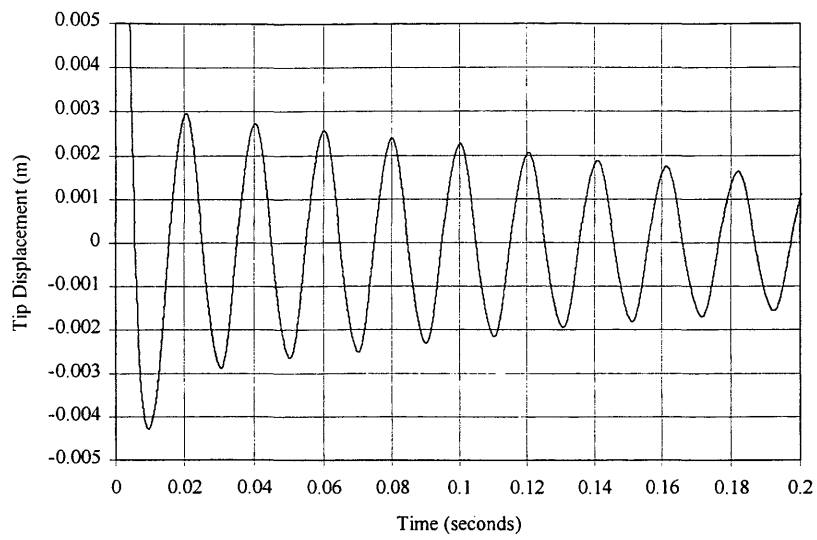


Figure A-6

Tip displacement plot for 30 $\mu$ m fiber (Constant axial velocity, 2000 RPM).

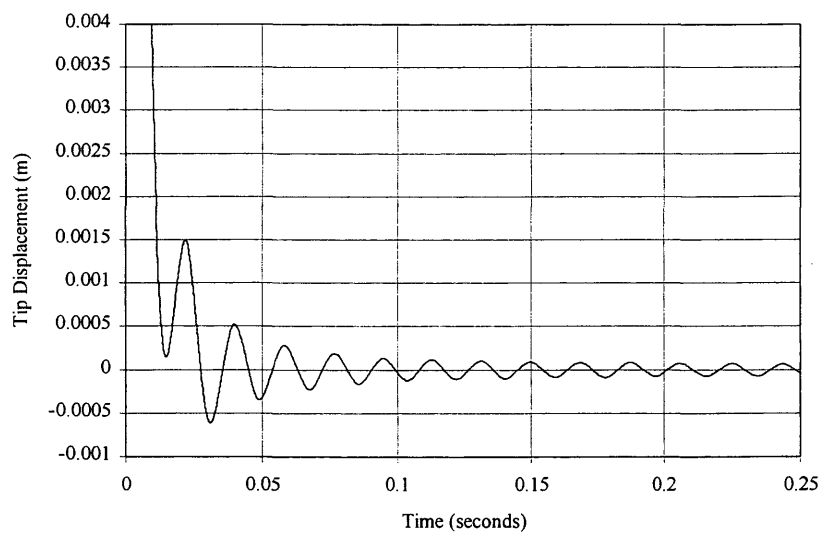


Figure A-7

Tip displacement plot for 12 $\mu$ m fiber (with axial turbulence, 1000 RPM).

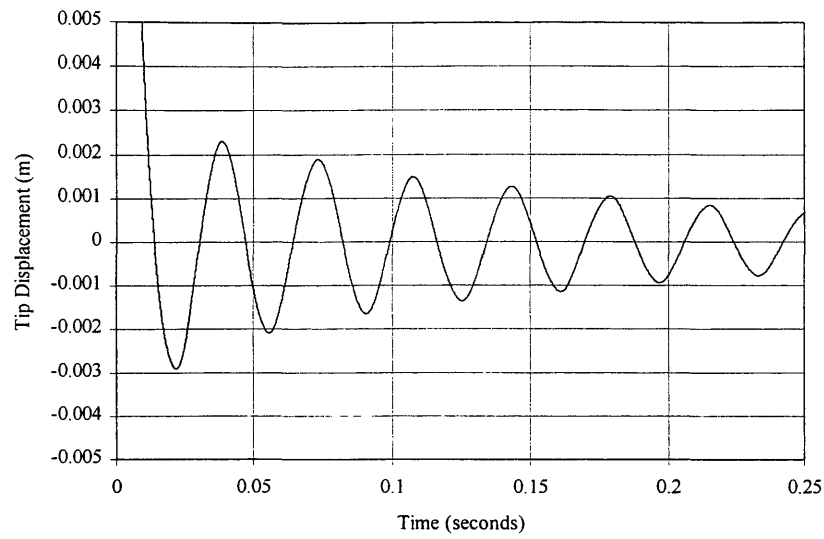


Figure A-8

Tip displacement plot for 30 $\mu$ m fiber (with axial turbulence, 1000 RPM).

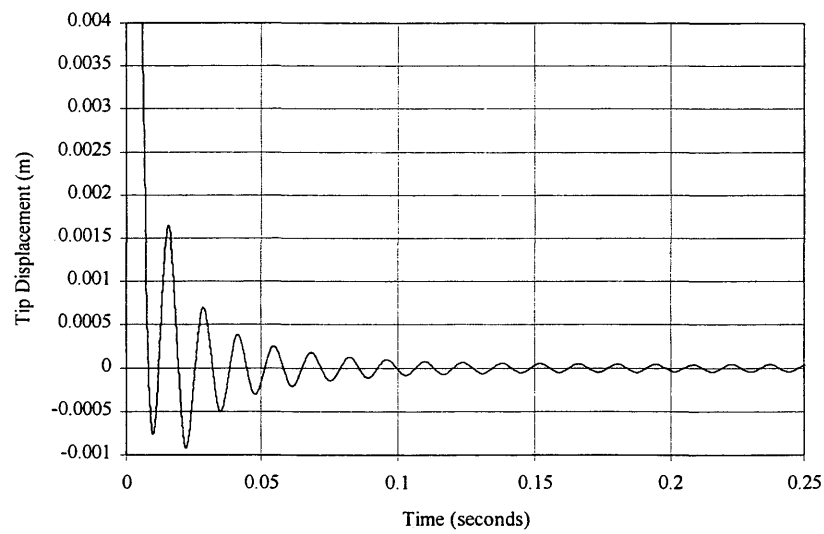


Figure A-9

Tip displacement plot for 12 $\mu$ m fiber (with axial turbulence, 1500 RPM).

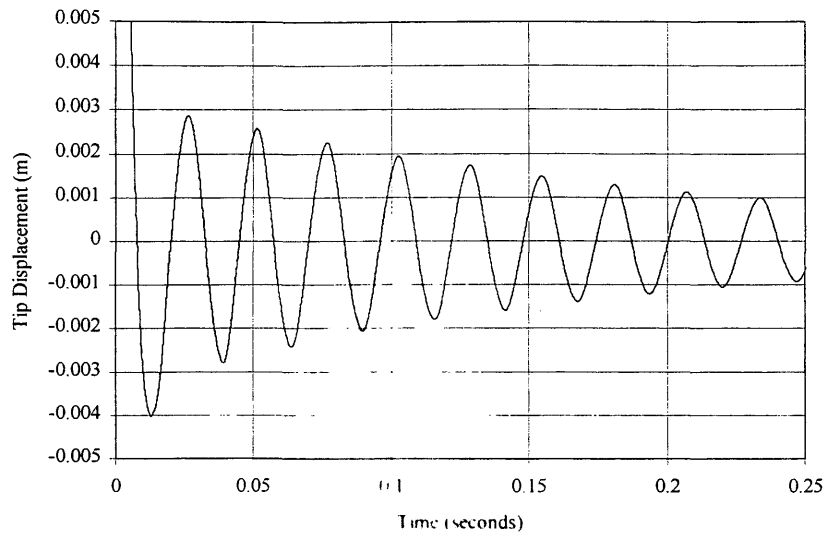


Figure A-10

Tip displacement plot for 30 $\mu$ m fiber (with axial turbulence, 1500 RPM).

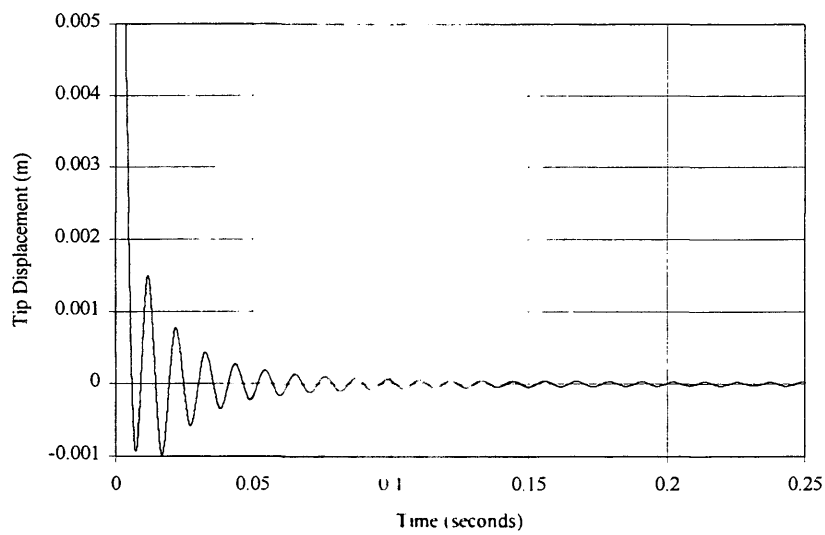


Figure A-11

Tip displacement plot for 12 $\mu$ m fiber (with axial turbulence, 2000 RPM).

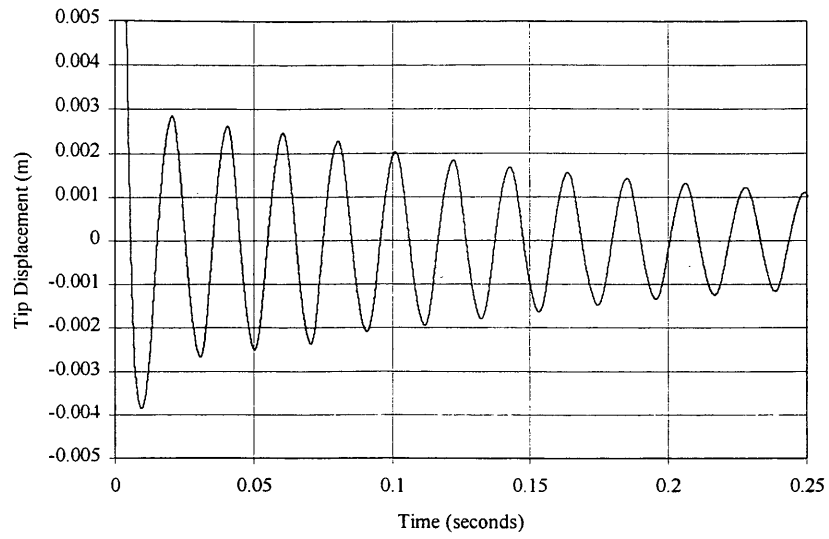


Figure A-12

Tip displacement plot for 30μm fiber (with axial turbulence, 2000 RPM).

APPENDIX B  
NUMERICAL SIMULATION DISPLACEMENT  
PLOTS

This Appendix contains displacement versus time plots resulting from the numerical simulations. The maximum positive displacement, the maximum negative displacement and the mean position for each fiber and each fan speed combination are summarized in Chapter 7.

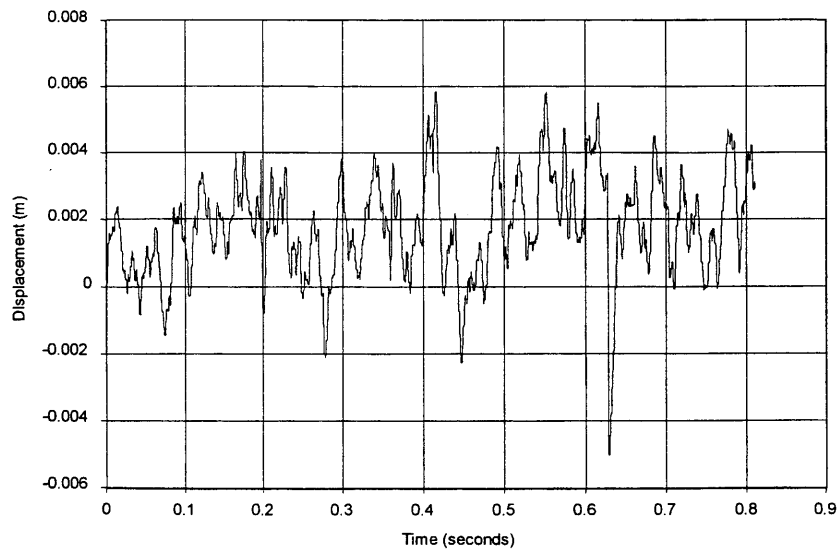


Figure B-1

Tip displacement for 12 $\mu$ m, single degree of freedom model (1000 RPM).

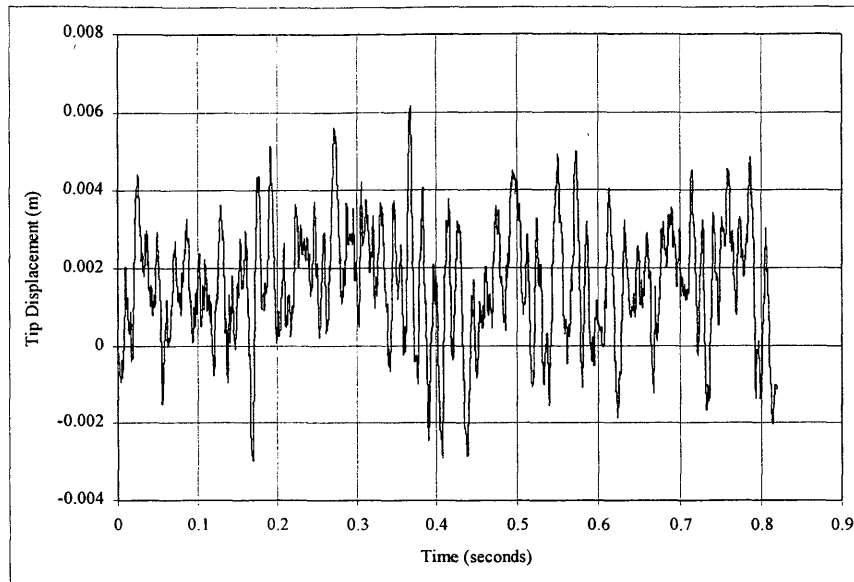


Figure B-2

Tip displacement for  $12\mu\text{m}$ , two degrees of freedom model (1000 RPM).

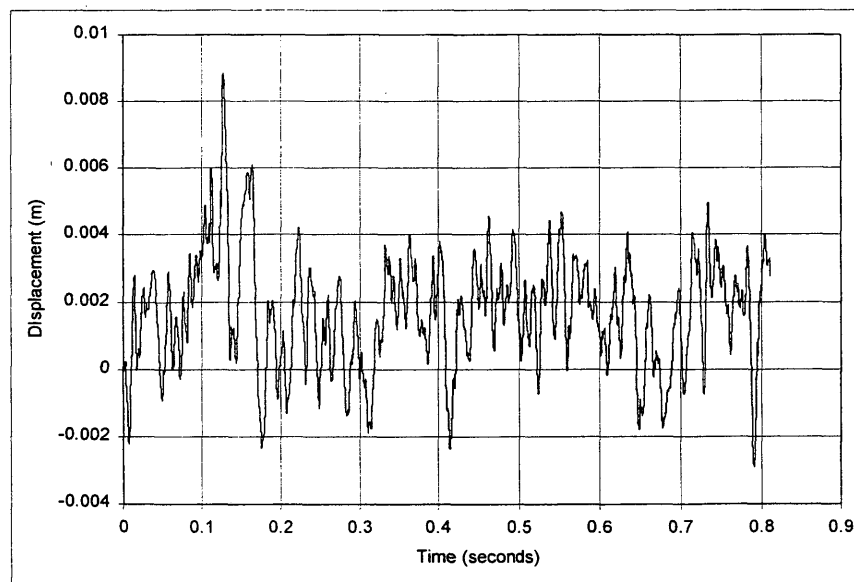


Figure B-3

Tip displacement for  $12\mu\text{m}$ , single degree of freedom model (1500 RPM).

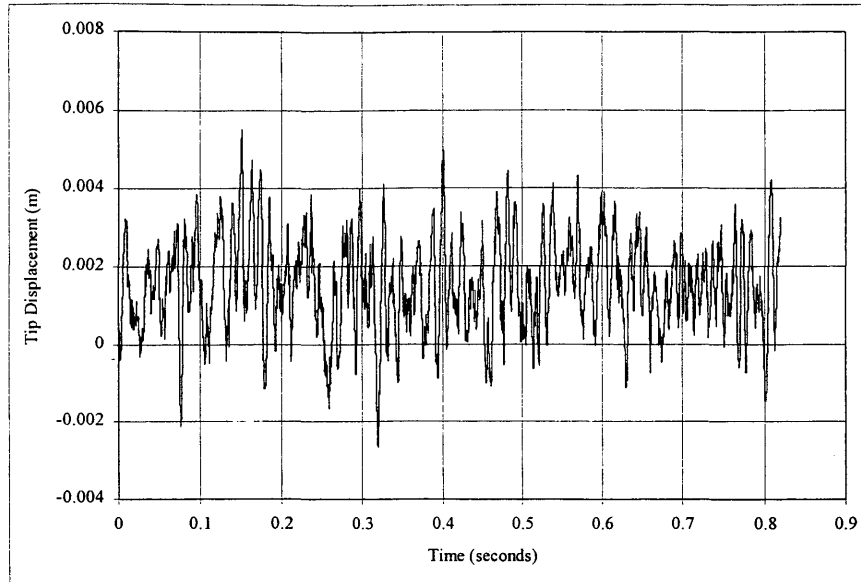


Figure B-4

Tip displacement for  $12\mu\text{m}$ , two degrees of freedom model (1500 RPM).

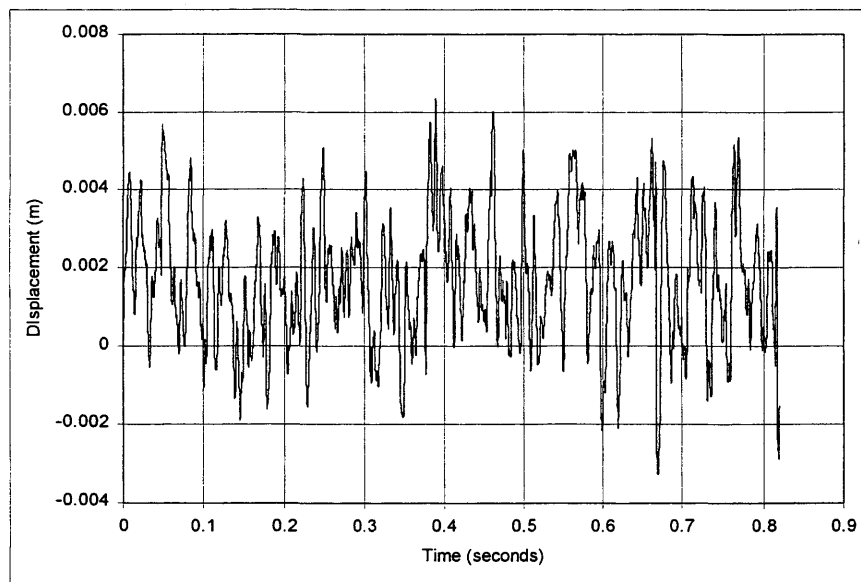


Figure B-5

Tip displacement for  $12\mu\text{m}$ , single degree of freedom model (2000 RPM).

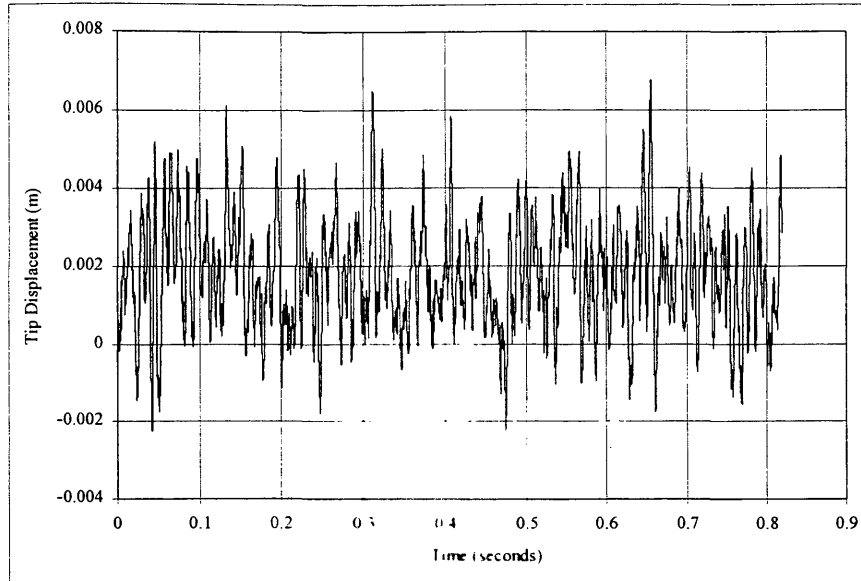


Figure B-6

Tip displacement for  $12\mu\text{m}$ , two degrees of freedom model (2000 RPM).

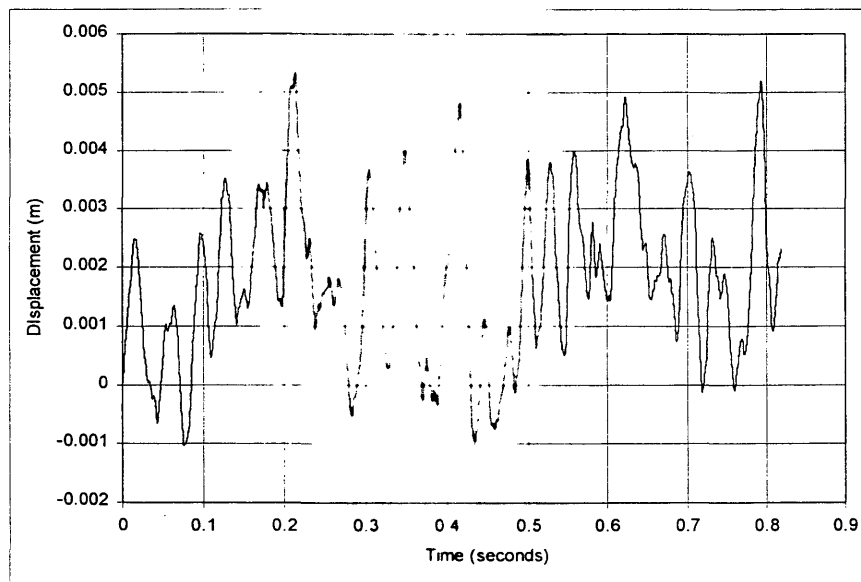


Figure B-7

Tip displacement for  $30\mu\text{m}$ , single degree of freedom model (1000 RPM).

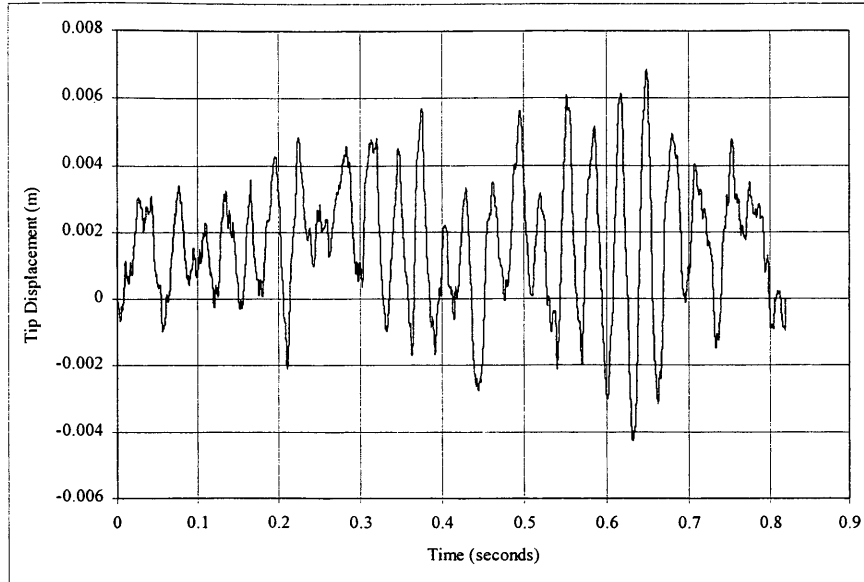


Figure B-8

Tip displacement for  $30\mu\text{m}$ , two degrees of freedom model (1000 RPM).

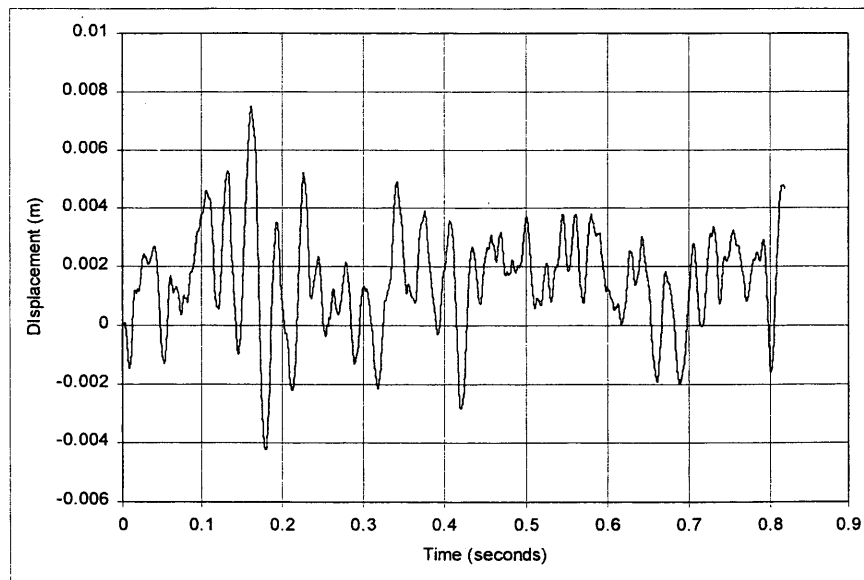


Figure B-9

Tip displacement for  $30\mu\text{m}$ , single degree of freedom model (1500 RPM).

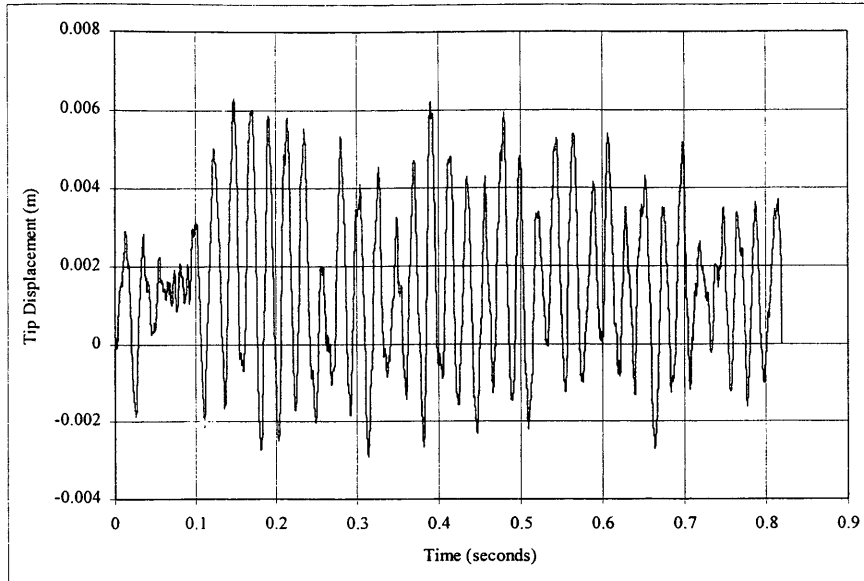


Figure B-10

Tip displacement for  $30\mu\text{m}$ , two degrees of freedom model (1500 RPM).

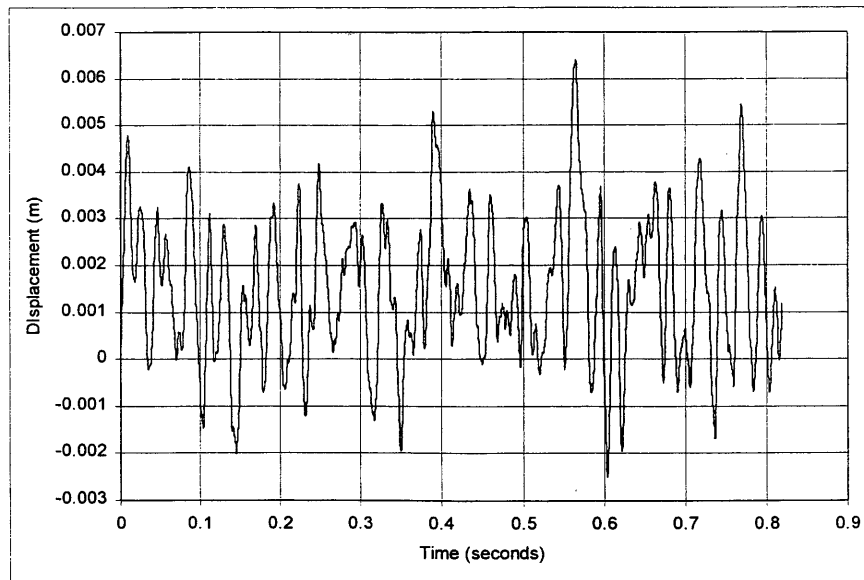


Figure B-11

Tip displacement for  $30\mu\text{m}$ , single degree of freedom model (2000 RPM).

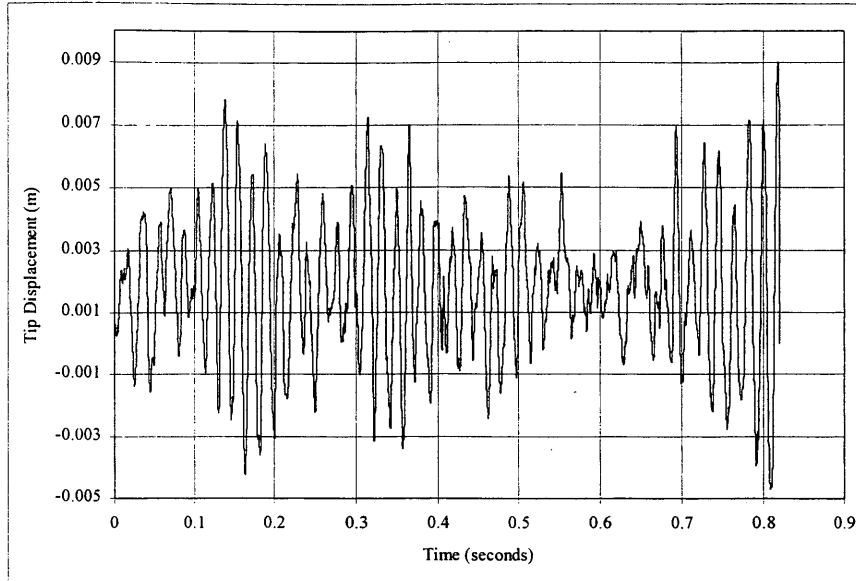


Figure B-12

Tip displacement for  $30\mu\text{m}$ , two degrees of freedom model (2000 RPM).

APPENDIX C  
NUMERICAL SIMULATION FREQUENCY  
SPECTRUM PLOTS

This Appendix contains frequency spectrum plots resulting from the numerical simulations.

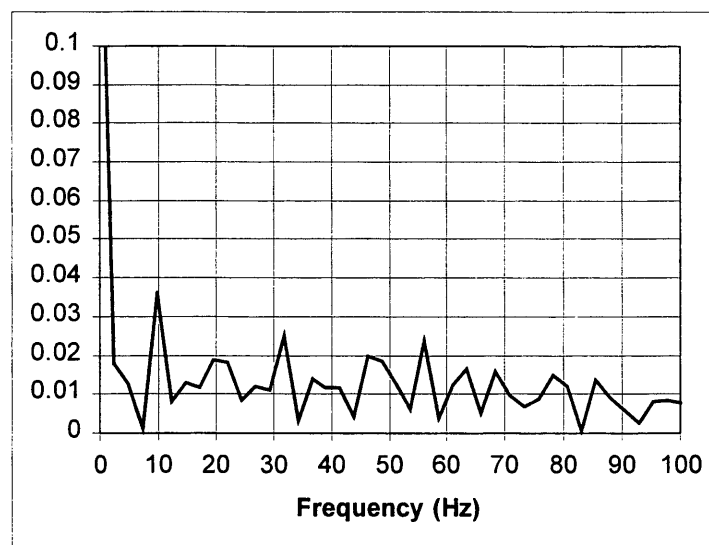


Figure C-1

Frequency Spectrum for 12 $\mu$ m, single degree of freedom model (1000 RPM).

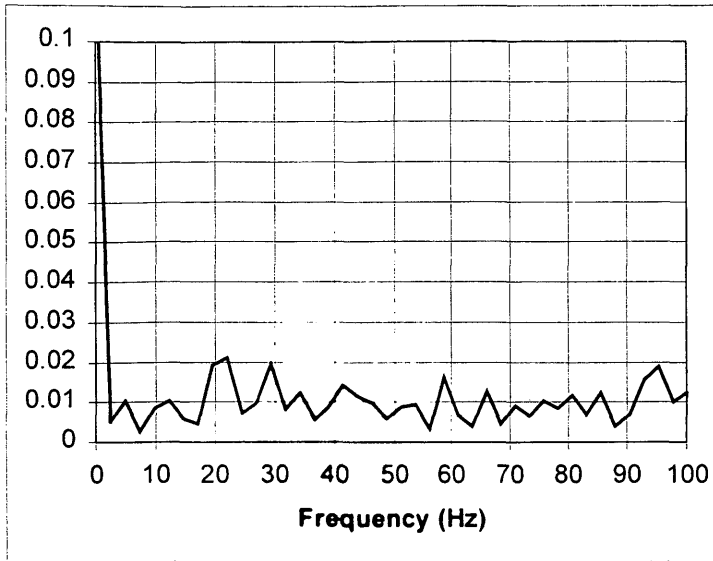


Figure C-2

Frequency Spectrum for 12 $\mu$ m, two degrees of freedom model (1000 RPM).

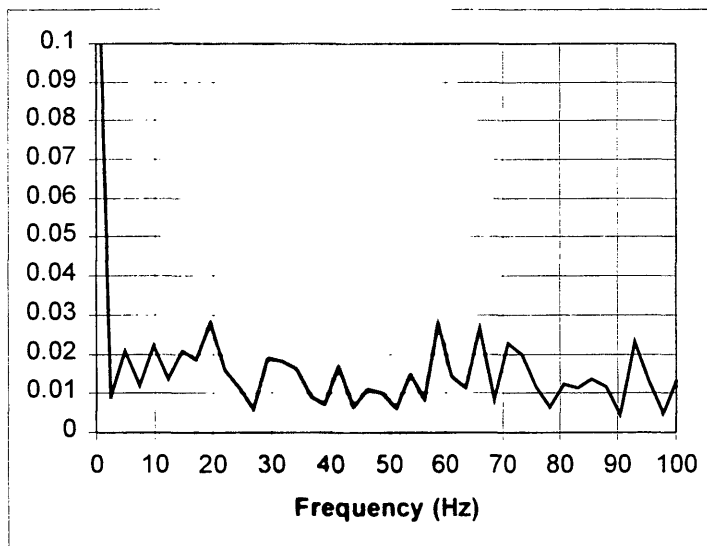


Figure C-3

Frequency Spectrum for 12 $\mu$ m, single degree of freedom model (1500 RPM).

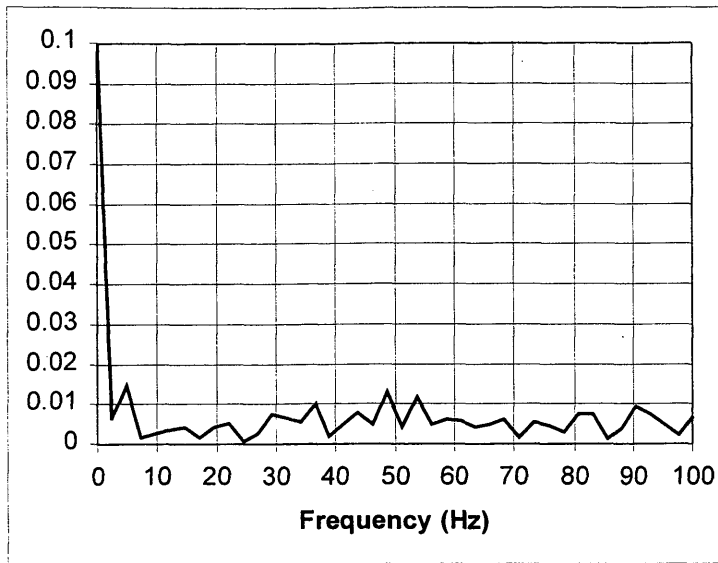


Figure C-4

Frequency Spectrum for 12 $\mu$ m, two degrees of freedom model (1500 RPM).

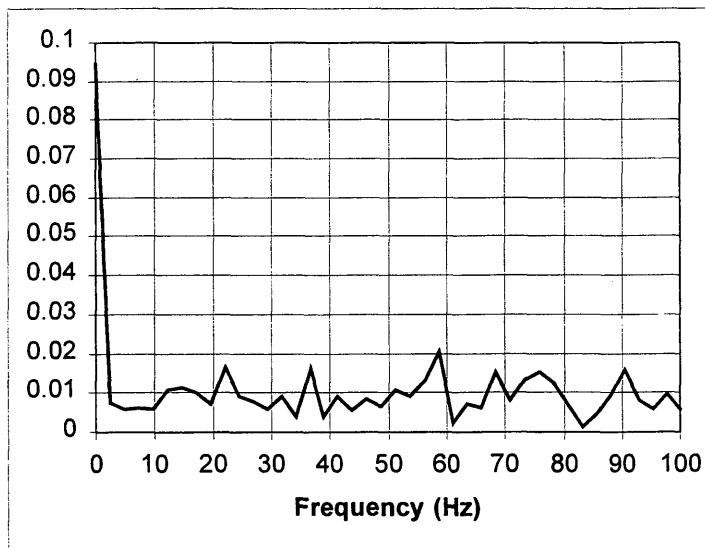


Figure C-5

Frequency Spectrum for 12 $\mu$ m, single degree of freedom model (2000 RPM).

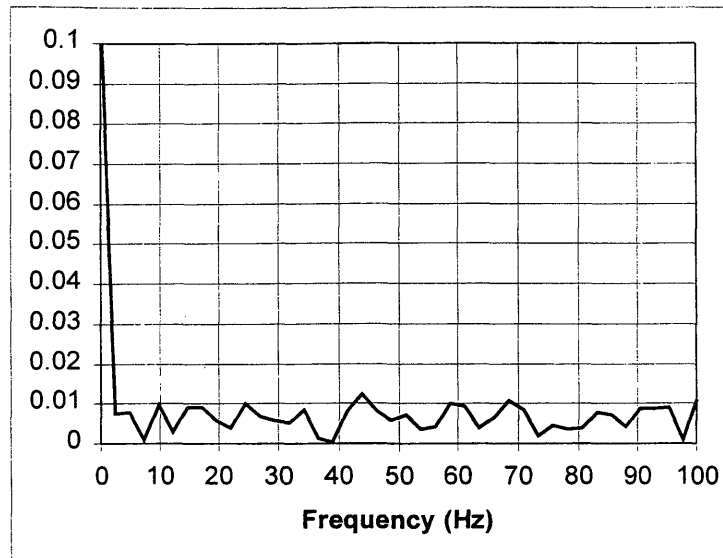


Figure C-6

Frequency Spectrum for 12 $\mu\text{m}$ , two degrees of freedom model (2000 RPM).

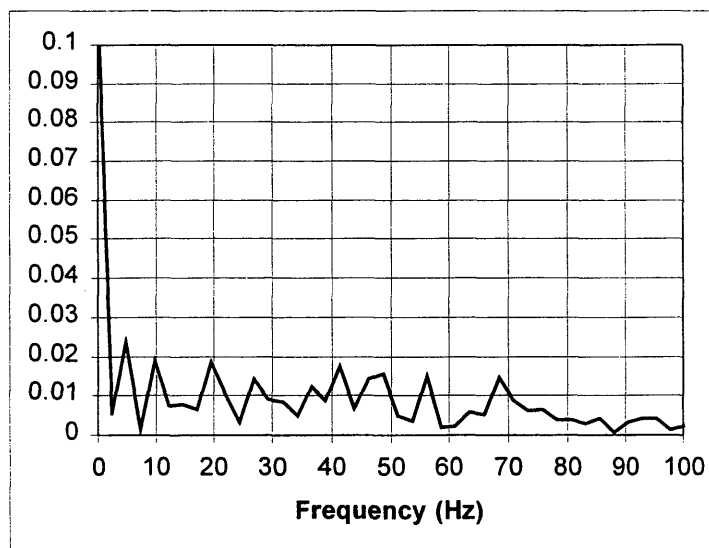


Figure C-7

Frequency Spectrum for 30 $\mu\text{m}$ , single degree of freedom model (1000 RPM).

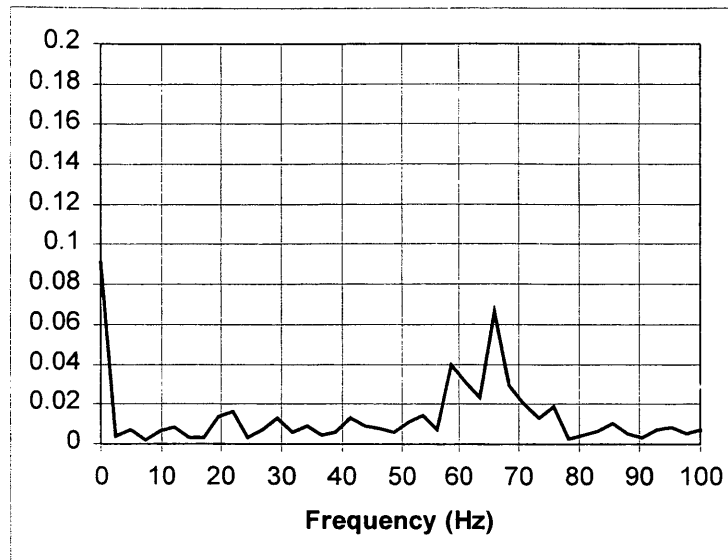


Figure C-8

Frequency Spectrum for 30μm, two degrees of freedom model (1000 RPM).

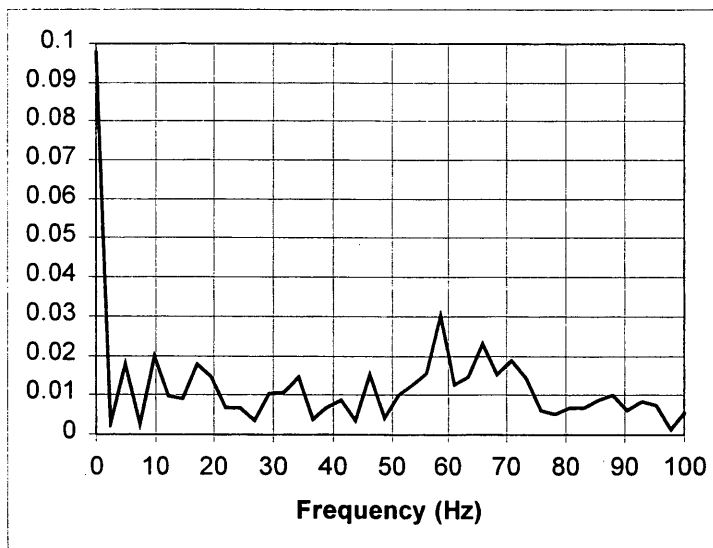


Figure C-9

Frequency Spectrum for 30μm, single degree of freedom model (1500 RPM).

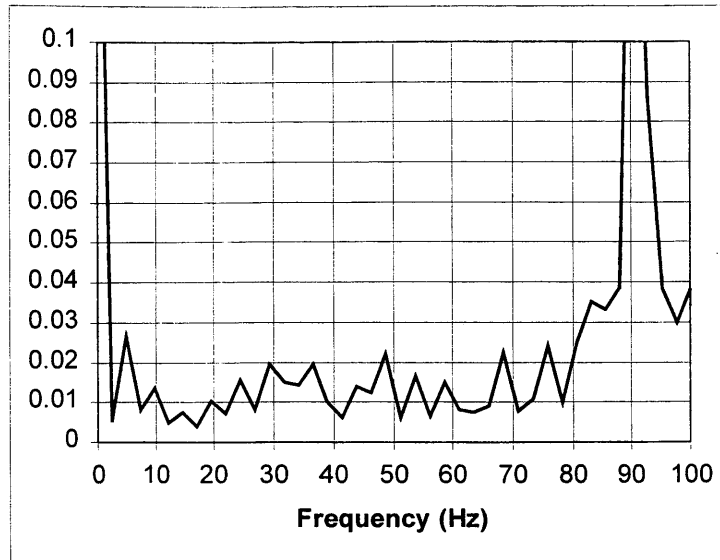


Figure C-10

Frequency Spectrum for 30 $\mu$ m, two degrees of freedom model (1500 RPM).

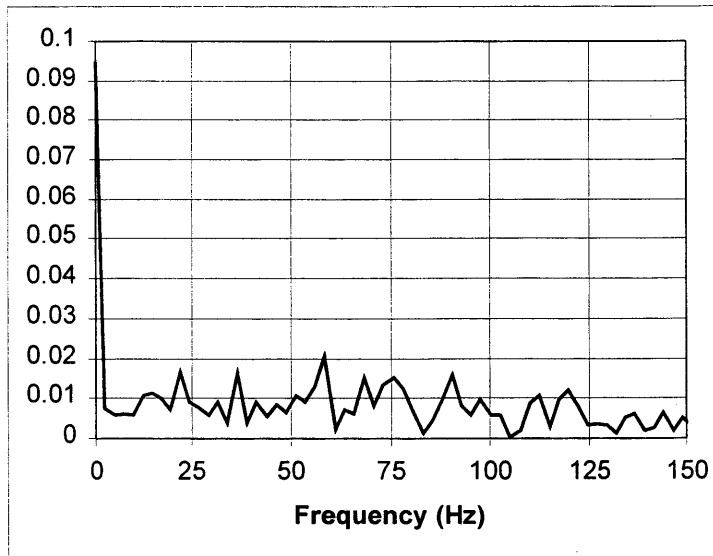


Figure C-11

Frequency Spectrum for 30 $\mu$ m, single degree of freedom model (2000 RPM).

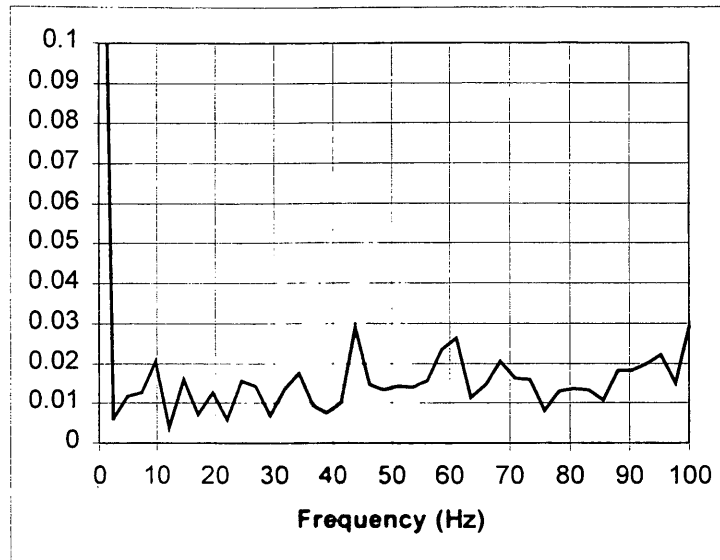


Figure C-12

Frequency Spectrum for 30 $\mu$ m, two degrees of freedom model (2000 RPM).

## APPENDIX D

## NUMERICAL SIMULATION TENSILE FORCE PLOTS

This Appendix contains tensile force versus time plots resulting from the numerical simulations.

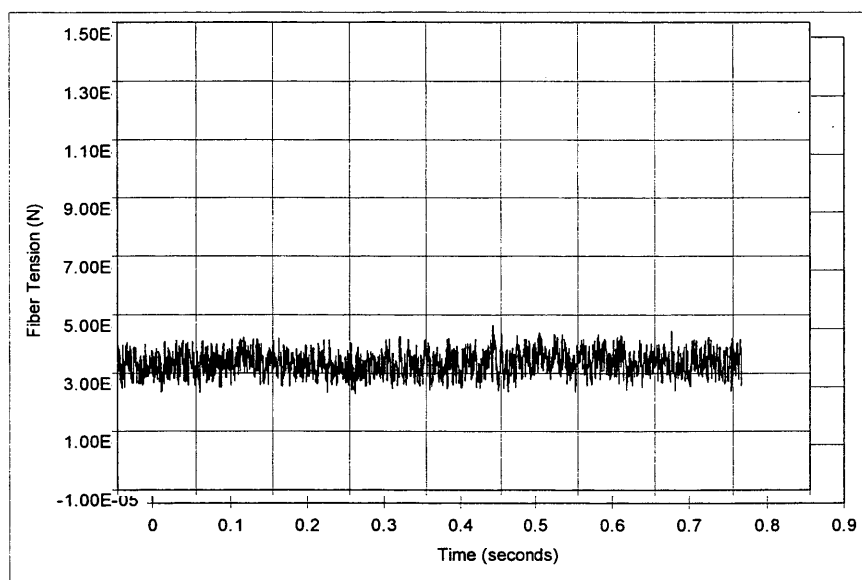


Figure D-1

Fiber tension for 12 $\mu$ m, single degree of freedom model (1000 RPM).

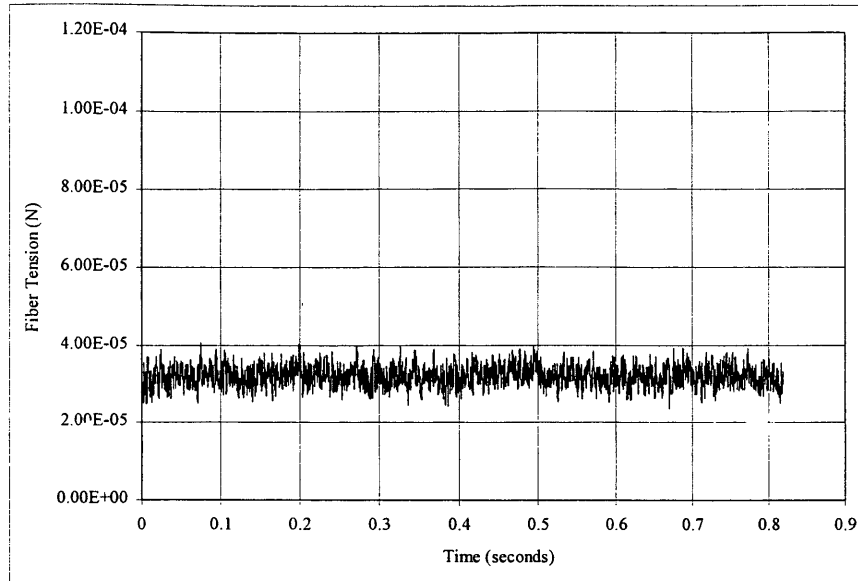


Figure D-2

Fiber tension for 12 $\mu$ m, two degrees of freedom model (1000 RPM).

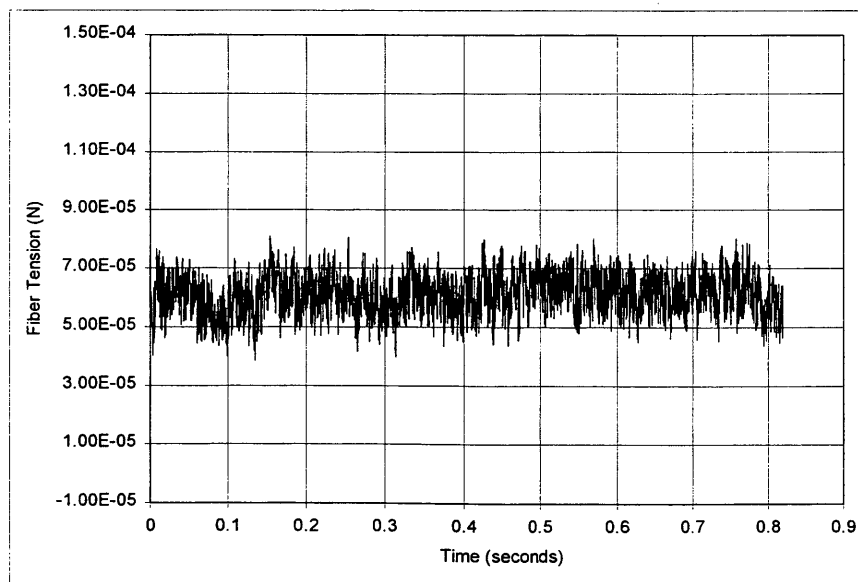


Figure D-3

Fiber tension for 12 $\mu$ m, single degree of freedom model (1500 RPM).

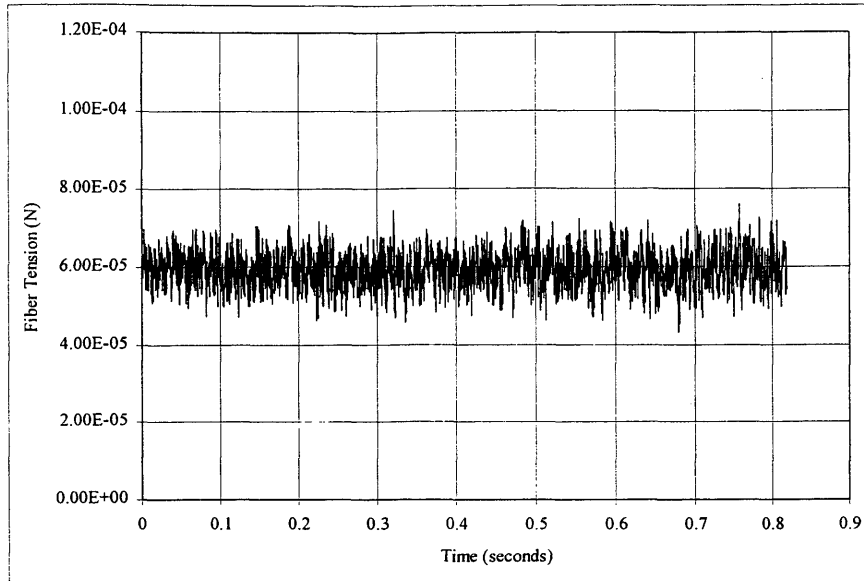


Figure D-4

Fiber tension for 12μm, two degrees of freedom model (1500 RPM).

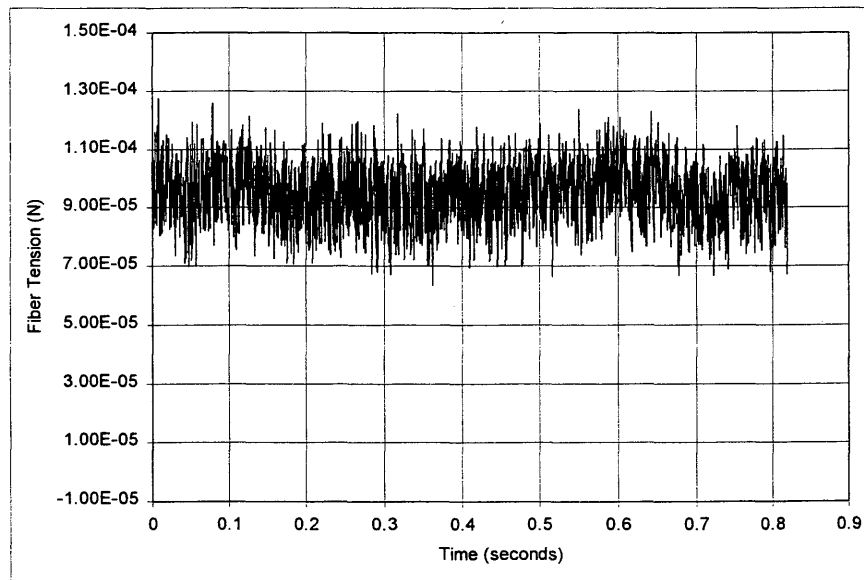


Figure D-5

Fiber tension for 12μm, single degree of freedom model (2000 RPM).

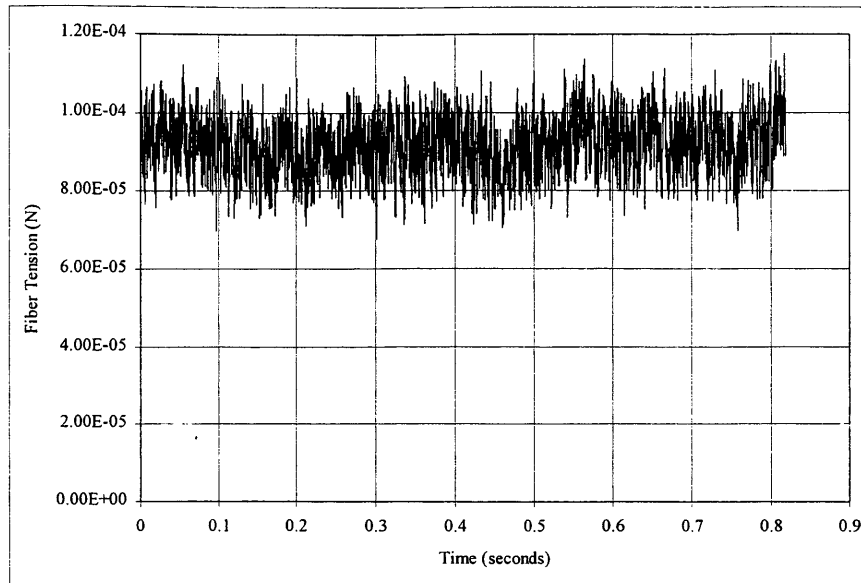


Figure D-6

Fiber tension for 12 $\mu$ m, two degrees of freedom model (2000 RPM).

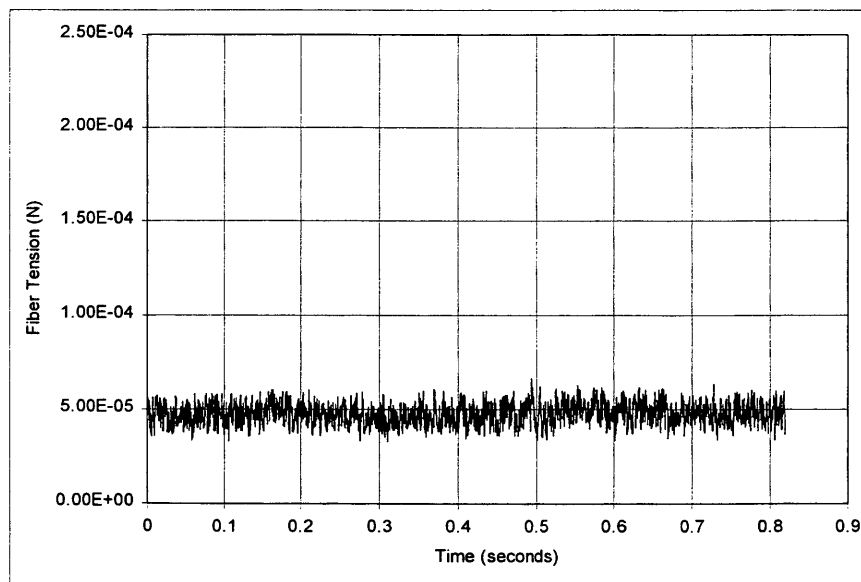


Figure D-7

Fiber tension for 30 $\mu$ m, single degree of freedom model (1000 RPM).

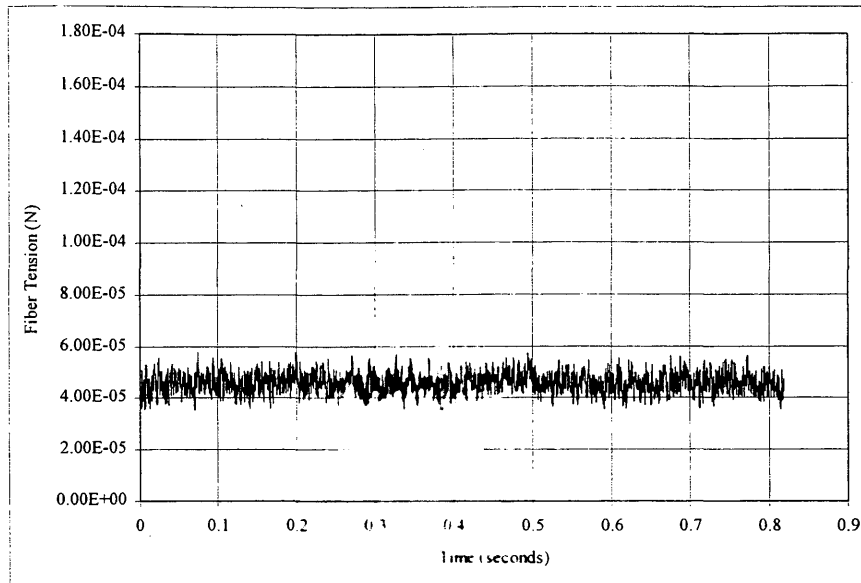


Figure D-8

Fiber tension for 30µm, two degrees of freedom model (1000 RPM).

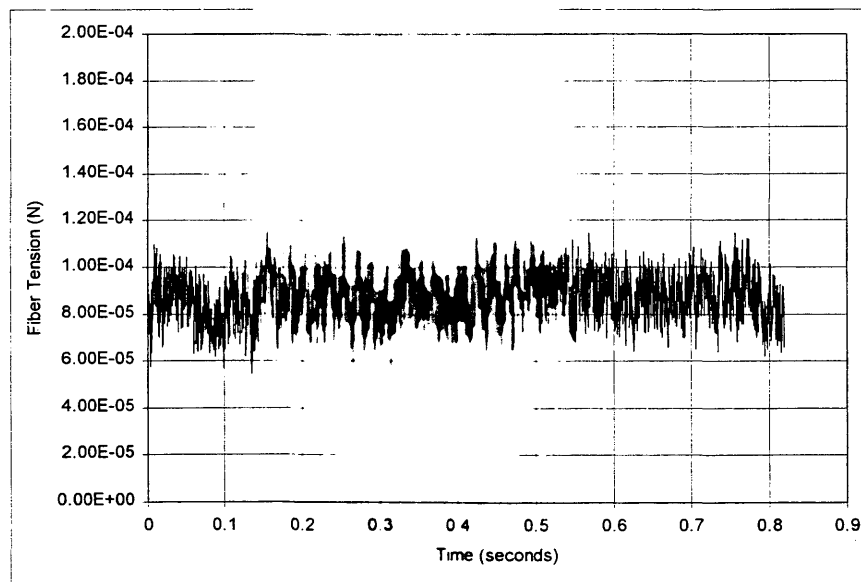


Figure D-9

Fiber tension for 30µm, single degree of freedom model (1500 RPM).

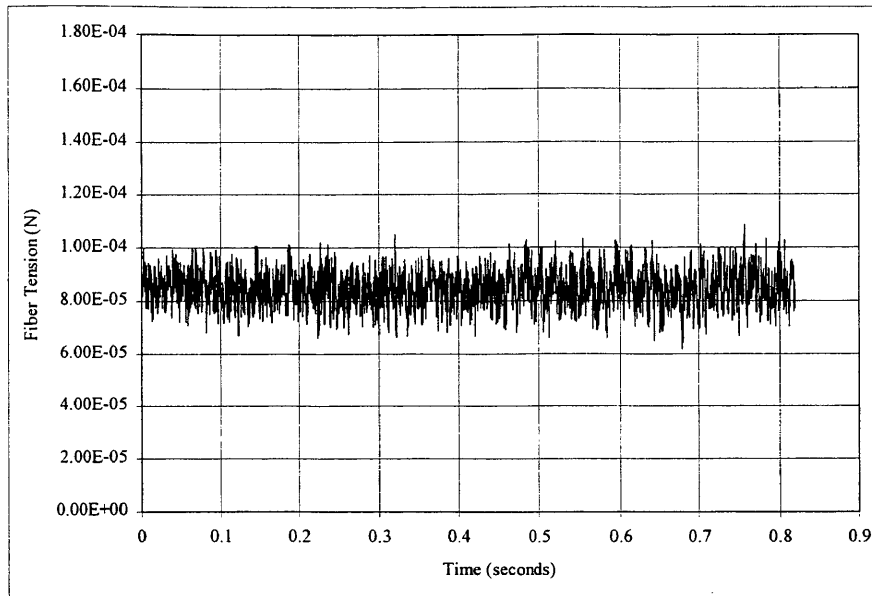


Figure D-10

Fiber tension for 30 $\mu$ m, two degrees of freedom model (1500 RPM).

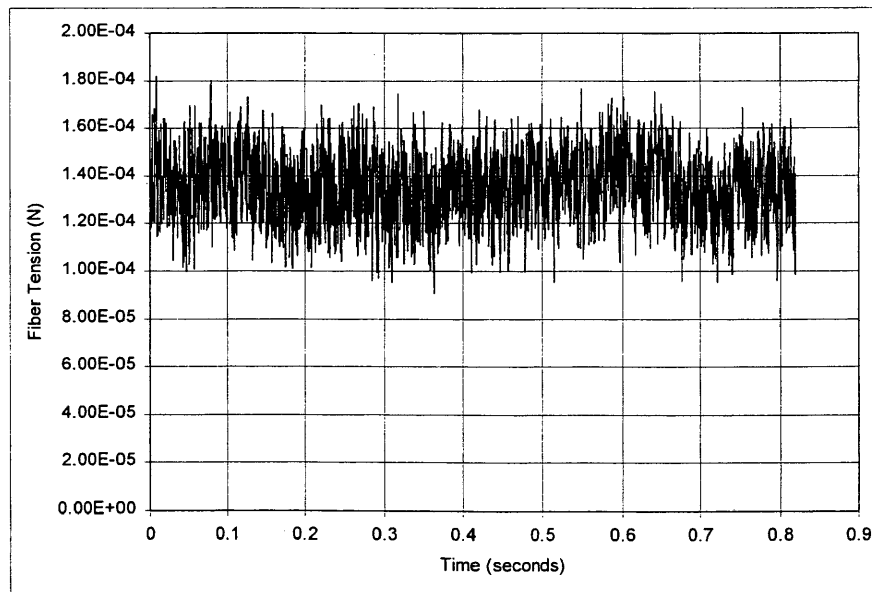


Figure D-11

Fiber tension for 30 $\mu$ m, single degree of freedom model (2000 RPM).

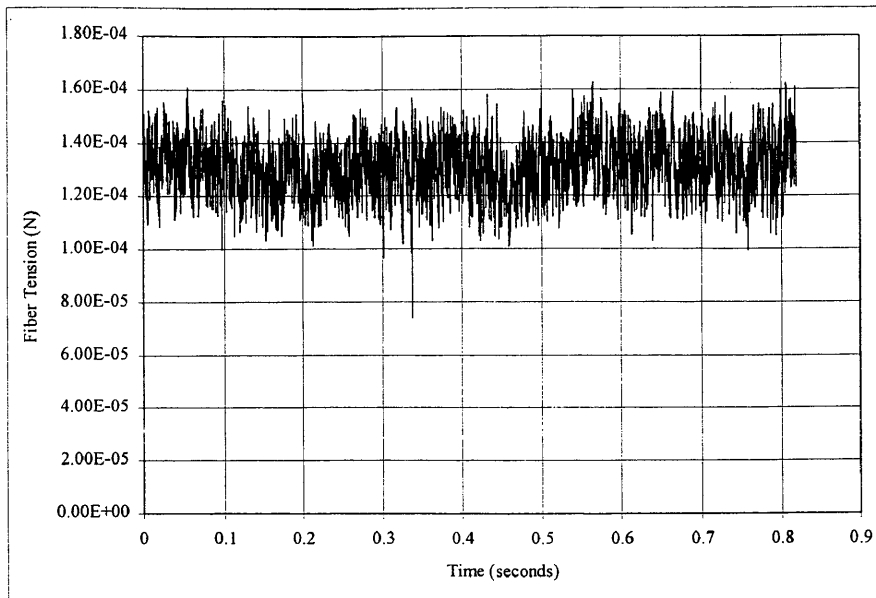


Figure D-12

Fiber tension for 30 $\mu$ m, two degrees of freedom model (2000 RPM).